



NICOLAUS COPERNICUS  
UNIVERSITY  
IN TORUŃ

---

***In-vivo* assessment of age-related changes in the  
human crystalline lens using optical imaging  
systems**

---

*Author:*

Ashish Gupta

*Supervisor:*

Dr hab. Ireneusz Grulkowski, prof. UMK

*Co-supervisor:*

Dr Daniel Ruminski

*A dissertation submitted in fulfilment of the requirements for the degree of  
Doctor of Philosophy in the*

Department of Biophysics, Institute of Physics  
Faculty of Physics, Astronomy, and Informatics  
Nicolaus Copernicus University in Toruń

**Toruń, June 2023**



*“The study of nature must necessarily involve the study of the human sense as well. In order to be accurate in our observations of light and colour in the landscape, we must, first of all, be familiar with the instrument we use continually-namely, the human eye.”*

***Marcel Minnaert***



# Abstract

The human crystalline lens is a biconvex adjustable refractive element of the eye and consists of concentric layers of fibre cells that form the lens nucleus and cortex. The lens is subject to several ageing processes that alter structural, optical and biomechanical lens properties, leading to a gradual deterioration in vision. The ever-growing fibre cells cause continuous remodelling of lens morphology by increasing the lens size and weight. Human crystalline lens transparency is achieved by specific structural lens organisation, and age-related molecular changes in the lens lead to increased intraocular light scattering.

The main goal of the study was to demonstrate and quantify characteristic age-related alterations in the crystalline lens by the measurement of forward- and back-scattering in healthy subjects and to associate those changes with vision degradation. Specifically, the thesis concentrated on: (1) lens shape remodelling with age, (2) gradual loss of lens transparency and reduction of visual performance, and (3) optical inhomogeneities within the lens associated with the micro-structural lens organization. Two modern imaging instruments, anterior segment swept-source optical coherence tomography (OCT) and double-pass imaging of retinal point spread function, were used to assess both the lens morphology and intraocular scattering. Firstly, I demonstrated that crystalline lens morphology (thickness and radii of surface curvature) changes with age. I also evaluated that the optical quality of the lens degrades with age as the back-scattered optical signal increases. Secondly, I performed a detailed analysis of the age-related changes in the optical signal discontinuity zones of the lens (nucleus and cortical C1 $\alpha$ , C1 $\beta$ , C2, C3, and C4 zones) based on high-definition OCT images and Oxford system nomenclature. The bright zone, C3, was primarily responsible for the overall growth of the crystalline lens and also highly correlates with the increase in the back-scattered signal. Finally, I was able to visualize lenticular suture architecture from volumetric OCT data.

The results help towards an improved understanding of the structure/function relationship of the crystalline lens, and can contribute to a better insight into the development of age-related eye diseases such as cataract and presbyopia.

# Streszczenie

Soczewka oka ludzkiego jest dwuwypukłym elementem refrakcyjnym, którego kształt może ulegać zmianom. Zbudowana jest ona z koncentrycznych warstw wydłużonych komórek, tworzących tzw. jądro oraz korę soczewki. Soczewka podlega różnorodnym procesom starzenia, które wpływają na zmianę jej właściwości strukturalnych, optycznych oraz biomechanicznych, prowadząc do stopniowego pogorszenia widzenia. Ciągły wzrost oraz przyrost liczebności włókien soczewki skutkuje nieustanną przebudową morfologii soczewki, manifestujący się w zwiększeniu jej rozmiaru i wagi. Dodatkowo, wysoka przezroczystość soczewki oka ludzkiego jest osiągnięta dzięki specyficznej budowie strukturalnej soczewki, a następujące z wiekiem zmiany molekularne zachodzące w soczewce prowadzą do zwiększonego wewnątrzgałkowego rozpraszania światła.

Niniejsza praca miała na celu charakteryzację oraz opis ilościowy zmian w soczewce oka ludzkiego poprzez pomiar światła rozproszonego wstecznie oraz w przód w grupie zdrowych ochotników oraz powiązanie tych zmian ze zmianami jakości widzenia. W pracy tej skoncentrowano się na następujących zjawiskach: (1) zmiany kształtu soczewki z wiekiem, (2) stopniowa zmiana przezroczystości soczewki (rozproszenia światła) oraz osłabienie jakości widzenia, (3) występowanie niejednorodności optycznych w soczewce związanych ze sposobem organizacji komórkowej. W badaniach użyto instrumenty obrazujące takie jak tomografia optyczna OCT przedniego odcinka oka oraz układ podwójnego przejścia do prezentacji funkcji odpowiedzi punktowej oka. Metody te pozwoliły na wizualizację struktury trójwymiarowej oka oraz pomiar rozpraszania wewnątrzgałkowego.

Podjęte badania przekrojowe pokazały, że cechy morfologiczne soczewki, takie jak grubość i promień krzywizny, zmieniają się wraz z wiekiem. Jakość optyczna oka ulega również pogorszeniu, co jest związane ze wzrostem rozpraszania światła w oku. W kolejnej części pracy przeprowadziłem analizę tzw. warstw (obszarów) nieciągłości optycznych w soczewce, które zostały zidentyfikowane na obrazach OCT w oparciu o

tz. system nomenklatury oksfordzkiej (tj. jądro i warstwy korowe C1 $\alpha$ , C1 $\beta$ , C2, C3 i C4). Badania wykazały, że jasna warstwa C3 jest głównie odpowiedzialna za zwiększenie grubości soczewki, a zmiany w niej zachodzące mają istotny wpływ na wzrost natężenia światła rozpraszane wstecznie. W ostatniej części pracy pokazałem, że trójwymiarowe dane OCT umożliwiają wizualizację struktury tzw. szwów soczewkowych.

Wyniki badań przyczyniają się do oceny zależności pomiędzy strukturą a funkcją soczewki, a tym samym do zrozumienia procesów rozwoju chorób oka związanych ze starzeniem, takich jak zaćma czy starczowzroczność.

# Acknowledgements

With a great sense of achievement and pleasure, I am concluding the academic chapter of my life. This has been a long and fulfilling journey, and I am incredibly grateful to all the individuals who have contributed to my success.

I am deeply grateful to Dr. Arun Kumar, my mentor during my Master's studies, for his unending support throughout my academic journey. Without his guidance, pursuing doctoral studies would not have been possible. My heartfelt appreciation also goes out to my parents, Dr. Ram Kumar Gupta, MD and Dr. Kamlesh Gupta, MD whose love, faith, and motivation have enabled me to step out of my comfort zone and embark on this challenging journey in a foreign land. Their belief in me has been the driving force behind my success, and I will always be grateful to them.

My supervisor, Dr. hab. Ireneusz Grulkowski provided me with the opportunity to pursue my doctoral studies under his guidance, for which I am grateful. His support, guidance, and encouragement throughout my research projects have been invaluable. Dr. Daniel Ruminski, my co-supervisor, has also been an essential part of my academic journey, sharing his technical expertise and different approaches to solving problems during experiments. I also appreciate Dr. Pablo Artal for providing access to his lab, LOUM Murcia Spain, where we could get all the data for my research. I am truly grateful for their contributions to my academic journey.

I would also like to express my heartfelt appreciation to my friends and colleagues who have been a pleasure to work with and provided their support in many ways. Dr. Alfonso Jimenez Villar was instrumental in obtaining data from Murcia, Spain, and shared his expertise in ophthalmic biometry. Dr. Grzegorz Gondek has also been a supportive friend who helped me settle down in Poland and served as my best man at my wedding. Dr. Ewa Maczynska-Walkowiak and Dr. Spozmai Panezai provided invaluable ideas that significantly improved my presentations and articles.

Finally, my wife, Dr. Justyna Gupta, deserves special mention for providing me with unwavering emotional support and encouragement during my doctoral journey. Her presence has been a constant source of strength for me, and I am deeply grateful for her patience in listening to my complaints and offering valuable advice to help me navigate this journey. I thank her from the bottom of my heart for being a pillar of support throughout this experience.

I would like to dedicate my dissertation to my beloved family, in-laws, and friends who have been my source of strength throughout this journey. I look forward to the next phase of my life, where I will apply the knowledge and skills I have gained to positively impact the world.

## **Motivation, hypothesis and aims**

Ageing is a natural process that occurs in all living organisms. It involves the gradual decline of physiological functions and the onset of various degenerative diseases. The effects of ageing on the human body are multifaceted, affecting various organs and systems. One of the most notable changes that occur with ageing is a loss of muscle mass and strength, known as sarcopenia. Other changes that occur with ageing include decreased bone density, osteoporosis, and an increased risk of cardiovascular disease, diabetes, and cancer. The immune system also undergoes changes with ageing, the thymus, which is responsible for producing T-cells, decreases in size and function with age, leading to a decline in the ability to mount an immune response. The ageing process also affects the human brain and mind, leading to a decline in cognitive function and an increased risk of dementia. As we age, the brain undergoes a series of structural and functional changes, including a decrease in the size of the brain and a decrease in the number of neurons and synapses. One of the most significant risks associated with ageing is the increased risk of dementia, including Alzheimer's disease.

The complex optical system of the human eye involves multiple structures and processes that work together to create the sense of sight. The eye is also subject to age-related changes, which can result in vision deterioration, affecting a significant percentage of the global population over 40 years of age. These changes may cause difficulties with daily activities and even lead to blindness. Visual impairment and blindness pose a significant economic burden, especially in societies of developed countries where the lifespan is generally longer. The ocular tissues undergo different degenerative processes with age, which leads to the eye diseases such as corneal degeneration, posterior vitreous detachment (due to liquefaction), and age-related macular degeneration in the retina [1]. The crystalline lens is a crucial structure of the eye that also undergoes natural ageing processes causing presbyopia and cataract – the conditions with the highest global prevalence.

Ophthalmic diagnostics serves as a key step for the determination of both the presence and progress of ocular pathologies as well as for monitoring eye disease management strategies. Modern emerging technologies represent advantages over traditional clinical methods for lens evaluation such as slit lamp examination. Recent advancements in light source and optical signal detection technologies have provided new methods with higher sensitivity and resolution than previous imaging modalities. However, several challenges have yet to be addressed to perform comprehensive investigations on which regions of the lens are primarily responsible for lenticular ageing processes [2-14]. In addition, quantitative image analysis offers the potential for an objective assessment of the optical properties of the crystalline lens.

In this dissertation, **I hypothesize that *in-vivo* optical imaging enables objective measurement of age-related changes in the crystalline lens, which in turn affects vision.**

Therefore, **the main goal of the study was to demonstrate and quantify characteristic age-related alterations in the crystalline lens by the measurement of forward- and back-scattering in healthy subjects and to associate those changes with vision degradation.**

In the cross-sectional studies, I utilized two emerging modalities – optical coherence tomography (OCT) and double-pass method (for retinal point spread function imaging) – to map and quantify age-related changes in the crystalline lens by the detection of light back- and forward scattering, respectively. Additionally, visual function was assessed with a contrast sensitivity test in adaptive optics visual simulator.

In particular, I defined the following specific aims:

- 1. To visualize and quantitatively analyse age-related changes in morphology and transparency of crystalline lens and to investigate the impact of those changes on the visual quality of the eye:** The unique morphology and transparency of the crystalline lens enables for focusing the light at the retina for clear vision. My goal was to evaluate the age-related morphological changes in the crystalline lens, specifically, its central thickness and radii of curvature, using three-dimensional OCT data. I also measured the transparency of the crystalline lens (optical densities)

and presented the corresponding age-related changes. Additionally, I evaluated the optical quality and vision quality of the eye through the use of the double-pass system and adaptive optics visual simulator.

- 2. To demonstrate the three-dimensional local optical inhomogeneities of the crystalline lens and their association with microstructural lens features:** Here, two other aspects of lens development and ageing were considered, namely lenticular sutures and optical signal discontinuity (OSD) zones. These examples represent micro-structural details of the lens and can be visualized optically as inhomogeneities in volumetric OCT images. Through quantitative and qualitative analysis, I identified the regions of the lens that dominate age-related changes, shedding light on the roles of sutures and OSD zones in the lens declining transparency with age.



# Dissertation outline

The dissertation is divided into the following chapters:

**Chapter 1:** In this chapter, I will provide an overview of the unique characteristics of the human crystalline lens, including its morphology and transparency. You will also gain an understanding of optical scattering in the eye and the microstructural features that impact the lens optical quality which are the subject of interest in this thesis. Together, we will explore the developmental stages of the lens and the crucial features that enable its function. Additionally, I will provide insights into the ageing processes that can lead to the degradation of the lenticular tissue and may contribute to eye diseases such as cataracts and presbyopia.

**Chapter 2:** In this chapter, I will introduce the clinical tools that were utilized to evaluate the status of the crystalline lens. Specifically, I will focus on optical imaging modalities used in this project that measured either the morphology or transparency of the lens. I will provide a rationale for why OCT was chosen over other imaging modalities and offer a detailed explanation of the developed swept-source OCT system, including how its characteristics were measured. Additionally, I will describe the double-pass system and the adaptive optics visual simulator that were used to clinically assess the optical quality of the eye and the vision quality.

The next three chapters demonstrate the results of my studies. Each chapter starts with the motivation and state of the art related to a specific topic. Next, the details of data acquisition and developed data analysis tools were presented. Once the results are shown, I included a critical and thorough discussion of the observed effects with the other published studies on each specific topic.

**Chapter 3:** I will present the results of the cross-sectional study aiming at the determination of changes in the shape and transparency of the crystalline lens in healthy subjects. Specifically, I will introduce the algorithm to measure the radius of curvature, central thickness and optical density of the crystalline lens. To ensure the accuracy of

these measurements, I corrected the OCT images of the lens for motion artefacts and light refraction prior to conducting the measurements. I performed a statistical analysis of age-related changes in the above-mentioned parameters and how they associate with vision quality. I also found a relation between back-scatter and forward-scatter metrics.

**Chapter 4:** I will present the optical signal discontinuity (OSD) zones, which are the unique features of the crystalline lens that appear as bright and dark zones in optical cross-sectional images. I will introduce the methodology to extract the thickness and optical density of these zones from OCT-based densitograms. The study presented in this chapter is regarded as a more detailed assessment of age-related lens alterations than that given in Chapter 3. Additionally, I will use multivariate regression analysis and Spearman correlations to demonstrate how the degradation of the crystalline lens and the OSD zones can impact the eye's overall quality measurements. This is the first comprehensive study that uses OCT data to identify OSD zones and evaluates the modifications of the OSD zones with ageing.

**Chapter 5:** In this chapter, I will focus on the unique features of the lenticular sutures. I will describe the methods used to obtain contrast-enhanced *en-face* images of the sutures and to quantify suture-like features within the lens from OCT volumetric images. To achieve this, I developed an algorithm that was compared with manual counting of the suture branches for accuracy. Additionally, I measured the transparency of the sutures and assessed their contribution to the overall signal from the cortex of the lens. Through the statistical analysis, I presented correlations between age and the suture optical density signal and overall cortex signal, which provided valuable insights into the ageing processes of the lens. This study represents the first *in-vivo* visualisation of human lenticular sutures. Throughout the chapter, I also provided context for the significance of our findings.

**Chapter 6:** In this chapter, I have provided a summary of all results obtained in the project and discussed the results concerning the hypotheses and objectives that were set at the beginning of the thesis. I also identified the limitations of the study and discussed possible ways to address them. Additionally, I have shared insights from the conclusions drawn from the study, and I discussed potential future applications and directions in the fields of ophthalmology and vision science.

# Contents

<b>Abstract</b> .....	<b>i</b>
<b>Streszczenie</b> .....	<b>iii</b>
<b>Acknowledgements</b> .....	<b>v</b>
<b>Motivation, hypothesis and aims</b> .....	<b>vii</b>
<b>Dissertation outline</b> .....	<b>xi</b>
<b>List of Figures</b> .....	<b>xvii</b>
<b>List of Tables</b> .....	<b>xxi</b>
<b>1. Introduction</b> .....	<b>1</b>
1.1 Morphology and transparency of the crystalline lens .....	1
1.2 Light scattering in the eye .....	4
1.3 Lenticular sutures: a juncture of the lens fibre ends.....	7
1.4 Role of the crystalline lens in the human ocular system.....	9
1.4.1 Development of the crystalline lens .....	10
1.4.2 Crystalline lens metabolism .....	11
1.5 Age-related diseases in the eye and crystalline lens .....	13
1.5.1 Cataract.....	14
1.5.2 Presbyopia .....	18
1.6 Optical signal discontinuity zones of the lens .....	19
1.6.1 Classification of OSD zones .....	21
1.6.2 Impact of OSD zones on the optical quality of the lens.....	21
<b>2. Optical imaging systems</b> .....	<b>23</b>
2.1 Ophthalmic assessment using various optical imaging modalities .....	23
2.2 Optical coherence tomography.....	25
2.2.1 Principle of operations of OCT. Generations of OCT systems.....	25
2.2.2 Key parameters of the SS-OCT system.....	28
2.2.3 Characteristics of the swept-source OCT system used for the study ....	32
2.2.4 Image acquisition and synchronization .....	34
2.2.5 OCT signal processing .....	35
2.3 Double-pass system for the analysis of the optical quality of the eye .....	40

2.4 Adaptive optics visual simulator .....	43
2.4.1 Subjective refraction errors .....	43
2.4.2 Visual acuity .....	44
2.4.3 Contrast sensitivity function .....	45
<b>3. Age-related changes in the shape and transparency of the human crystalline lens .....</b>	<b>47</b>
3.1 Motivation and aim of the study .....	47
3.2 Data acquisition.....	50
3.3 Data post-processing and statistical analysis .....	51
3.3.1 Motion artefacts correction .....	51
3.3.2 Refraction correction method with ray tracing .....	51
3.3.3 OCT-based morphometry and densitometry of the crystalline lens .....	53
3.3.4 Statistical analysis. Simple linear regression model .....	53
3.4 Results .....	54
3.4.1 Average parameters in the study group.....	54
3.4.2 Age-related changes in the morphometry and optical density of the lens and its components.....	55
3.4.3 Impact of age-related changes on the optical quality of the eye and visual function.....	57
3.5 Discussion .....	58
<b>4. Changes of optical non-homogeneity of the crystalline lens with age. Optical signal discontinuity zones.....</b>	<b>63</b>
4.1 Motivation and aim of the study .....	63
4.2 Data acquisition.....	64
4.3 Data post-processing and statistical analysis .....	64
4.3.1 Densitogram .....	64
4.3.2 Multivariate linear regression (MLR) model.....	65
4.3.3 Statistical analysis .....	67
4.4 Results .....	68
4.4.1 Average parameters in the study group.....	68
4.4.2 Age-related changes in the thickness and transparency of OSD zones .....	68
4.4.3 Factors influencing lens thickness and optical density .....	71
4.5 Discussion .....	72

<b>5. <i>In-vivo</i> imaging of lenticular sutures and effect of ageing on suture architecture.....</b>	<b>75</b>
5.1 Motivation and aim of the study.....	75
5.2 Data acquisition.....	77
5.3 Data post-processing and statistical analysis.....	77
5.3.1 Imaging of lenticular sutures.....	77
5.3.2 Methods of extraction of suture features.....	77
5.3.3 Comparison of manual and semi-automatic methods for suture segmentation. Bland-Altman analysis.....	80
5.3.4 Quantitative description of lenticular suture pattern.....	81
5.3.5 Statistical analysis.....	81
5.4 Results.....	82
5.4.1 Suture visualization strategies from volumetric OCT data.....	82
5.4.2 Agreement between semi-automatic and manual method of suture extraction.....	84
5.4.3 Suture patterns in ageing lenses.....	85
5.4.4 Age-related changes in the crystalline lens suture patterns.....	86
5.5 Discussion.....	88
<b>6. Summary, limitations, and future scope. Conclusions.....</b>	<b>93</b>
6.1 Summary.....	93
6.2 Limitations.....	94
6.3 Future scope.....	97
6.4 Conclusions.....	98
<b>References.....</b>	<b>101</b>
<b>Appendix A.....</b>	<b>115</b>



# List of Figures

<b>Figure 1.</b> Anatomy of the crystalline lens. ....	2
<b>Figure 2.</b> Schematics of light scattering in the eye. ....	5
<b>Figure 3.</b> Angular distribution of scattered light for Rayleigh and Mie scattering. ....	6
<b>Figure 4.</b> Schematic diagrams showing the formation of suture patterns; (a) simple umbilical, (b) line, (c) Y-shaped, and (d) complex star-shaped sutures. ....	7
<b>Figure 5.</b> The eye as an optical imaging system where the (a) crystalline lens is relaxed to view a distant object, and (b) crystalline lens accommodates (thickens) to view a nearby object. ....	9
<b>Figure 6.</b> Formation of the crystalline lens from gestation till birth. ....	11
<b>Figure 7.</b> Nutrition microcirculation of the crystalline lens and arrows point to the direction of circulation of ions. ....	12
<b>Figure 8.</b> (a) A healthy crystalline lens and light focused at a singular point on the retina. (b) A cataractous crystalline lens and focused light are scattered at multiple points on the retina. ....	17
<b>Figure 9.</b> (a) Light focused by the healthy crystalline lens on the retina, and (b) presbyopic crystalline lens behind the retina. ....	18
<b>Figure 10.</b> Scheimpflug image of the eye of a 51-year-old female. Using the densitogram above the image, 8 different zones can be distinguished. Using the local maximums of the gradient of the densitogram under the picture, three different cortical zones (C1–C3) can be defined according to the Oxford system. ....	20
<b>Figure 11.</b> (a) A Michelson interferometer with a broadband light source. An integrated interference signal from each interface (P <sub>1</sub> , P <sub>2</sub> , P <sub>3</sub> and P <sub>4</sub> ) is detected at the detector. (b)	

An interferogram showing the positions of the interfaces is retrieved from the real function of the fast Fourier transform (FFT) of the integrated interference signal. .... 26

**Figure 12.** Schematic diagram of a conventional wavelength swept laser. .... 29

**Figure 13.** Swept-source OCT system schematics..... 33

**Figure 14.** Axial resolution ( $\Delta z$ ), lateral resolution ( $\Delta x$ ), and depth of field (b). ..... 33

**Figure 15.** Synchronisation of galvo scanners with the data acquisition in three-dimensional raster scan protocol. .... 34

**Figure 16.** Flow chart for swept-source OCT signal processing. Raw data acquired is when non-linearly k-sampled, then the data undergoes resampling and interpolation process to get linearly k-sampled, and when data is acquired with k-clock, then it is directly interpolated in linearized k-spaced. The numerical dispersion compensation algorithm is used to get the correct point spread function. After taking FFT, complex data is generated that can be used to generate 2D/3D intensity and/or phase images (depending on the application). .... 35

**Figure 17.** Double-pass OQAS scheme. .... 41

**Figure 18.** Selection of ROI and computing intensity radial average using double pass image for (a) the healthy eye, and (b) the eye with intraocular scattering. .... 42

**Figure 19.** Schematic diagram of Adaptive optics visual simulator. .... 44

**Figure 20.** (a) Sinusoidal gratings with 100% and 50% contrast levels with a spatial frequency of 3 cycles/degree. (b) The sinusoidal gratings with orientations, 45° (left) and 135° (right), with different contrast levels, were presented to the subject in random order. (c) The area under logarithmic contrast sensitivity function (AULCSF) for a 17 year old subject. .... 46

**Figure 21.** (a) Original OCT B-scan of the crystalline lens of a 49-yo subject. (b) Refraction correction of the central B-scan. The surfaces of the anterior and posterior of the lens (solid yellow) and the nucleus (dashed yellow) were used to measure the radii of curvature (yellow arrows), and the central thickness (black double-side arrows). (c) Region of interest to measure the optical density of the lens, cortex, and nucleus.52

**Figure 22.** Age dependence of measured (a) thickness of nucleus, cortex, and whole lens, (b) radii of curvature of the anterior and posterior lens capsules and the lens nucleus, and (c) optical density of the nucleus, cortex, and lens. .... 57

**Figure 23.** (a) Schematic diagram of the crystalline lens (left half: structure of the crystalline lens, and right half: OSD zones) and ROI (red) for generating densitogram for the zones. The epithelial layer is not given in scale. (b) Three-dimensional swept-source OCT volumetric ( $8 \times 8 \times 7 \text{ mm}^3$ ) dataset of a 49-year-old subject. (c) Refraction correction of the central B-scan. The surfaces of the anterior and posterior of the lens (solid yellow) and the nucleus (dashed yellow) were used to measure the radii of curvature. (d) Densitogram of the lens and identification of the OSD zones based on Oxford system nomenclature. The thickness and optical density were measured for each zone. .... 65

**Figure 24.** Relation of ageing with changes in the anterior and posterior thickness of the cortex and its sub-layers (C1, C2, C3, and C4)..... 70

**Figure 25.** Percentage contribution of cortical layers to the total cortical thickness for different age groups. .... 71

**Figure 26.** (a) Anatomy structure of the human crystalline lens. (b) OCT volumetric data of the crystalline lens of  $8 \times 8 \times 4 \text{ mm}^3$ . (c) Illustration of the segmented cortex and generation of average intensity projection (AIP) image of the anterior cortex. Star-shaped sutures are visible in AIP image. .... 78

**Figure 27.** Flow chart of the image processing and extraction of suture pattern algorithm; averaged intensity *en-face* projection of anterior lens suture, image contrast enhancement with bandpass filtering and CLAHE (contrast limited adaptive histogram equalisation) contrast enhancement, image binarisation, image skeletonisation, pruning ends and false branches..... 79

**Figure 28.** (a) Cross-sectional segmentation of cortex and nucleus, (b) AIP projections of segmentations reveal sutures at: anterior cortex – star-shaped sutures (green), anterior fetal nucleus – Y sutures (yellow), posterior fetal nucleus – Y sutures (red), and posterior cortex – star-shaped sutures (blue). (c) 3-D suture architecture in the whole crystalline lens. Data presented here is the anterior crystalline lens from the right eye of a 40-yo subject. .... 83

**Figure 29.** Anterior (green) and posterior (yellow) suture pattern in the crystalline lens of the right eye of a 40-yo subject. **(a)** Representation in the Cartesian coordinate system. **(b)** Representation in the polar coordinate system. .... 83

**Figure 30.** Enhanced-contrast AIP of the right eye of the 28-yo subject. Red arrow clearly shows non-homogenous nature of light scattering in suture region. .... 84

**Figure 31.** Validation of the algorithm for suture pattern extraction. Comparison and agreement between semi-automatic algorithm and manual grading of the AIP images: **(a)** anterior lens sutures and **(b)** posterior lens sutures. The plots demonstrate the correlation between the detected number of suture branches (left column) and Bland-Altman plots (right column). .... 85

**Figure 32.** The crystalline lens and suture pattern in the ageing eye. OCT cross-sectional image (upper row), AIP images (middle row) and extracted anterior suture patterns (bottom row) of human lenses in different decades of human life. .... 86

**Figure 33.** Quantitative analysis of the human lens suture pattern *in-vivo*. **(a)** Relation between the number of branches in the posterior lens and the number of branches in the anterior lens. The dashed line represents the equality of the numbers. **(b)** Age-related changes in the number of branches. **(c)** Age-related changes of the suture density index. **(d)** Age-related changes in the mean signal of the anterior cortex and the anterior suture pattern derived from AIP images. **(e)** Age-related changes in the mean signal of the posterior cortex and posterior suture pattern derived from AIP images..... 87

## List of Tables

<b>Table 1.</b> Age-related changes in the lens thickness in <i>in-vivo</i> studies. ....	48
<b>Table 2.</b> Age-related changes in lens transparency. ....	49
<b>Table 3.</b> Mean and standard deviations of the measured parameters.....	55
<b>Table 4.</b> Correlation of measured parameters with age.....	56
<b>Table 5.</b> Spearman’s correlation between the measurements from OCT, OQAS and VAO. ....	58
<b>Table 6.</b> Mean and standard deviations of the thickness and optical density of lenticular OSD zones from the 49 eyes.....	68
<b>Table 7.</b> Correlation of measured parameters with age.....	69



# Chapter 1

## Introduction

The human eye is a complex optical system that consists of a series of structures and media. The ocular structures enable formation of a sharp image of an object onto the retina, where the light is converted into electrical signals that our brain interprets as visual images. The eye's natural lens, also called the crystalline lens, is an important part of the eye's anatomy that allows the eye to focus on objects at varying distances. It is located behind the iris and in front of the vitreous body. The crystalline lens is a highly transparent and complex tissue that grows throughout life and continuously goes through biochemical changes. The age-related changes in the lens change the morphology and transparency of the lens which eventually affects the vision process. To understand the ageing of the lens, it is essential to first understand the morphology and the features responsible for the transparency of the lens [7, 15, 16]. The morphology and transparency of the lens depend on how the lens is developed and the microstructures within the lens.

### 1.1 Morphology and transparency of the crystalline lens

The crystalline lens is an avascular, biconvex, and transparent structure that is composed of specialized cells called lens fibres. The lens fibres are long, thin cells that are packed tightly together, forming concentric layers that resemble the rings of an onion. The fibre cells are arranged in a radial pattern, with the outermost fibres originating from the anterior pole of the lens and the innermost fibres originating from the posterior pole. These layers are called lamellae, and they are arranged around a central core called the nucleus. The lens fibres are held together by a delicate network of intercellular junctions called sutures (Fig. 1).

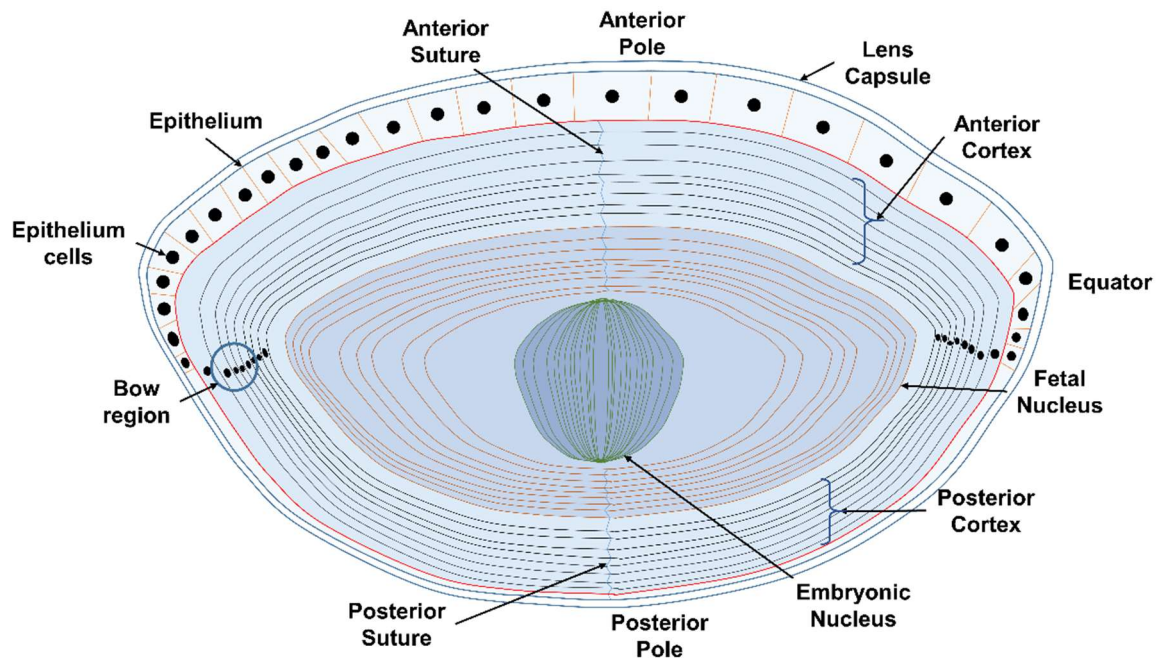


**Figure 1.** Anatomy of the crystalline lens.

The lens fibres are constantly being added to the lens throughout life. The crystalline lens grows with age because the primary and secondary fibre cells continuously differentiate to add elliptical fibre cells throughout the lens [7, 10, 17]. The addition of new lens fibres towards the lens periphery makes it more convex. That is, the crystalline lens curvature declines with age as it becomes thicker. The average lens size in adults is approximately 10 mm across and 4 mm from front to back.

Generally, the lens is comprised of a very high concentration of proteins (sometimes exceeding 450 mg/ml) [17]. Proteins make up nearly 60% of the eye's lens which is a higher protein concentration than any other bodily tissue [2, 18, 19]. The lens fibre cell cytoplasm has specialized proteins called crystallins, which are responsible for maintaining its transparency. Crystallins provide about 90% of the soluble proteins in the crystalline lens. The crystallins account for 38% of the wet weight of the lens [2, 18]. As new fibres are added at the outer edge of the lens and old fibres are pushed towards the centre, a gradient of fibre density can be observed inside the lens, with the outer fibres being less dense than the inner fibres. This results in the gradient of crystallins concentration. Along with a non-uniform growth rate of the lens layers, the gradient of distribution of crystallins develops a gradient of refractive index (GRIN)

distributed such that the highest refractive index is at the centre and the lowest is at the lens periphery [20, 21]. The crystallins are also arranged in a highly organized pattern, with different types of crystallins localized to specific regions of the lens [2, 18, 22].

The transparency of the lens is maintained by several mechanisms. First of all, to keep the lenticular physical phenotype and maintain transparency, the differentiated lens fibres are arranged in high order such that the light scattering losses are minimized [7, 10, 17]. During differentiation, the fibre cells undergo the elimination of nuclei and organelles so that there is no refractive index mismatch across the cells (Fig. 1) [2, 18, 22]. Moreover, the high concentrations of crystallins in the centre of the lens and the specific arrangement of crystallins make the lens highly transparent [23, 24]. Those factors decide on a relatively uniform refractive index at the cellular and sub-cellular levels. This means that ideally light passing through the lens is not scattered, and the lens is not opaque.

Another mechanism for maintaining transparency is the circulation of nutrients and waste products within the lens. The lens is avascular, meaning that it does not contain blood vessels. Instead, nutrients and waste products are transported to and from the lens through the aqueous humour. The lens metabolism is maintained by micro-circulation, which begins at the extracellular spaces of the sutures and helps to remove any proteins or other substances that may accumulate within the lens, which could potentially interfere with its transparency.

In nuts-shell, human lens formation goes through an asymptotic growth phase before birth, and lens growth is linear after birth. The crystalline lens transparency is facilitated by the unique cellular architecture of the lens, the absence of blood vessels, the removal of cellular organelles (including cellular nuclei) that minimises the extracellular space, and the matching of the refractive index between the membranes and the cytoplasm. To maintain the transparency of the crystalline lens, the crystalline lens must be nurtured with the required ions and maintain water content [25-30].

## 1.2 Light scattering in the eye

As media for light propagation, most human tissues are considered turbid (i.e., “cloudy” or opaque). However, the eye is the most transparent human organ, which allows maximum light penetration with safe optical power. Light scattering is a phenomenon that occurs due to small-scale inhomogeneities (such as the collagen fibrils in the cornea, the lens proteins, etc.) within the ocular media, whose refractive indices with respect to the surrounding media modify the original trajectory of the incident light inside the eye. These inhomogeneities will affect light propagation within the eye and degrade the retinal image quality. Understanding scattering in the eye is crucial for developing ophthalmic optical imaging techniques that can diagnose and monitor eye diseases.

When light is incident on soft matter, the molecules in the matter absorb light partially and rest is radiated as scattered light. Each molecule acts as a point source of scattered light in all directions. Depending on interference with the light waves emitted by molecules in the surrounding, the overall scattering can be directional. Two main types of directional scattering that occur in the eye are: forward scattering and backward scattering [15, 31].

Forward scattering occurs when light is scattered in the forward direction with scattering angle of smaller than  $90^\circ$ , i.e. away from the direction of the incident light. This type of scattering is important in determining the transparency of the cornea and crystalline lens [32, 33]. For a healthy eye, the contribution of forward scattering by the cornea, iris, crystalline lens, and retina is 30%, 5%, 40%, and 20%, respectively of the total scattered light. The forward scattered light intensity can be determined by:

$$I_f = I_0 \times \exp(-\mu_t z), \quad (1.1)$$

where  $I_0$  is the light intensity incident on the sample,  $\mu_t$  is the total attenuation coefficient, and  $z$  is the distance travelled by the light. The main effect of forward light scattering is the reduction of the retinal image quality by introduction of glare in the vision. As a consequence, contrast sensitivity of the eye is lower.

Backward scattering, on the other hand, occurs when light is scattered at over more than  $90^\circ$ , or in the backward direction, towards the direction of the incident light [33]. The backward scattered light intensity is given by:

$$I_b = I_f - (I_0 \times \exp(-\mu_a z)), \quad (1.2)$$

where  $I_0$  is the light intensity incident on the particle,  $\mu_a$  is the absorption coefficient, and  $z$  is the distance travelled by the light.

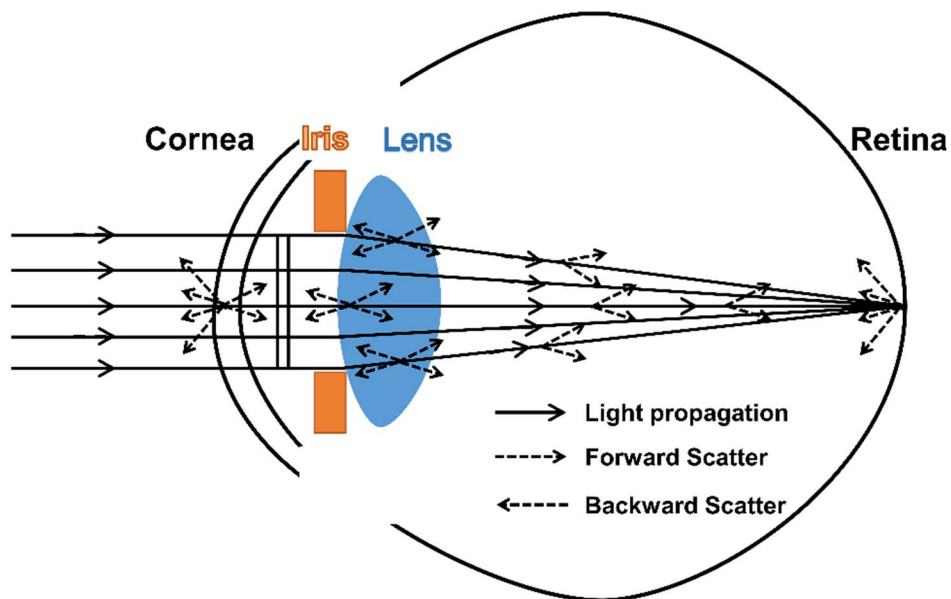


**Figure 2.** Schematics of light scattering in the eye (adapted from [32]).

The mechanisms underlying forward scattering and backward scattering are different and depend on the size and shape of the scattering particles (Fig. 2). The particles much smaller than wavelength scatter about equally in forward and backward directions; larger particles scatter more strongly in forward direction. The particles dominating backward scatter in the human eye lens are much smaller than the wavelength. The particles dominating forward scatter have sizes of the order of wavelength are due to Mie scattering (Fig 3.). Physically, intraocular scattering can be complex and also depends on the refractive index of the scatterers with respect to their surrounding media [33-35]. Mie scattering is roughly dependent on the wavelength of

light, and its intensity is proportional to the size of the scattering particle. In this case, the scattered light is not isotropic but rather depends on the angle of scattering [36].

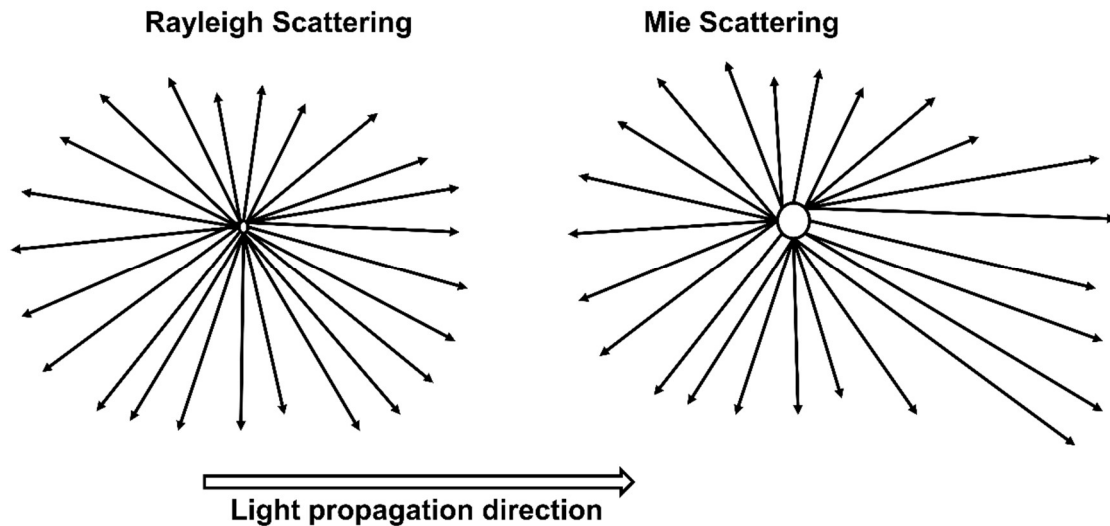


**Figure 3.** Angular distribution of scattered light for Rayleigh and Mie scattering.

When the scatterers are much smaller than the wavelength of light, the Rayleigh approximation can be used. Rayleigh scattering occurs in both forward and backward directions (Fig. 3). For small particles, such as those found in the cornea and crystalline lens, Rayleigh scattering is the dominant mechanism of scattering. The intensity of Rayleigh scattering is inversely proportional to the fourth power of the wavelength of light, which means that shorter-wavelength light is scattered more strongly than longer-wavelength light. In this case, the scattered light is isotropic, meaning that it is scattered equally in all directions. This is why the cornea and crystalline lens, which are made up of small scattering particles, appear transparent to visible light [15, 37-39].

Ophthalmic optical imaging techniques based on scattering are powerful tools for diagnosing and monitoring eye diseases. These techniques make use of the scattering properties of the various structures within the eye to obtain high-resolution, non-invasive images of these structures. Some of the most commonly used ophthalmic optical imaging techniques based on scattering detection include optical coherence tomography (OCT), confocal microscopy, and Scheimpflug imaging.

### 1.3 Lenticular sutures: a juncture of the lens fibre ends

Lenticular sutures constitute the surfaces where anterior or posterior fibre ends meet each other. The study of lenticular sutures has revealed complex lens growth throughout life. Previous studies of the lens suture anatomy observed the lens growth's complexity by studying the suture patterns during infancy, adolescence, and adulthood [40, 41]. The sutures can be categorised based on their structural complexity as umbilical / central point, line, y-shaped, and star-like (Fig. 4).

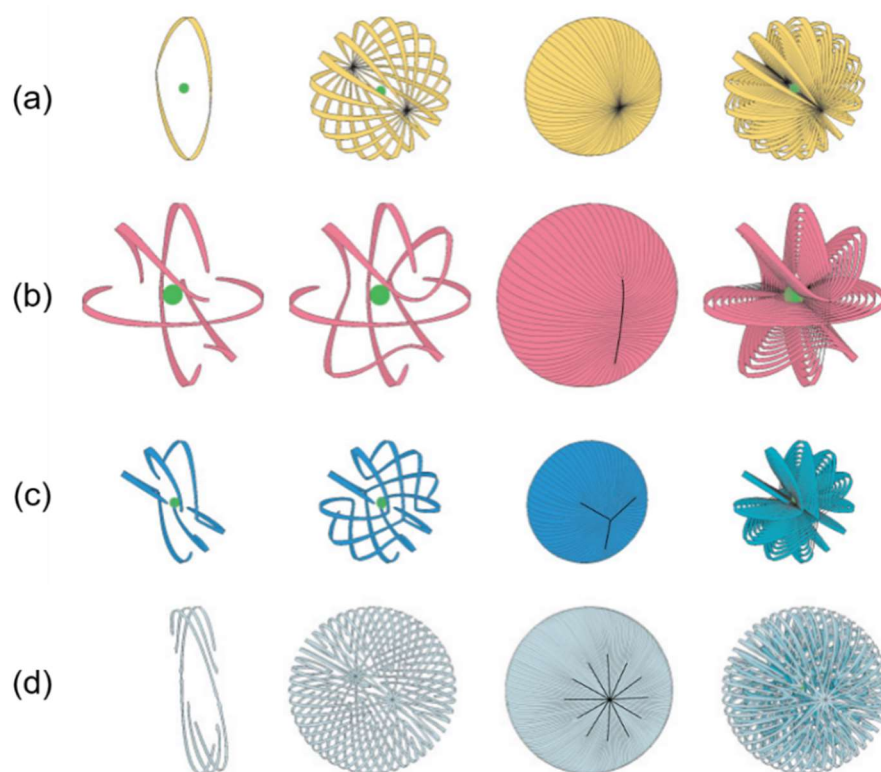


**Figure 4.** Schematic diagrams showing the formation of suture patterns; (a) simple umbilical, (b) line, (c) Y-shaped, and (d) complex star-shaped sutures [41].

**Umbilical/central point suture:** The simplest lens suture characteristic of birds, reptilians, some amphibians, and fish lenses. These lenses have fibres with identical growth and pass through the polar axis of the lens. The anatomical appearance would be a point at the centre (Fig. 4a).

**Line, y-shaped, and star-like sutures:** The lens fibres with these sutures do not extend from one pole to another pole of the lens, like lenses with umbilical sutures. Instead, the suture pattern begins at a pole and branches out towards the equator of the lens along the curvature of the layer of the lens. The line sutures are characteristic of many fish, sharks, rays, frogs, and small mammals like mice, guinea pigs, and rabbits. As the name suggests, line sutures appear as horizontal and vertical lines on the anterior and posterior surfaces of the lenticular layers (Fig. 4b).

Y-shaped sutures anatomically include three suture branches forming a ‘Y’ on the anterior lens surface (embryonic nucleus). On the posterior surface, three suture branches form an inverted ‘Y’. The Y-sutures are seen in the young eyes of large mammals, including humans (Fig. 4c).

The complex star-shaped sutures are seen in large adult mammals, including humans. More than three branches characterise the star-shaped sutures and also have further sub-branches (Fig. 4d). The star-shaped suture branches are more extended than line and y-shaped sutures. The anterior and posterior branches of the line, y-shaped and star-shaped sutures, are rotated to each other by  $90^\circ$ ,  $60^\circ$ , and  $20^\circ$  (approximately), respectively [41].

Ideally, the lens would be a perfect, spherical structure that would refract the light perfectly and focus it onto the retina. However, the lens is not a perfect structure, and several factors can contribute to light scattering and aberration. One of these factors is the presence of sutures, which create interfaces between the different lens fibres that can scatter the light.

The arrangement of sutures at the poles of the lens is particularly important in reducing light scattering. The sutures at the poles are arranged in a highly ordered, symmetrical pattern that radiates out from the centre of the pole [41]. This arrangement helps to minimize the number of interfaces between the different lens fibres that the light must pass through. When the light encounters an interface between two different lens fibres, some of it is reflected and scattered, leading to a loss of image quality. By minimizing the number of interfaces, the suture pattern at the poles reduces light scattering and improves image quality [40, 42].

In addition to reducing the number of interfaces, the suture pattern at the poles is also optimized to reduce spherical aberration, which is another factor that can contribute to light scattering. Spherical aberration occurs when light rays passing through different parts of a spherical lens converge at slightly different points, leading to blurring and distortion of the image. The angle of the sutures at the poles is optimized to reduce spherical aberration by ensuring that the light passing through the lens is focused onto the retina with minimal distortion [26, 40, 42, 43].

## 1.4 Role of the crystalline lens in the human ocular system

The human ocular system comprises refractive elements like the cornea and the crystalline lens, allowing the image of the object to be generated on the retina via the ocular media (i.e. aqueous and vitreous humour). About two-thirds of the eye's focusing power is due to corneal refraction, and one-third is due to the crystalline lens [7, 44, 45]. The crystalline lens plays also a critical role in the ocular system by adjusting its shape to focus light onto the retina. This process, known as accommodation, is essential for clear vision at varying distances [9, 10, 44-46]. When we look at objects up close, the crystalline lens becomes more convex, allowing it to focus light onto the retina. Conversely, when we look at objects far away, the lens becomes less convex, enabling us to see distant objects clearly (Fig. 5).

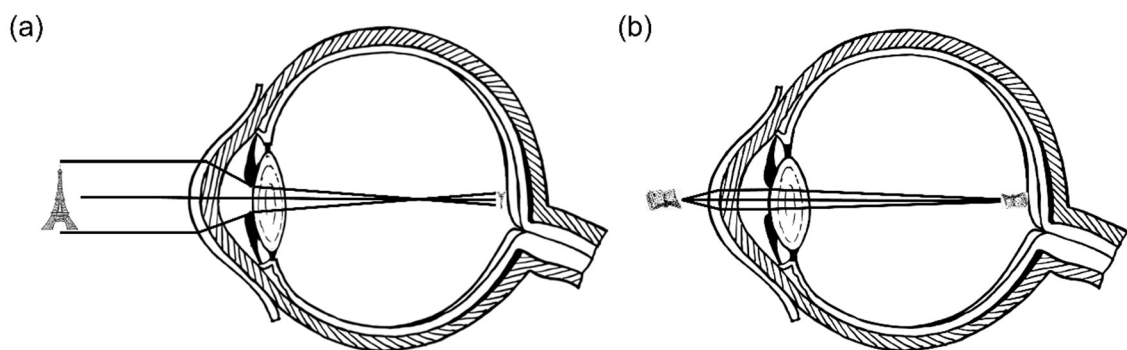


**Figure 5.** The eye as an optical imaging system where the **(a)** crystalline lens is relaxed to view a distant object, and **(b)** crystalline lens accommodates (thickens) to view a nearby object (adapted from [47]).

The ability of the crystalline lens to change the shape is due to the contraction of the ciliary muscle located around the lens. When the ciliary muscle contracts, it relaxes the tension on the zonular fibres, allowing the lens to become more rounded and increase its refractive power. Conversely, when the ciliary muscle relaxes, it increases the tension on the zonular fibres, causing the lens to flatten and decrease its refractive power [9, 46, 48, 49].

In addition to its role in accommodation, the crystalline lens also plays a crucial role in protecting the eye from harmful UV radiation. The lens is capable of absorbing UV radiation, preventing it from reaching the sensitive structures of the eye, such as the retina [50-54].

The ciliary body also produces aqueous humour, which keeps the lens healthy and functioning. Aqueous humour is the clear fluid located between the cornea and the lens that flows through the eye and then drains from the eye through the trabecular meshwork [55, 56]. The lens relies on aqueous humour for energy and cleansing rather than nerves or blood flow [50, 57, 58].

However, a correct vision process is not only dependent on the refractive properties of the ocular tissues (cornea and lens) and ocular media but also linked to the transparency of all elements in the optical path. The high concentrations of water-soluble proteins, called crystallins, in the fibre cells, are responsible for providing transparency to the lens. The crystalline lens transparency and gradient of refraction depend on its complex architecture and cellular functioning, which changes throughout age [15, 17, 59].

### **1.4.1 Development of the crystalline lens**

The crystalline lens perpetually grows throughout life. The eye develops in early pregnancy after approximately 28 days of conception; however, the human crystalline lens develops at the sixth week of gestation. At the early stage of lens development (Fig. 6), the area of the surface ectoderm around the optic stalk thickens to form the lens placode. The lens placode sinks to form the first lenticular structure, a lens vesicle that is composed of epithelial cells. On the 33<sup>rd</sup> day of gestation, the lens vesicle separates

from the surface ectoderm. The lens vesicle is covered with basal lamina and comprises single-layer cells. The posterior epithelial cells elongate to form primary lens fibre cells. The primary cells keep attached to the posterior basal lamina and grow towards the anterior lens epithelium. The primary lens fibre cells form the central nucleus between the seventh and eighth week after gestation.

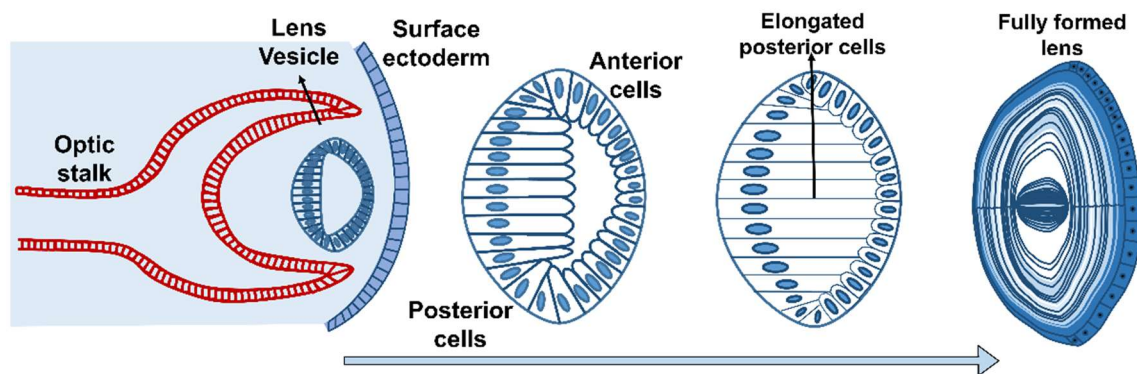


**Figure 6.** Formation of the crystalline lens from gestation till birth (adapted from [61, 62]).

After birth, the epithelial cells at the lens equator continue to form secondary lens fibres [10, 50, 58, 61]. The secondary lens fibres are formed from the extensively elongated and differentiated anterior epithelial cells at the lens equator. The first secondary fibres form an enclosed layer and meet at the poles to form Y-shaped sutures. The elongated secondary fibre cells create new lenticular layers throughout life near the lens surface, while the older layers are pushed towards the central nucleus [13, 28, 42]. The highly ordered lens fibres are transformed into co-axial refractive surfaces responsible for the crystalline lens transparency. As the lens grows, the lens fibres elongate till they interface with each other from adjacent hemispheres at the anterior and posterior poles of each concentric layer to form the sutures [12-14, 43].

### 1.4.2 Crystalline lens metabolism

When the crystalline lens structural properties are established at the embryonic stage, a unique internal microcirculation channel is established without blood flow

responsible for nurturing the lens. The microcirculation channel provides nutrients to cells and removes metabolic waste. It also controls the ionic homeostasis of deeper lens cells. Therefore, the transparency of the crystalline lens is maintained by eliminating the potential sources of light scattering [59, 63, 64]. The internal microcirculation system utilises ionic and fluid fluxes to deliver nutrients and remove metabolic wastes via extracellular spaces to deeper lens fibre cells (Fig. 7).

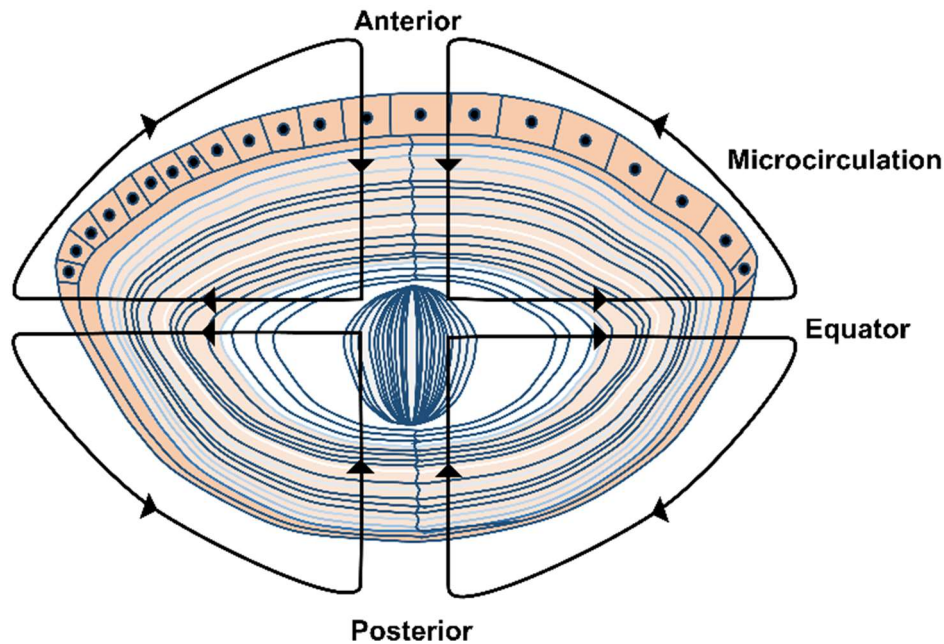


**Figure 7.** Nutrition microcirculation of the crystalline lens and arrows point to the direction of circulation of ions (adapted from [65-67]).

The diffusion of water, ions, and nutrients is facilitated at both poles of the lens. At the poles, sutures are an integral part of the microcirculation system that is paramount for lens development and growth. The water, ions and nutrients enter the lens poles via sutures and reach uniformly to deeper nucleus fibre cells moving through suture-associated extracellular space. The fluid exits through membrane and gap junction channels at the equator while collecting metabolic waste from cells on the way out. It is hypothesised that the lens microcirculation is generated by circulating ion flux due to the lower ion density pump at the poles compared to the high density at the equator [65-67].

The microcirculation results from not only an electrochemical gradient but also a hydrostatic pressure gradient between the lens periphery and centre. This hydrostatic pressure gradient is 0 mmHg at the periphery and 335 mmHg at the centre and is assumed to be responsible for driving the fluid from the nucleus towards the periphery of the lens [68]. Thus, the lenticular sutures play an important role in providing the pathways for the nutrients to flow from poles to deep fibre cells in the nucleus and help maintain the ionic and fluid flux for keeping an open microcirculation channel.

## **1.5 Age-related diseases in the eye and crystalline lens**

With age, the eye undergoes changes that can affect its function. For example, the cornea may become thicker [3, 15, 69, 70], and the retina may become thinner and less able to detect light [71, 72]. The age-related changes lead to eye diseases that degrade the optical and vision quality of the eye and its elements including the crystalline lens.

Glaucoma is a disease that is characterized by progressive damage to the optic nerve and loss of visual function. The most common form of glaucoma, called primary open-angle glaucoma, is associated with increased intraocular pressure (IOP) [73-76]. The increased IOP damages the optic nerve, which is caused by compression of the blood vessels, leading to reduced blood flow and oxidative stress. Age-related changes in the trabecular meshwork, a structure in the eye that regulates the outflow of aqueous humour, may reduce its ability to regulate IOP, contributing to the development of glaucoma [73-76].

Age-related macular degeneration (AMD), on the other hand, is a condition that affects the macula, the part of the retina responsible for sharp, central vision. In AMD, the macula becomes damaged, leading to a loss of central vision. The exact cause of AMD involves a combination of genetic, environmental, and lifestyle factors. Age-related changes in the retinal pigment epithelium (RPE), a layer of cells that nourishes the photoreceptor cells in the retina, can contribute to the development of AMD [4, 71, 77]. As the RPE cells age, they become less efficient at clearing waste products, leading to the accumulation of toxic materials that can damage the macula.

With age, the lens fails to maintain the highly ordered arrangement of the lenticular fibres at the periphery and exposure to light throughout life, more profound lens fibres (older lens fibres) go through protein oxidation, thus, leading to the degradation of the fibre cells, causing an overall loss of transparency of the crystalline lens. These complex age-related biochemical changes the lens goes through, cause molecular structural changes in the lens fibre arrangement leading to changes in transparency and morphology [24, 45, 78, 79]. The lens starts to become less transparent and stiffer. The crystalline lens becomes inelastic leading to presbyopia. Age-related changes in the lens, such as thickening and development of opacifications, can reduce the transmission of light through the eye and increase scatter. These opacifications can also reduce the amount of light that reaches the macula, leading to reduced visual function. The presence of opacifications is clinically known as cataract.

### **1.5.1 Cataract**

Cataract is a common eye condition that affects millions of people worldwide. It is characterized by clouding of the lens of the eye, which can cause blurry vision, glare, and difficulty seeing in low light conditions. The development of cataracts is the leading cause of the degradation of vision. Heredity and senile cataracts are the leading cause of blindness worldwide [80].

#### **Causes of cataract**

Cataracts occur when the proteins in the lens of the eye clump together, forming cloudy areas that can block or scatter light as it enters the eye [18]. The cause of cataracts is believed to be a combination of genetic and environmental factors. Risk factors for developing cataracts include [80]:

- **Age:** Cataracts are primarily caused by ageing, as the proteins in the eye's lens mutate over time. These changes result in a reduction in flexibility, transparency, and ability to transmit light effectively. Typically, age-related cataracts progress slowly over several years and can impact either one or both eyes. While they can occur at any age, they are more prevalent in individuals over 60 years old [81].

- **Genetics:** Several genetic mutations can cause cataracts. These mutations can affect the genes that are responsible for the production and maintenance of the proteins that make up the lens of the eye. Some of the most common mutations associated with cataracts include [82]:

*Mutations in the crystallin genes:* Crystallin proteins are the most abundant proteins in the lens, and mutations in the genes that produce these proteins can cause cataracts. Several different types of mutations have been identified in the crystallin genes, including missense mutations, nonsense mutations, and frameshift mutations.

*Mutations in the gap junction protein alpha 3 (GJA3) and gap junction protein alpha 8 (GJA8) genes:* Gap junctions are structures that allow cells in the lens to communicate with each other, and mutations in the genes that produce the gap junction proteins can disrupt this communication and cause cataracts.

*Mutations in the beaded filament structural protein 2 (BFSP2) gene:* BFSP2 is a protein that helps maintain the structure of the lens, and mutations in this gene can cause cataracts.

*Mutations in the heat shock transcription factor 4 (HSF4) gene:* HSF4 is a protein that helps regulate the expression of genes involved in lens development, and mutations in this gene can disrupt this regulation and cause cataracts.

In addition to these genetic mutations, there are also several genetic syndromes that cause cataracts, including *Down syndrome, Marfan syndrome, and galactosemia* [83, 84].

- **Diabetes:** Cataracts are frequently caused by diabetes, especially in those who have had the condition for a long period or have poorly controlled blood sugar levels. One mechanism by which diabetes leads to cataracts is through glycation, whereby glucose molecules attach to proteins in the eye's lens, causing cloudiness over time [85]. Additionally, diabetes can cause cataracts via oxidative stress, as high glucose levels can increase the production of reactive oxygen species, leading to lens damage. Factors such as high blood pressure and cholesterol, which are linked to diabetes, can also contribute to cataract development [86, 87]. To prevent cataracts, individuals with diabetes need to work closely with their healthcare providers to manage their blood sugar levels and diabetes control.

- **Smoking:** Cataracts can be a consequence of long-term exposure to cigarette smoke. Evidence suggests that beyond the already-known risks, like diabetes and hypertension, tobacco smoke has other damaging effects on health, too. It is believed this damage is caused by oxidative stress caused by toxic chemicals in the smoke [88]. Studies reveal that smokers have an increased risk of developing cataracts when compared to non-smokers; furthermore, those who began using tobacco products at a younger age are even more vulnerable [89-91]. Although the exact mechanism behind this relationship is not fully known, it is clear that cigarettes can increase the likelihood of cataract development.
- **UV radiation:** The risk of developing cataracts is associated with being exposed to ultraviolet (UV) radiation. UVA and UVB are two distinct forms of this radiation, each impacting the eye differently; UVA has a longer wavelength, which penetrates more deeply into the eye than UVB. However, both can lead to oxidative stress [92] in the lens – a process whereby free radicals damage proteins and cause clumps or deposits that cloud and opaque the lens, thus impairing vision [93]. Long-term exposure to ultraviolet radiation can be significantly impacted by location, altitude, and time of day. To reduce the chance of suffering from a radiation-induced cataract, reduction of eye exposure through protective eyewear and conscious avoidance of peak hours of sunlight is advised [94, 95]. Along with these precautions, dietary supplements like vitamins C and E can boost antioxidant levels and offer further protection against damaging effects on the lens [96].

## **Symptoms of cataract**

The symptoms of cataracts can vary depending on the type and severity of the condition. Common symptoms of cataracts include:

- blurry or cloudy vision,
- difficulty seeing at night or in low-light conditions,
- sensitivity to glare,
- seeing halos around lights,
- fading or yellowing of colours,
- double vision,

- frequent changes in glasses or contact lens prescription.

The interaction of light with the cataractous opacities results in increased light scattering before reaching the retina. This contributes to the degradation of vision (Fig. 8).

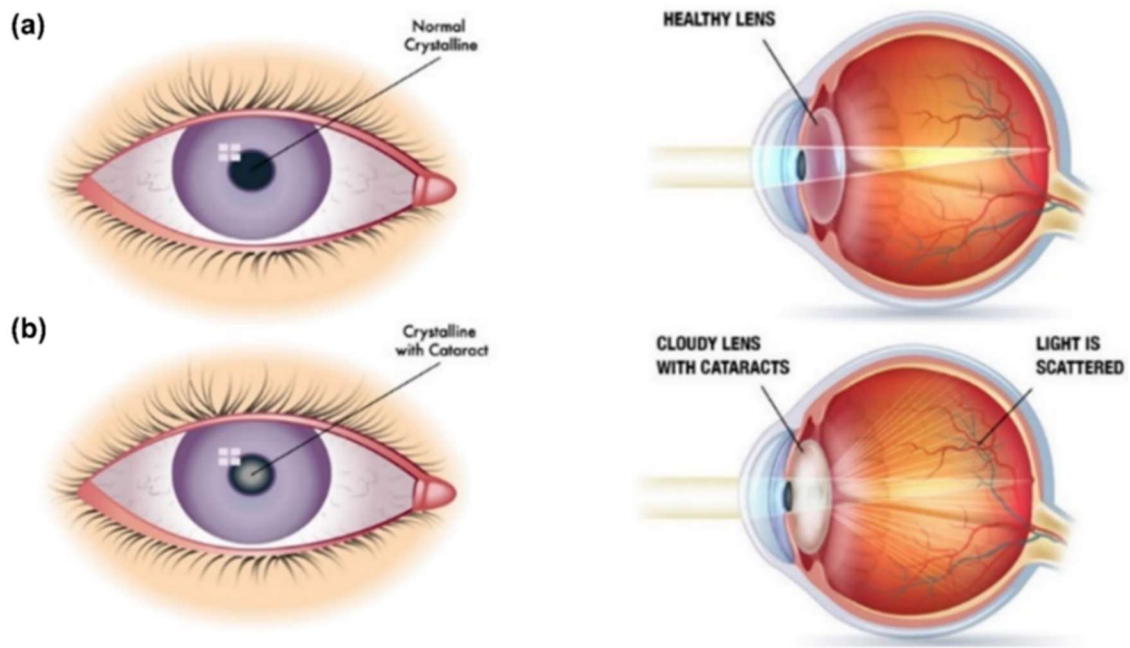


**Figure 8.** (a) A healthy crystalline lens and light focused at a singular point on the retina. (b) A cataractous crystalline lens and focused light are scattered at multiple points on the retina (adapted from [97, 98]).

### Treatment of cataract

Cataract treatment typically involves surgery to remove the cloudy lens and replace it with an artificial lens, known as an intraocular lens [99, 100]. Currently, cataract surgery is a safe and effective procedure that is performed on an outpatient basis. In addition to surgery, there are also non-surgical treatments for cataracts that may help slow the progression of the condition. These treatments include [99-101]:

- Prescription glasses or contact lenses: In the early stages of cataracts, prescription glasses or contact lenses may help improve vision.

- Anti-glare sunglasses: Anti-glare sunglasses can help reduce glare and improve vision in bright sunlight.
- Medications: Certain eye drops and medications may help slow the progression of cataracts, although they cannot cure the condition.

## 1.5.2 Presbyopia

Presbyopia is an age-related vision condition that affects individuals typically over the age of 40. It is characterised by a progressive loss of the eye's ability to focus on nearby objects (Fig. 9). This causes a refractive error leading to vision impairment, commonly known as hyperopia. The person suffering from hyperopia can see far objects with better clarity than the nearby object as light reflected from nearby objects is focused by a presbyopic lens to the plane behind the retina [102].

The condition occurs due to a natural ageing process that affects the eye's ability to change the shape of its lens to accommodate near vision. The age-related biochemical changes not only lead to the creation of opacities but also decreased elasticity of the lens. Lens hardening is caused by decreased levels of water content and  $\alpha$  crystallins with age, increasing the stiffness in the lens nucleus. Due to the stiffening of the lenticular nuclear fibres, the lens surfaces lose their flexibility to tune the focusing power [18, 104].

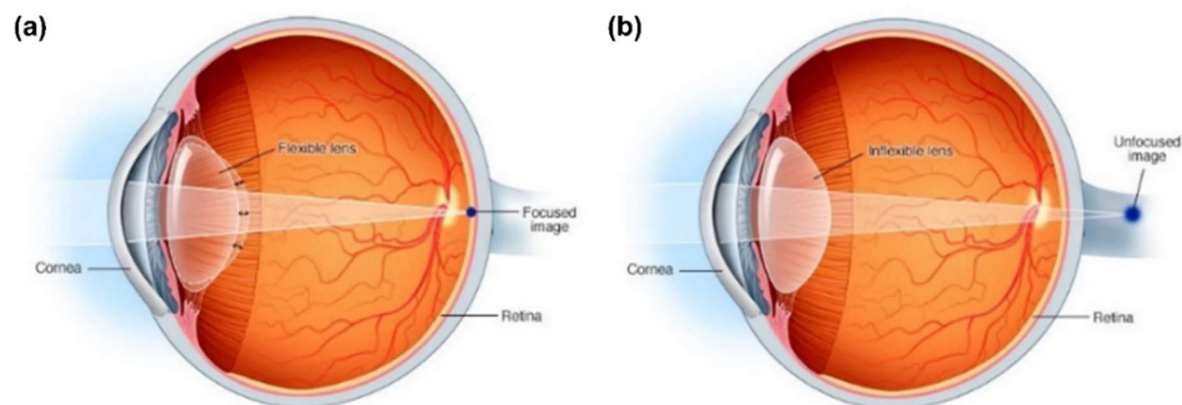


**Figure 9.** (a) Light focused by the healthy crystalline lens on the retina, and (b) presbyopic crystalline lens behind the retina [103].

## Symptoms of presbyopia [105]

The symptoms of presbyopia can include:

- blurred vision when reading or looking at objects up close,
- eye strain or fatigue when doing close work, such as reading or using a computer,
- headaches, especially after reading or doing close work for an extended period,
- difficulty seeing small print, such as on menus or labels,
- need to hold reading materials at arm's length to see them.

## Treatment of presbyopia

Presbyopia, a natural part of ageing that affects most people to some degree, can be treated with corrective lenses such as reading glasses, bifocals, or multifocal contact lenses. Surgical options like monovision laser assisted *in-situ* keratomileusis (LASIK) and conductive keratoplasty are also available but may not be suitable for everyone and carry risks [106]. Lifestyle changes such as taking frequent breaks, using good lighting, and increasing the font size on electronic devices can also help manage presbyopia.

### 1.6 Optical signal discontinuity zones of the lens

The human crystalline lens is made up of layers of fibre cells, each with its unique optical properties. Optical signal discontinuity (OSD) zones are areas within the lens where the refractive index changes at the layer-to-layer interface, causing a discontinuity in the transmission of light. The optical imaging systems reveal a number of OSD zones.

Previous studies classified the OSD zones of the crystalline lens as the embryonic, fetal, juvenile, adult nuclei, and cortex (Vogt nomenclature), based on the assumption that the nucleus is formed in various stages of life [107, 108]. The researchers at the University of Oxford, UK, developed a classification system known as the Oxford nomenclature for OSD zones. This nomenclature was designed to assess light scattering and facilitate the description of cataract locations within the crystalline lens. It was developed based on densitometric scans of Scheimpflug photographs,

providing a comprehensive framework for understanding and categorizing these zones [109]. The world health organisation (WHO) simplified cataract grading system was introduced to simplify the grading and classification of cataracts. As a result, the previous nomenclatures are no longer used [110].

Most published studies on lens internal structure and properties have used the Oxford and/or the historical Vogt nomenclature. I used the Oxford nomenclature of this study due to its simplicity. The crystalline lens is a GRIN lens, refractive index changes from the centre to the periphery, and the Oxford nomenclature is used to classify the lens into four concentric zones (C1, C2, C3, and C4) and a central nucleus based on their optical and anatomical properties (Fig. 10) [10, 109].

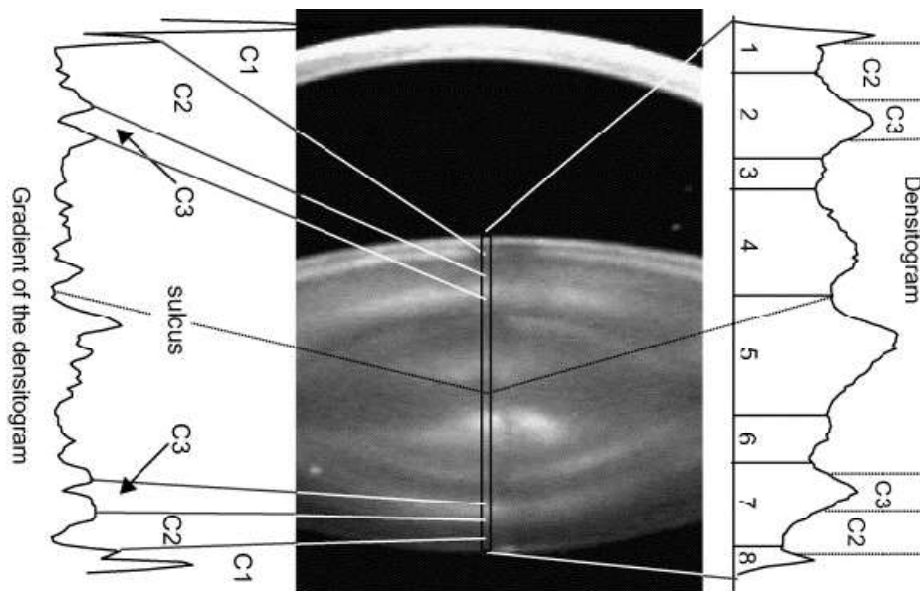


**Figure 10.** Scheimpflug image of the eye of a 51-year-old female. Using the densitogram above the image, 8 different zones can be distinguished. Using the local maximums of the gradient of the densitogram under the picture, three different cortical zones (C1–C3) can be defined according to the Oxford system [9].

### **1.6.1 Classification of OSD zones**

The lens gradient index enables it to concentrate light onto the retina directly, eliminating the requirement for extra optical components like a curved mirror or another lens. [11]. The Oxford nomenclature is used to describe the different OSD zones of the lens, based on their optical and anatomical properties.

C1 is the most anterior of the OSD zones, located at the anterior pole of the lens. It separates the lens fibres that originate from the equator from those that originate from the anterior pole and is characterized by a decrease in refractive index. The C1 zone is composed of elongated lens fibres that are packed tightly together. C2, located just anterior to the equator, separates the outer cortex from the inner cortex and has a more gradual decrease in refractive index. This zone is composed of shorter lens fibres that are arranged in a more random pattern than those in the C1 zone [12]. The C3 zone is the thickest layer of the lens, located in the central region of the lens cortex, and separates the lens fibres that originate from the posterior pole from those that originate from the equator. The C4 zone is the innermost layer of the lens cortex and has a gradual decrease in refractive index. This zone is composed of shorter lens fibres that are arranged in a more random pattern than those in the C3 zone. The nucleus is the central zone of the lens and is characterized by a high refractive index, responsible for the majority of the lens refractive power. The refractive index of the nucleus is relatively constant, and it decreases gradually towards the periphery of the lens [10-12].

### **1.6.2 Impact of OSD zones on the optical quality of the lens**

The distribution and characteristics of OSD zones can vary between individuals and even between different regions of the same lens. In general, OSD zones are more common in older individuals and are associated with the development of age-related cataracts. The presence of OSD zones in the equatorial region of the lens has been linked to the formation of posterior subcapsular cataracts [109].

The C1 zone discontinuities are related to astigmatism and irregularities in the cornea [10, 11]. C2 is also responsible for the formation of a faint dark ring in retro illumination images of the lens and its discontinuities are associated with variations in

lens power and vision quality [10, 11]. The discontinuities in the C3 zone are associated with the formation of cataracts [10, 11] and the C4 zone is related to variations in lens power and vision quality [10-12]. The nucleus is associated with the formation of cataracts and causing presbyopia.

The OSD zones' thickness and transparency can be assessed using various imaging modalities [9, 10, 12, 111]. The scattering caused by OSD zones can reduce contrast sensitivity and create halos and glare, particularly in low-light conditions [7, 15]. Therefore, the impact of OSD zones on visual function can be quantified using various imaging and psychophysical techniques, including contrast sensitivity testing and straylight measurement [15, 99].

## Chapter 2

### Optical imaging systems

#### 2.1 Ophthalmic assessment using various optical imaging modalities

As people age, the lenticular system of the eye undergoes changes that can lead to decreased transparency and elasticity. These changes can ultimately lead to the development of various eye disorders. To monitor the progression of these diseases, a variety of imaging techniques are used. These techniques involve measuring the eye's morphology [112, 113] and the axial distances among its optical components [114, 115]. Moreover, they assess the transparency and aberrations of optical wavefronts reflected from the retina and conduct psychophysical evaluations to determine the eye's visual quality [116-120].

Magnetic resonance imaging (MRI) and ultrasonography are both non-invasive imaging modalities used in ophthalmology. MRI uses a directional magnetic field, electromagnetic waves perpendicular to magnetic field, and records free-induction decay resonance signal to generate detailed images of the eye's internal structures, while ultrasonography creates ocular cross-sectional images using high-frequency sound waves. MRI has been used to obtain detailed images of the whole eye, including the crystalline lens, to evaluate its position and morphology *in-vivo* [120, 121]. Ultrasonography has been utilized clinically to diagnose and monitor various eye conditions such as cataracts, glaucoma, and retinal detachment, as well as in research to study the structure and function of the eye [57, 122, 123]. However, although MRI and ultrasound provide a long imaging depth range, they are limited by their lack of sensitivity and poor resolution. High-frequency ultrasound can improve the resolution but high frequencies suffer higher attenuation, thus limiting the penetration depth.

Optical imaging modalities offer high-resolution imaging capabilities, such as Scheimpflug photography which captures multiple cross-sectional images of the eye at different angles by rotating the camera and tilting the lens around the eye's optical axis. The concept of the camera relies on the idea of extending the depth of focus in the photography. This modality enables measurements of various parameters of the lens and can diagnose and monitor a wide range of eye conditions [5, 9, 57, 125-128].

Confocal laser scanning microscopy (CLSM) generates three-dimensional (3-D) images of internal structures using a laser beam, allowing for high-resolution imaging of the lens internal structures, such as the lenticular OSD zones, fibres, and epithelial cells [128]. Multiphoton microscopy generates high-resolution images of internal structures by exciting fluorescent molecules (like crystallins) in the lens using a high-intensity laser beam, providing detailed visualization of lens fibres and optical sectioning of the lens. Both these techniques have shallow imaging depth ranges [128] and are limited to *in-vitro* studies.

The Purkinje image-based system is another ophthalmic diagnostic tool that obtains four Purkinje images by reflecting and refracting light from intraocular structures. The images are analysed to determine the lens shape, size, and position [129].

While Scheimpflug photography offers higher resolution, it lacks sensitivity. On the other hand, CLSM, multiphoton microscopy, and the Purkinje image-based system provide very high-resolution images, but with shallow imaging depth ranges.

The laser and electronics industries have recently made significant progress, resulting in the creation of optical imaging systems like optical coherence tomography (OCT), which can produce detailed, sensitive cross-sectional images of both the anterior and posterior segments of the eye [7, 14, 111, 114, 130-133]. In addition, other systems such as the double-pass technique-based optical quality analysis system (OQAS) [117-119] and adaptive optics visual simulator (VAO) [115, 134] can assess the eye's optical and vision quality.

This chapter provides a concise overview of the imaging tools employed in my research to examine the crystalline lens, as well as to evaluate both the optical and vision

quality of the eye. These imaging tools comprise a swept-source OCT, VAO, and a double-pass configuration-based OQAS.

## **2.2 Optical coherence tomography**

OCT is an imaging modality that provides high-resolution cross-sectional images with a resolution of a few micrometres (1–20  $\mu\text{m}$ ), which is about ten times finer than high-frequency ultrasound. Unlike other imaging modalities, the resolution of OCT is not inversely related to imaging depth. Instead, a higher resolution requires a broader optical bandwidth of illuminating beam, typically provided by a femtosecond laser or a superluminescent light-emitting diode. The central wavelength of the light source chosen for OCT is usually within the tissue imaging optical windows of 800 nm, 1060 nm, or 1310 nm, which affects the penetration depth.

### **2.2.1 Principle of operations of OCT. Generations of OCT systems**

The principle of operation of OCT is similar to that of ultrasound, it measures back-scattered light from the object. The measurement is accomplished using a technique called low-coherence interferometry. In a Michelson interferometer (Fig. 11a) a light beam is split into a reference and sample arm. The backscattered light from the sample and the reflected light beam from the reference mirror is superimposed at the beam splitter. The light waves from both arms produce interference fringes on the photodetector [135, 136]. Interference can be seen over a wide range of path-length differences between the two arms for a monochromatic light source, but with the use of a low-coherence broadband source, the interference modulation only appears when the path-length mismatch is not longer than the coherence length.

OCT can be classified into two categories depending on the detection scenarios: Time domain OCT and Fourier domain OCT. In Time-domain OCT (TD-OCT), a scanning mirror is used to scan the beam across the sample, and at each transverse location, the reference mirror is translated over a range of  $\Delta z$  to obtain an axial scan (A-scan). The resulting peaks in the axial profile represent reflective surfaces, and sequential A-scans are acquired using a scanned optical spot to generate a two-

dimensional (2-D) cross-sectional images (B-scans). Multiple B-scans can be acquired with scanning in two lateral direction, which generates a stack, or 3-D volume, or OCT images [135, 136].

To overcome the limitation of the A-scan rate of TD-OCT, a novel OCT detection scheme without any moving mirror was proposed. The structure was similar to that of the TD-OCT system, but the detection principle is significantly different. The new OCT system was called Fourier domain OCT (FD-OCT) because the reflection positions of the sample were retrieved not by scanning the reference mirror but by Fourier transform of the interference spectrum of the superimposed reflected light from the two arms. FD-OCT measures all the reflected light in the wavenumber domain, resulting in advantages in imaging speed and signal-to-noise ratio over TD-OCT. The delay echo time is calculated by performing fast Fourier transform (FFT) (Fig. 11b) of the interference spectrum of the light.

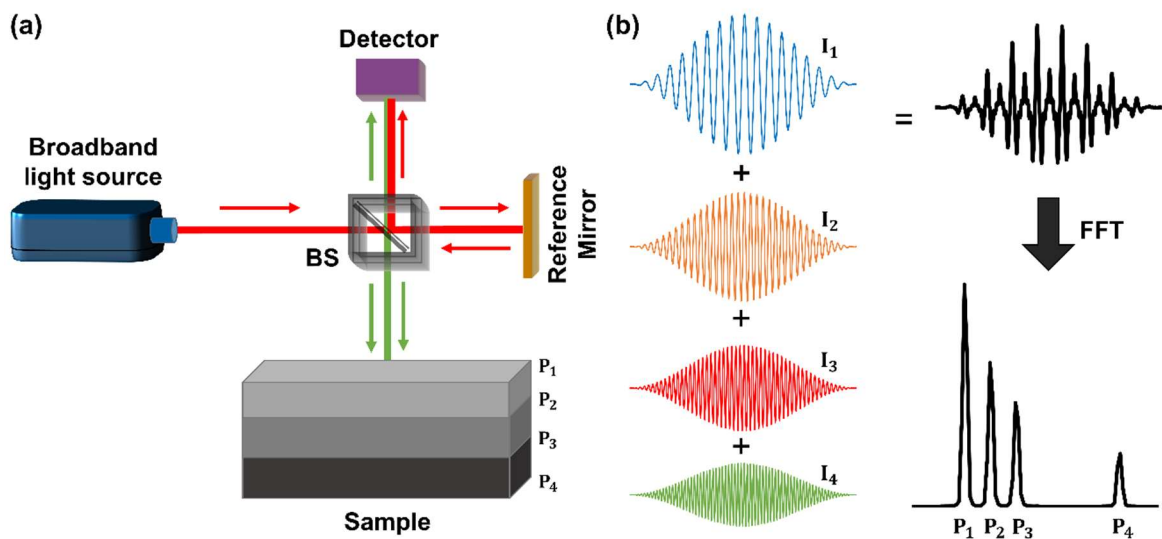


**Figure 11.** (a) A Michelson interferometer with a broadband light source. An integrated interference signal from each interface ( $P_1$ ,  $P_2$ ,  $P_3$  and  $P_4$ ) is detected at the detector. (b) An interferogram showing the positions of the interfaces is retrieved from the real function of the fast Fourier transform (FFT) of the integrated interference signal.

Two established ways of realizing an FD-OCT are spectral domain OCT (SD-OCT) and swept-source OCT (SS-OCT), which differ by the optical sources, detection and acquisition methods of the interference spectrum. SD-OCT employs a broadband light source together with a spectrometer (with a diffractive grating and one-dimensional detector array) for detection [137]. However, FD-OCT is limited by the number of sample points to resolve the high order interference spectrum frequencies and acquisition speed of the camera.

The limitations of SD-OCT are overcome by SS-OCT that uses a frequency tunable laser to rapidly sweep the laser across its frequency range for each sample location, recording the interference at each wavelength individually by a single photodiode [135, 137-139]. Both FD-OCT methods result in data sets that represent the intensity distribution as a function of wavelength, which are further processed to create depth profiles of tissue reflectivity. In SS-OCT, a wavelength sweep period results in frequency modulated interference spectrum according to the optical path differences between the reference arm and the interfaces of the sample [140, 141].

SS-OCT has been the most promising because of several advantages over SD-OCT. Firstly, SS-OCT has higher sensitivity because it adopts a single point photodetector which shows higher sensitivity than the detector unit (pixel) of CCD or CMOS line array used in SD-OCT. Secondly, the difference of the distances from the units of line arrayed CCD to the incident point of diffractive grating inevitably leads to serious field curvature phenomenon and dispersion, which introduces unavoidable crosstalk to the multichannel spectrometer [135, 138, 139, 141-143]. Therefore, it will limit the spectral resolution and the contrast ratio of the retrieved interference fringe, which impact signal drop with depth. The corresponding spectral resolution can be greatly enhanced in SS-OCT because of the narrow instantaneous linewidth of swept source and the high-speed photodetector, which consequently improves the axial imaging range and signal drop. The advancements in the optoelectronics industry have led to the availability of low cost high speed single point photodetectors with >10 GHz bandwidth that are available in all wavelengths of 400-1700 nm. The A-scan rate of SS-OCT depends only on the sweep rate of the swept source, which can be as high as hundreds of megahertz and much higher than the A-scan rate of TD-OCT and SD-OCT.

### 2.2.2 Key parameters of the SS-OCT system

Several parameters play a crucial role in determining the performance of the OCT system. The lateral and axial resolution determine the level of details visualized in OCT image. The sensitivity determines the minimum signal back-scattered in the sample that can be detected. The A-scan rate or imaging speed shows how fast the OCT could capture axial line data. These parameters are critical in the evaluation and comparison of the OCT imaging system. The selection between SS-OCT and SD-OCT is made based on applications with the selection of appropriate wavelength and light source, the choice of scanning speed and density, the use of effective signal processing techniques, and the selection of the appropriate imaging protocol [135, 138, 139, 141-143]. Other factors that may impact OCT performance include the quality and stability of the instrument, as well as the experience and expertise of the operator

For our study, we selected SS-OCT because of its advantage of the long imaging range. In SS-OCT, most of the key parameters are determined by the performance of the swept source. Here we briefly discuss the impact and limitations of the parameters.

#### Wavelength swept-source laser

In SS-OCT, a tunable light source sweeps the wavelength over time. Therefore, in practice the sample is illuminated with the light of different wavelengths during the sweep. Some key technical specifications of wavelength-swept sources include:

- *Output power* - determines signal-to-noise ratio (SNR), but is limited by tissue exposure limits/detector saturation,
- *Tuning curve* - determines linearity of wavelength sweep,
- *Sweep repetition rate* - determines A-scan rate and sampling density,
- *Tuning range (bandwidth)* - determines axial resolution,
- *Instantaneous linewidth* - determines coherence length, or signal roll-off (fringe visibility) with depth, and
- *Relative Intensity Noise (RIN)* - affects SNR and the presence of image artefacts.

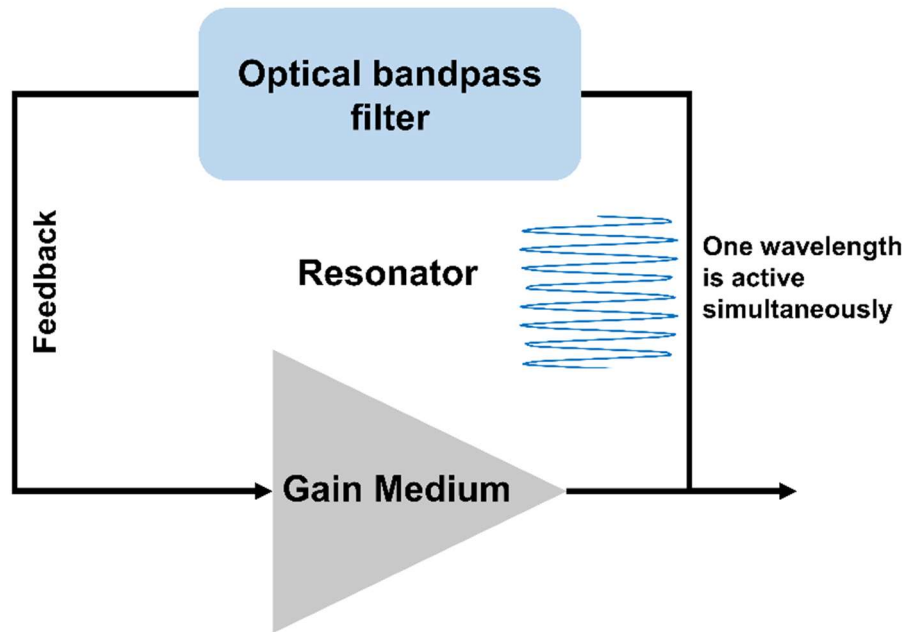


**Figure 12.** Schematic diagram of a conventional wavelength swept laser.

Figure 12 shows a scheme of a wavelength swept laser which consists of a resonator including a gain medium and a fast tunable optical bandpass filter which is dynamically tuned to set the lasing wavelength [144] (centered around 850 nm, 1060 nm, 1300 nm). The sweep range of the wavelength swept laser is determined jointly by the tuning range of the bandpass filter and the gain profile of the gain medium. In operation, normally multiple cavity modes over the gain loss balance threshold will be excited and circulate in the laser cavity.

When the filter wavelength is tuned, the lasing modes which are moved out of the passband will be attenuated soon and new laser modes in the new passband will start to grow. However, the new laser signal is grown from amplified spontaneous emission, which will take hundreds of round trips to reach a stable lasing state.

The wavelength swept-source laser, specifically the one used in this project, incorporates a semiconductor laser and a short cavity MEMS (Micro-Electro-Mechanical System) based Fabry-Perot tunable filter [145]. A semiconductor optical amplifier generates light at a specific frequency within the laser cavity, where it undergoes reflection and amplification. The integrated MEMS Fabry-Perot filter comprises adjustable mirrors that modify their position through MEMS technology.

This alteration changes the resonant frequency of the filter cavity, enabling the transmission of various wavelengths. Precise control of the mirror separation via an actuator facilitates the tunability of this laser. Consequently, a continuous range of emitted wavelengths is achieved, which is highly beneficial for OCT imaging applications.

### **Resolution and depth of field**

In OCT, axial resolution ( $\Delta z$ ) and lateral resolution ( $\Delta x$ ) are decoupled, i.e. the axial resolution depends only on the coherence length of the light source whereas lateral resolution depends on how tightly the beam is focused. The temporal coherence length of a broad-band light source of the OCT system is very short of the order of a few microns ( $>2 \mu\text{m}$ ) because coherence length is inversely proportional to the spectral width ( $\Delta\lambda$ ) of the light source and directly proportional to the source's central wavelength ( $\lambda$ ) squared [135].

$$\Delta z = \frac{2\ln 2}{n\pi} \frac{\lambda^2}{\Delta\lambda}, \quad (2.1)$$

where  $n$  is the refractive index. Like in microscopy, objective lens numerical aperture (NA) defines lateral resolution and the depth of field. Using Gaussian beam optics, the lateral resolution ( $\Delta x$ ) and depth of field ( $b$ ) can be expressed as [135]:

$$\Delta x = \frac{4\lambda}{\pi} \frac{f}{d}, \quad (2.2)$$

$$b = 2z_R = \frac{\pi\Delta x^2}{\lambda}, \quad (2.3)$$

where  $\lambda$  is the central wavelength of the light source,  $f$  is the focal length of the objective lens,  $d$  is the beam diameter incident on the objective lens, and  $z_R$  is the Rayleigh range.

## Imaging range

Depending on the applications of OCT systems,  $b$  can be matched with the imaging range by changing the objective lens from low NA to high NA. Our application uses a low NA objective lens so that  $b > \Delta z$ .

The imaging range ( $Z_{max}$ ) in the Fourier domain OCT system is defined by the sampling wavelength interval ( $\delta\lambda$ ) and is expressed as [130, 135]:

$$Z_{max} = \frac{\lambda_0^2}{4n\delta\lambda}, \quad (2.4)$$

where  $\delta\lambda = \Delta\lambda/N_s$ ,  $N_s$  is the sample range within the full width at half maximum of the laser spectrum. In SS-OCT, the imaging range is dependent on the duty cycle (DC) of the sweep (the fraction of the sweep used for imaging). Therefore, Eq. 2.4 can be rewritten as:

$$Z_{max} = \frac{\lambda_0^2 DC}{4n\delta\lambda}, \quad (2.5)$$

## Sensitivity

OCT is a sensitive imaging technique for weakly scattering objects, including micron-scale biological structures, even when obscured by thick, opaque layers. Assessing an OCT system's sensitivity is crucial to establish its minimum detectable reflectivity and comparing its performance. Sensitivity also highlights the trade-off between image quality and key system parameters such as illumination power and acquisition speed [135, 146]. Sensitivity is directly proportional to the illumination power (limited by saturation threshold of the detectors) and inversely proportional to the acquisition speed.

Sensitivity is defined as the minimum sample reflectivity required to achieve signal-to-noise ratio  $SNR = 1$ .  $SNR$  of the OCT system is calculated using intensity images by [135]:

$$SNR = \left( \frac{I}{\sigma_{bg}} \right)^2, \quad (2.6)$$

which in logarithmic scale (dB) is expressed as

$$SNR (dB) = 20 \log \left( \frac{I}{\sigma_{bg}} \right), \quad (2.7)$$

where  $I$  is the peak image intensity from the sample's OCT image, and  $\sigma_{bg}$  is the standard deviation of the image background intensity (i.e. where a sample is not present). Squaring the signal and noise terms is needed to convert OCT image intensity values, proportional to the amplitude of the interference fringes resulting from the cross-correlation of sample and reference fields, to power values.

### **Imaging speed**

SS-OCT avoids the mechanically moving reference arm in TD-OCT (at kHz level) and overcomes the fundamental speed limitation of spectrometers such as CCD or CMOS in SD-OCT (at a hundred kHz level). SS-OCT has demonstrated the fastest A-scan rate ever reported at tens of megahertz by adopting high-speed swept sources and a balanced photodetector with GHz bandwidth to acquire time-resolved interference signal [140-142, 144, 147, 148]. The A-scan rate of the SS-OCT is solely determined by the sweep rate of the swept source, which has great potential for applications of the volumetric imaging and assessment of ultrafast motions.

### **2.2.3 Characteristics of the swept-source OCT system used for the study**

The OCT system used in the project employed a customized wavelength tunable swept source of 1050 nm, sweep rate 50 kHz, and 110 nm bandwidth (duty cycle 60%; Axsun Technologies Inc., USA). The detection and acquisition subsystem consisted of a dual-balanced photodetector (PDB-480-C, Thorlabs Inc., USA) and a data acquisition (DAQ) card of 0.8 GS/s bandwidth (National Instruments, USA) [132]. The sample is imaged using bi-directional galvo-scanners and is driven using voltage signals generated via a DAQ card (Fig. 13) [14, 114, 131, 133].

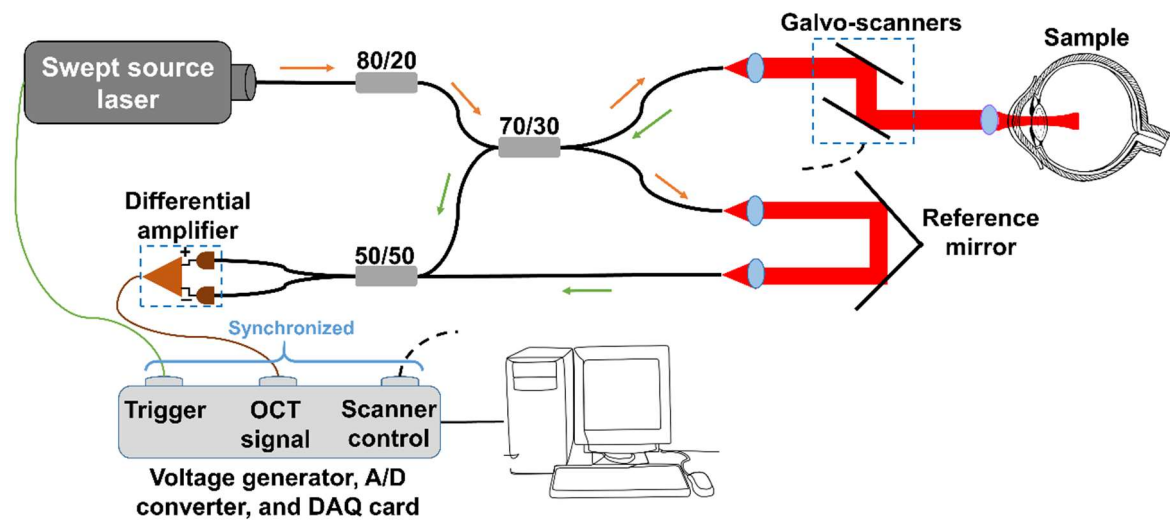


**Figure 13.** Swept-source OCT system schematics.

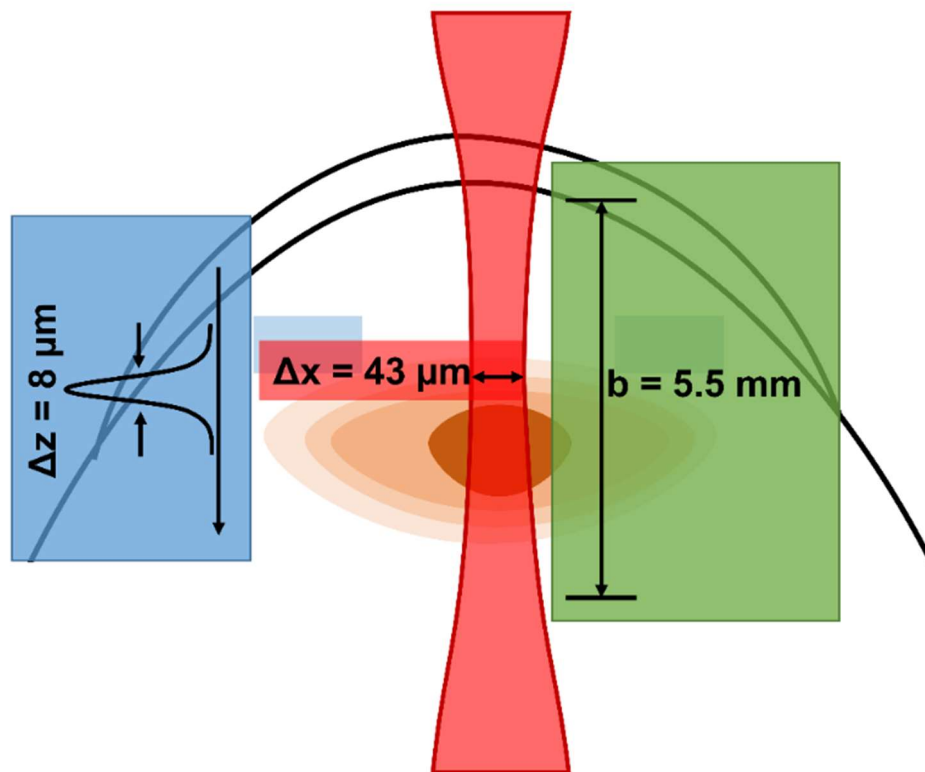


**Figure 14.** Axial resolution ( $\Delta z$ ), lateral resolution ( $\Delta x$ ), and depth of field ( $b$ ).

The OCT imaging was performed with the SS-OCT instrument enabling whole anterior segment visualisation [131, 149]. The imaging depth range of the system was 22.2 mm in air. The obtained sensitivity was 103 dB. The axial resolution, lateral

resolution, and depth of focus were  $8\ \mu\text{m}$ ,  $43\ \mu\text{m}$ , and  $5.55\ \text{mm}$  in air, respectively (Fig. 14). The power incident on the cornea ( $1.9\ \text{mW}$ ) did not exceed American National Standards Institute (ANSI) standards. The field programmable gate array (FPGA) module of the acquisition card enabled the preview mode in real time.

#### 2.2.4 Image acquisition and synchronization

The OCT system incorporates multiple electronic devices; light source, two-dimensional galvo-scanners (for three-dimensional imaging), and data acquisition cards that are synchronised to produce desired OCT images. The laser trigger signal is used to synchronise these devices, where the data acquisition period and galvo-mirror scanning frequency are adjusted according to the wavelength sweep rate of the laser (Fig. 15) [135].

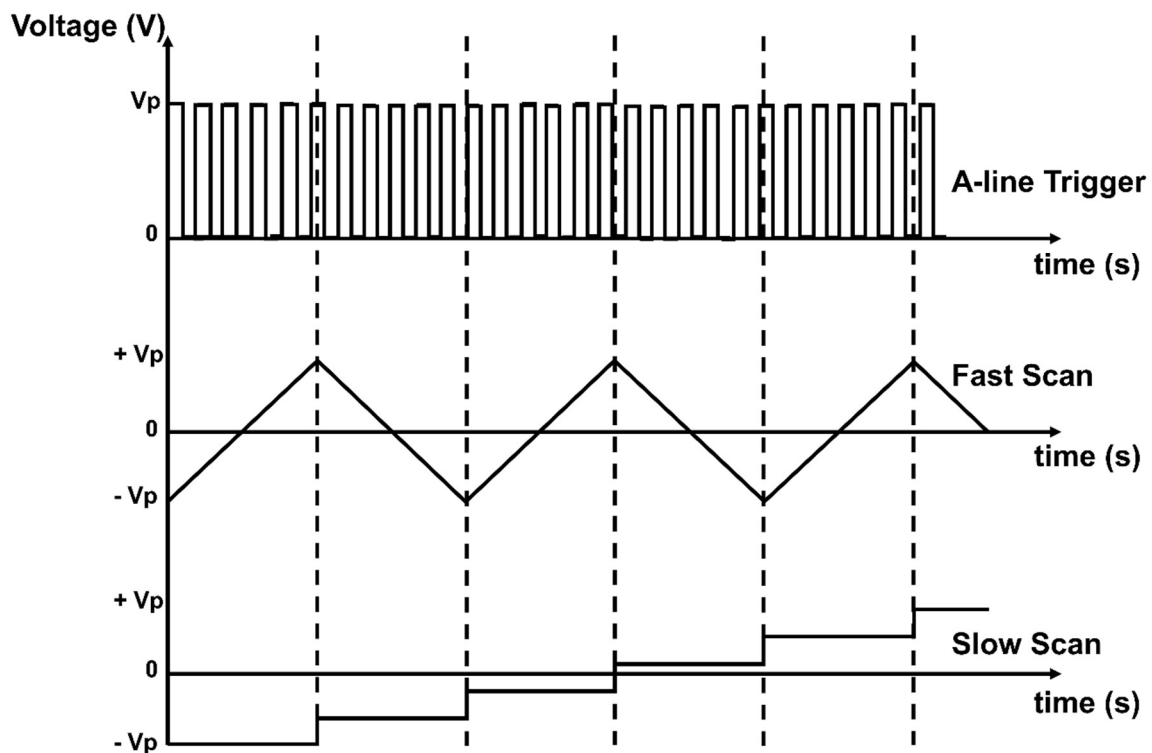


**Figure 15.** Synchronisation of galvo scanners with the data acquisition in three-dimensional raster scan protocol.

## 2.2.5 OCT signal processing

Depending on the method of acquiring the interference signal, the detection system, including electronics as well as digitization and acquisition of the interference signal must avoid degradation of axial OCT resolution. Hence, the trans-impedance amplifier used in the time domain and tunable laser-driven SS-OCT systems, and in particular the electronic bandpass filtering, must be designed properly and adapted to the ultra-broad optical bandwidth. The electronic bandwidth of the bandpass filter must not be too narrow to avoid reduction of the axial resolution, but must also not be too broad to avoid reduction of the sensitivity by introducing noise [130, 135, 142]. Real-time adaptive filtering can help to optimize sensitivity and maintain axial resolution.

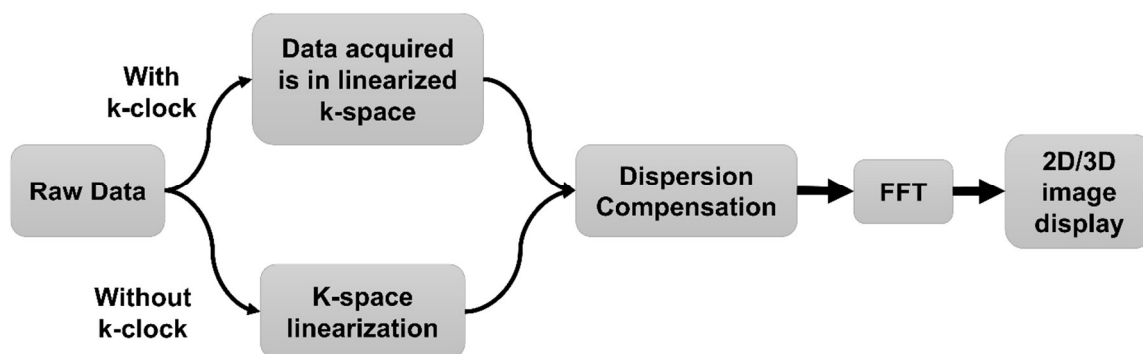


**Figure 16.** Flow chart for swept-source OCT signal processing. Raw data acquired is when non-linearly  $k$ -sampled, then the data undergoes resampling and interpolation process to get linearly  $k$ -sampled, and when data is acquired with  $k$ -clock, then it is directly interpolated in linearized  $k$ -spaced. The numerical dispersion compensation algorithm is used to get the correct point spread function. After taking FFT, complex data is generated that can be used to generate 2D/3D intensity and/or phase images (depending on the application).

The OCT signal must be correctly temporally digitized with at least 5–10 times oversampling with respect to the central wavelength, Doppler shift, as well as scanning speed in order to not degrade the achieved axial resolution. With tunable lasers, the

linearity of the scan has to be adjusted or alternatively, the k-trigger can be used to generate a scan discretely sampled linearly in k-space [135, 139, 142].

The interferometric signal obtained from digitisation is subjected to digital signal processing to produce tomographic images. Figure 16 illustrates the typical steps involved in SS-OCT signal processing. The interference spectrum is initially captured in  $\lambda$ -space, followed by an interpolation to linearised k-space (if k-clock is not used in hardware). However, the axial resolution can deteriorate in the presence of higher-order dispersion caused by backscattering from a heterogeneous medium. To address this, dispersion compensation algorithms (as described later) are applied during post-processing to improve the axial resolution. Finally, a fast Fourier transform is utilized to convert the acquired spectrograph into a tomogram and generate the OCT images. [135, 139, 142, 150-152].

## Raw data

The raw OCT interference signal at a single photo diode can be represented as [136]:

$$i_{\text{det}}(t) = \frac{\eta q}{h\nu} \left( P_r + P_s + 2\sqrt{P_r P_s} \int r(z)\Gamma(z) \cos(2k(t)z + \phi(z)) dz \right), \quad (2.8)$$

where  $\eta$  is the detector sensitivity,  $q$  the quantum of electric charge ( $1.6 \times 10^{-19}$  C),  $h\nu$  the single photon energy,  $P_r$  is half of the optical power reflected from the reference arm at the photodetector, and  $P_s$  is half of the optical power illuminating the sample. Here,  $z$  is the axial coordinate corresponding to the interferometer's optical path difference between the sample and reference arm.  $r(z)$  and  $\phi(z)$  amplitude and phase of the sample arm signal,  $\Gamma(z)$  is the coherence function of the laser output, and  $k(t)$  is wavenumber varying dynamically monotonously at the time at which laser output wavelength is tuned.

The dual-balanced detection of the interference signal comprises noise signals that originate from various sources; quantization noise and excess electrical noise generated in the digital acquisition (DAQ) board, thermal noise of the dual-balanced receiver, and relative intensity noise (RIN) of the swept-source. The common-mode

rejection ratio (CMRR) describes the ability of the balanced detector to reject common-mode signals (signals that appear in-phase and simultaneously at both inputs). Thus, dual-balanced detection in swept-source OCT eliminates any DC signal ( $P_r + P_s$ ) from the interferometer and amplifies the AC signal. Hence, the RIN is suppressed due to balanced detection. The noise signal in the OCT system is responsible for degrading SNR and resolution. In SS-OCT, the interference signal integrated with noise signals from all sources can be expressed as [135]:

$$i_n(t) = \left( \frac{i_{qn}}{G^2} + \frac{i_{ex}}{G^2} + i_{th} + \sqrt{2 \frac{\eta}{h\nu}} q \sum (P_r + P_s) + \frac{\eta q}{h\nu} \sqrt{RIN} \left\{ \sum \sqrt{\zeta(P_r^2 + P_s^2)} + \sum \sqrt{2P_r P_s} \right\} \right) BW, \quad (2.9)$$

where BW is detection bandwidth. The first two terms are introduced as the quantization noise and excess electrical noise generated in the digital acquisition (DAQ) board. G denotes the total gain of the receiver. The third term is the thermal noise of the dual-balanced receiver. The fourth term represents the total shot noise which is the sum of the shot noise from the individual photodiodes. The fifth term expresses the RIN of the swept-source with  $\zeta$  denoting the common-mode rejection efficiency of the balanced receiver. In addition to RIN reduction (compared to spectral domain OCT), the balanced detection provides multiple benefits; it suppresses self-interference noise [139] originating from multiple reflections within the sample and optical components; it also improves the dynamic range and reduces fixed-pattern noise by greatly reducing the strong background signal from the reference light.

### **K-space linearisation**

The wavelength tuning in the swept laser sources cause the wavenumber to be swept nonlinearly and to vary within subsequent sweeps which are referred to as intra and inter-sweep variability, respectively. Fourier transformation on the non-linearly sampled OCT data will lead to the deterioration of the axial resolution and sensitivity. Therefore, the acquired OCT signal must be resampled into the uniform k-space intervals prior to Fourier transformation. Moreover, a real-time calibration is required to correct the inter-sweep variability. One way is resampling the raw OCT fringes using

linearized phase difference at the two peak positions (close to autocorrelation peak and middle of the imaging range) of a mirror in sample arm that was manually moved along the OCT imaging range and then interpolating the OCT fringes to phase difference sample points of size  $N_s$  to get linearized k-spaced fringes. The second way, in-built auxiliary interferometer can be used for calibration signal (k-clock) generation to linearize k-space (Fig. 16).

### **Dispersion compensation**

OCT is an optical imaging modality that involves various optical elements; lenses, and optical fibres. The OCT light passes through different media with different refractive indices and the image is created upon recording interference signal from non-homogenous biological tissues that have non-linear refractive index gradients. The light passing through different optical media and bio-samples suffer from high-order dispersion. Dispersion is a phenomenon by which the speed of the light in a medium depends on wavelength [31]. Due to dispersion, if the total group refractive indices of all media in the sample and reference arms are mismatched, the axial resolution will be degraded [135, 136, 142, 153].

Temporal and spatial frequencies are interrelated in SS-OCT. By Fourier transforming the acquired temporal signal (interference fringes), the OCT system can obtain the spatial frequency content of the sample. Each temporal frequency has a corresponding spatial frequency in the OCT images. Because of dispersion (chromatic dispersion), the spatial and temporal frequencies are not necessarily proportional to each other, as they are in free space. The relationship between temporal and spatial frequency is given by the medium dispersion relation, [135, 142] known as propagation constant and can be specified in many ways; by refractive index as a function of wavelength or the spatial frequency wavenumber in the medium as a function of temporal frequency. Therefore, the mathematical representation of propagation constant  $\beta$  in a medium can be given as [142, 153, 154]:

$$\beta(k) = n(k)k, \quad (2.10)$$

where  $n(\lambda)$  is the refractive index dependent on wavelength  $\lambda$  propagating through the medium and  $n(k)$  is the refractive index dependent on the wavenumber  $k$  (dispersion relation). For any medium, the propagation constant can be expanded as Taylor series near central wavelength  $\lambda_0$  or wavenumber  $k_0$ . The expanded wavenumber-dependent propagation constant is given as:

$$\beta(k) = \sum_{m=0}^{\infty} \beta_m (k - k_0)^m, \quad (2.11)$$

$$\beta_m = \frac{1}{m!} \frac{d^m \beta}{dk^m}, \quad (2.12)$$

$$m = 0, 1, 2, \dots$$

where the first coefficient  $\beta_0$  describes the propagation constant in the medium at  $k_0$ , the second coefficient  $\beta_1$  represents the phase velocity of light, and the third coefficient  $\beta_2$  of the Taylor series expansion,  $\frac{1}{2} \left( k_0 \frac{d^2 n}{dk^2} + \frac{dn}{dk} \right)$ , is described as group velocity dispersion and second order dispersion. OCT images that exhibit distortions, blurs, and a degraded point spread function can be attributed to second or higher-order dispersions, which are described by terms in the Taylor series expansion beyond the third term (as represented by Eq. 2.11) [142, 155].

The OCT signal can be corrected for dispersion mismatch either by inserting a dispersion compensation material into the reference arm to balance the dispersion of the sample signal or by employing dispersion compensation algorithms. Various dispersion compensation algorithms have been developed that estimate dispersion compensation phase (DCP) either numerically or from experimental data [151, 152, 156, 157]. The numerical method is preferred over hardware modifications because; 1) compensation of higher than second-order dispersion requires the same material or elaborate combinations for balancing, and 2) it is challenging to dynamically compensate depth-dependent sample dispersion for inhomogeneous medium [135].

The dispersion can be efficiently corrected by eliminating the dispersion-induced phase contribution from the spectral phase of the OCT signal. The estimated coefficients are applied to the polynomial equation and the equation is used to estimate DCP by:

$$\varphi_{DC}(k) = \beta_2 (k - k_0)^2 + \beta_3 (k - k_0)^3, \quad (2.13)$$

where,  $\beta_2$ , and  $\beta_3$  are coefficients of expanded wavenumber dependent propagation constant that represents 2<sup>nd</sup> and 3<sup>rd</sup> order dispersion. Next step, multiply the complex conjugate of the DCP with the recorded OCT signal in the Fourier domain to get dispersion compensated OCT signal expressed as:

$$I_{DC}(k) = I(k) \times \exp(-i\varphi_{DC}(k)), \quad (2.14)$$

where,  $I(k)$  is the recorded OCT signal. Ideally, if DCP can be measured for the imaging system, it would help in eliminating effects on dispersion mismatch and enhance the OCT imaging quality [142].

### Fourier transform and image construction

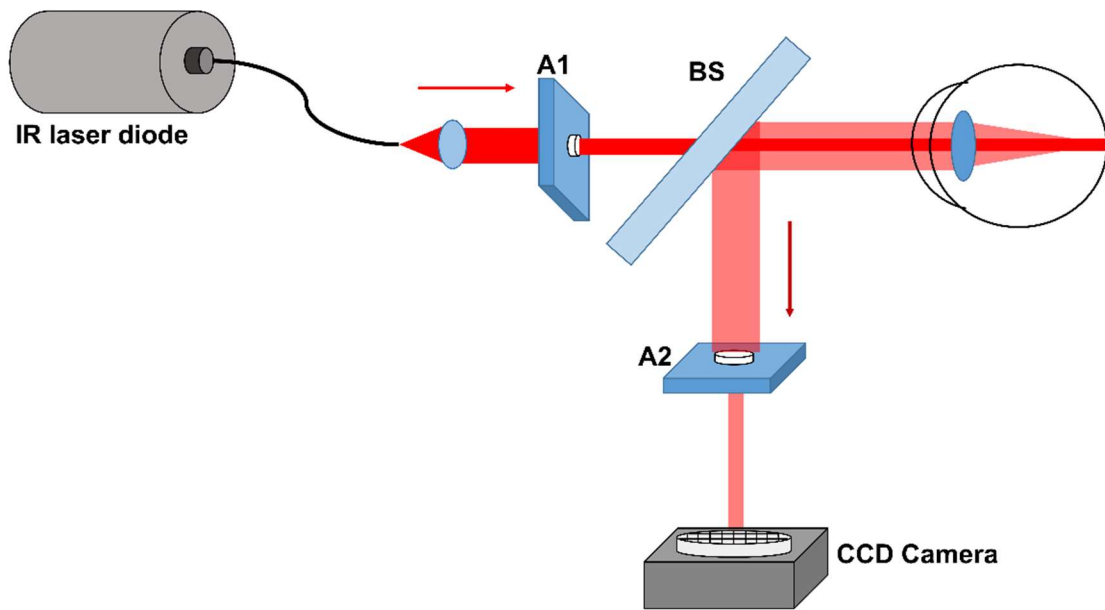
SSOCT system constructs images by performing inverse fast Fourier transform of the spectral interferogram that are linearly sampled in frequency space. Logarithmic non-linearity is used to compress the processed data to fit the dynamic range for display and for brightness correction.

## 2.3 Double-pass system for the analysis of the optical quality of the eye

The **ideal** optical system maps a point source in the object space into a point of the image space. However, some fraction of light in the **real** optical system can be misdirected, which is often referred to as straylight. Straylight can be visualised by the measurement of a point spread function (PSF) in the image plane of the system with the aid of array detector. Straylight in the optical systems appears due to scattering at the edges, reflections at optical surfaces, imperfections of optical elements, dust etc.

The straylight, caused by intraocular scattering, affects the optical quality of the eye and is perceived as glare in the vision [15, 98]. However, it is impossible to measure the PSF of the optical system of the eye *in-vivo* since the image plane is occupied by the retina. Therefore, one needs to use double-pass configuration to measure the retinal PSF. In a double-pass configuration, the light enters the eye and reflects off the retina

before passing through the eye's optical system again. This measurement concept has been implemented in an optical quality analysis system (OQAS). The OQAS is a non-invasive system that employs an infrared laser and uses a double-pass configuration to evaluate the optical quality of an individual's eyes [116-118]. This technology offers a more comprehensive and accurate analysis of an individual's visual function, enabling more precise diagnosis and treatment.



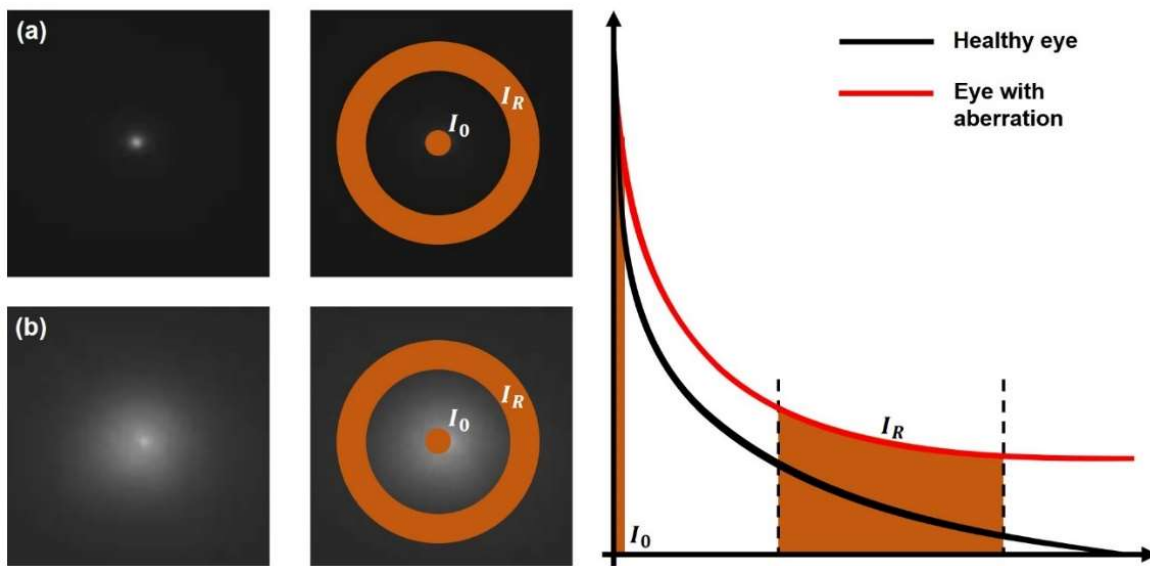
**Figure 17.** Double-pass OQAS scheme (adapted from [117]).

Figure 17 shows schematics of OQAS, a collimated beam is passed through an aperture (A1), mimicking a point light source. The reflected point source image from the retina is passed from the second aperture (A2), and then imaged on a CCD camera (BS is a beam splitter). Therefore, the array detector acquires the image of the point source (PSF) of the ocular system. The magnitude of straylight is quantified as objective scattering index (OSI). The OSI is defined by the following formula [116]:

$$OSI = \frac{I_R}{I_0}, \quad (2.15)$$

where  $I_R$  and  $I_0$  represent the integration (summation) of intensities at specific regions of interests (ROI) image pixels (Fig. 18).

In one of the proposed methods [116] for measuring OSI, the central ROI from the OQAS image was selected at 1 minute of arc radius, while the ROI for the periphery was a ring with 12 and 18-minute inner and outer arc radii, respectively. A multiplying factor of 0.1 limits the accessible values of OSI from 0 to a maximum of 25. OSI for normal eyes would range around 1, while values over 5 represent highly scattered systems.



**Figure 18.** Selection of ROI and computing intensity radial average using double pass image for **(a)** the healthy eye, and **(b)** the eye with intraocular scattering [116].

The OQAS integrated with the Badal optometer can evaluate various visual conditions, such as myopia, hyperopia, and astigmatism, and can also assess the impact of different treatments, such as contact lenses or intraocular lenses, on visual function [117, 118, 158]. Moreover, the OQAS is not limited to diagnostic purposes and can also be used to investigate the effects of ageing or disease on optical quality, providing valuable insights into the mechanisms of visual impairment [30, 98, 117, 118].

## **2.4 Adaptive optics visual simulator**

A visual simulator is a device that reproduces the visual experience of an individual, allowing ophthalmologists to test and evaluate visual function. Adaptive optics visual simulators (VAO, Voptica, Spain) takes this concept a step further by incorporating adaptive optics technology to correct for the optical aberrations of an individual's eyes, providing a more realistic and personalised simulation [15, 30, 101, 159].

The traditional method of testing visual function involves using a chart with various symbols or letters of decreasing sizes. However, this method does not take into account the individual's unique optical aberrations, leading to inaccurate results. VAO, on the other hand, can measure and correct for these aberrations, providing a more accurate and precise assessment of an individual's visual function.

The principal components of VAO system are a wavefront sensor and a deformable mirror (for dynamically correcting the optical wavefront aberrations) (Fig. 19) [98, 119, 160]. This adaptive correction allows for the precise manipulation of the optical system to provide a more accurate and realistic simulation of the eye's optics. The VAO system is used to measure subjective refraction, visual acuity (VA), and contrast sensitivity of the eye [50, 58, 98].

### **2.4.1 Subjective refraction errors**

One of the major benefits of VAO is that they can simulate and measure various refraction errors such as spherical, and cylindrical aberrations, by adjusting the deformable mirror to mimic the aberrations or aberration-corrections. The subject provides feedback on the perceived clarity and sharpness of the stimuli, which guides the refinement of the optical correction. This iterative process allows for the determination of the optimal optical prescription for the subject, minimizing refractive errors [98, 159, 160].

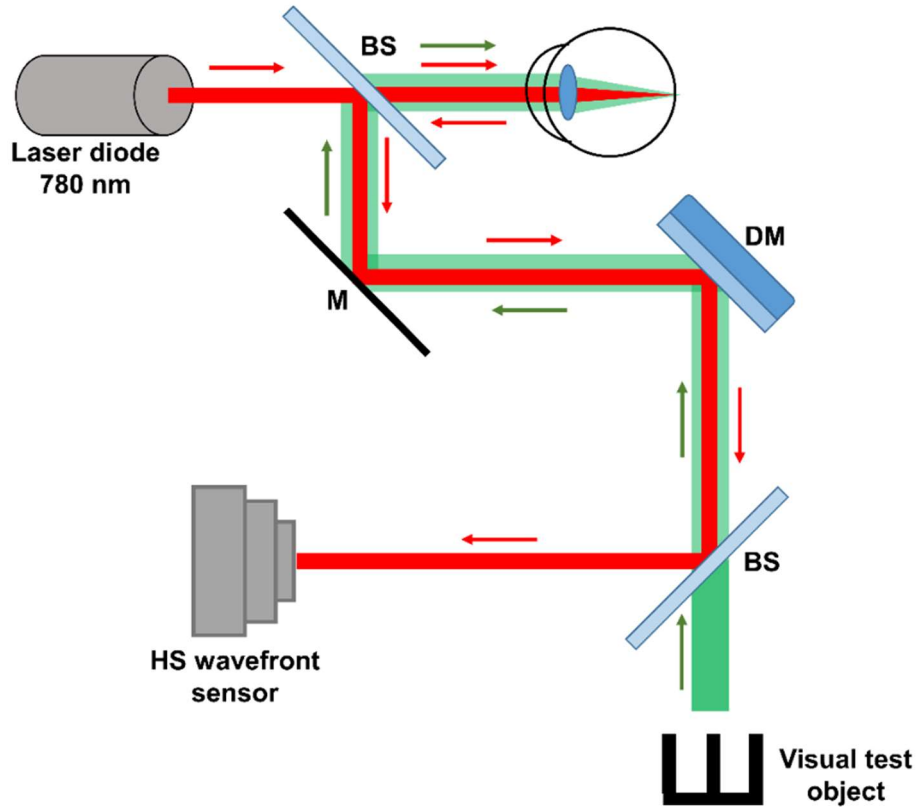


**Figure 19.** Schematic diagram of Adaptive optics visual simulator (adapted from [116]).

## 2.4.2 Visual acuity

The eye's optical and vision quality is assessed using the VAO system to measure visual acuity. Adaptive optics is used to observe the impact on visual acuity when the eye is stimulated with measured and simulated aberrations. The retinal image quality is analysed by convolving the image (aberrated) with the PSF of the eye for specific pupil size, viewing angle and wavelength. The visual acuity is measured with standard ETDRS (Early Treatment of Diabetic Retinopathy Study) test charts and expressed in the logarithm of the minimal angle of resolution (logMAR) as [98]:

$$VA (\log\text{MAR}) = -0.02 \times (\text{no. of letters read after last line}) + \log\text{MAR score of last line}, \quad (2.16)$$

where the minimal angle of resolution (MAR) is  $1/5^{\text{th}}$  of the angular subtense of the letter.

### 2.4.3 Contrast sensitivity function

The contrast sensitivity function (CSF) describes the visual system's ability to detect and differentiate contrast at different spatial frequencies. It shows how the inverse of the contrast threshold of a grating stimulus relates to its spatial frequency [116]. The integral of the logarithmic CSF curve gives a quantitative assessment of overall visual performance across various spatial frequencies, representing the combined contrast sensitivity throughout the entire range of frequencies tested.

Contrast sensitivity test is performed to assess visual function. Using VAO, the subject sits in front of the system in a dimly lit room to minimize the impact of pupil constriction. The VAO system's wavefront correction settings are adjusted to correct the subject's refractive error. The VAO generates sinusoidal gratings as visual stimuli, consisting of alternating light and dark bars with specific spatial frequencies and contrasts. These gratings are presented at different spatial frequencies, typically spanning from low to high frequencies. In this study, the spatial frequencies tested were 2, 4, 6, 8, 10, 15, 20, 25, 30, 35, 40, 45, and 50 cycles per degree, representing the number of light-dark cycles within one degree of visual angle. The gratings are displayed at varying contrast levels, ranging from low to high contrast, where contrast refers to the normalized difference in luminance between the light and dark bars of the grating (Fig. 20).

The subject's task is to identify the gratings by indicating the specific grating orientation (left for  $45^\circ$  or right for  $315^\circ$ ). The VAO system records the contrast threshold values for each spatial frequency and contrast level tested, which represents the minimum contrast required for the subject to detect or differentiate the grating. The stimuli are presented in a randomized order to minimize any bias or learning effects.

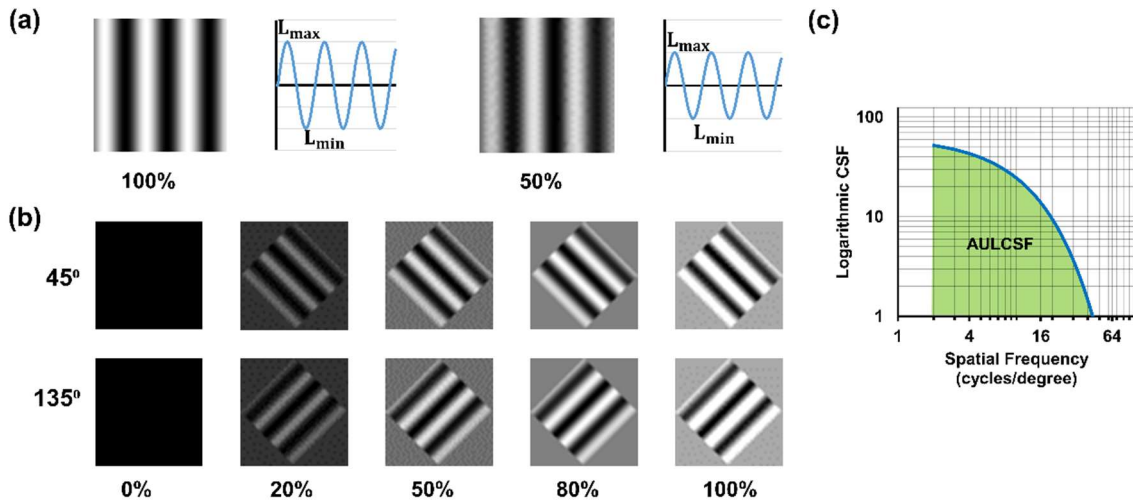


**Figure 20.** (a) Sinusoidal gratings with 100% and 50% contrast levels with a spatial frequency of 3 cycles/degree. (b) The sinusoidal gratings with orientations, 45° (left) and 135° (right), with different contrast levels, were presented to the subject in random order. (c) The area under logarithmic contrast sensitivity function (AULCSF) for a 17 year old subject.

The contrast sensitivity for each spatial frequency is determined by calculating the inverse of the contrast threshold, indicating the ability to perceive the gratings. The acquired data are plotted in a format of the contrast sensitivity function. Later on, the area under the log of CSF is measured (Fig. 20) to quantify the subject's visual performance. A larger value indicates better overall contrast sensitivity, implying a better spatial performance. Conversely, a smaller area suggests reduced contrast sensitivity and the possibility of visual impairments.

## Chapter 3

# Age-related changes in the shape and transparency of the human crystalline lens

### 3.1 Motivation and aim of the study

The crystalline lens is a critical component of the eye that plays a significant role in focusing light onto the retina. Therefore, the factors that determine the performance of the crystalline lens in the optical system of the eye include the geometry and transparency of the lenticular tissue. The lens must remain clear to allow light to pass through it and reach the retina. This is achieved by the highly ordered arrangement of its uniform, irreversibly differentiated fibre cells [161-163]. Any changes in the transparency of the lens can lead to visual impairments such as blurry vision or halos around lights. The lens morphology is equally important, as it must maintain its biconvex shape to refract the light. The complex formation of the crystalline lens and ever-growing fibre cells results in continuous changes in its morphology [7, 9, 10]. Changes in the lens morphology can lead to visual impairments such as myopia or hyperopia.

The crystalline lens transparency and morphology are influenced by a variety of factors, including genetics, age, and external environmental conditions such as exposure to UV radiation. All these factors were discussed briefly in section 1.2. In particular, the natural ageing processes are associated with lens growth and loss of transparency.

Recent studies show that various imaging modalities enable the examination of the lens structure. Table 1 presents *in-vivo* measurements for analysis of the age-related changes (thickness) in the crystalline lens that were performed using a Scheimpflug camera, ultrasound, magnetic resonance imaging, and OCT. These measurements led to the expected conclusion of thickening of the crystalline lens and a gradual decrement in the radii of the curvature of the lens surfaces with age. Unlike geometrical parameters, previous studies with different technologies revealed linear or non-linear

relationships of lenticular transparency with age (Table 2). However, Scheimpflug imaging, ultrasound, and MRI lacks sensitivity and has poor resolution, especially compared to imaging modality like OCT.

**Table 1.** Age-related changes in the lens thickness in *in-vivo* studies.

<b>Imaging modality</b>	<b>Age range (years)</b>	<b>Average thickness (mm)</b>	<b>Growth rate (mm/year)</b>	<b>Reference</b>
Ultrasound	18-70	Lens = 4.03 mm	Lens = 0.013	[57]
Scheimpflug slit lamp	18-70	Lens = 3.98 mm	Lens = 0.013	[57]
Scheimpflug slit lamp	18-70	Lens = 3.81 mm Cortex = 1.88 mm Nucleus = 1.97 mm	Lens = 0.014 Cortex = 0.017 Nucleus = - 0.003	[124]
MRI	22-83	Lens = 3.86 mm	Lens = 0.024	[120]
Scheimpflug camera	16-65	Lens = 3.93 mm Cortex = 1.65 mm Nucleus = 2.23 mm	Lens = 0.024 Cortex = 0.02 Nucleus = 0.003	[125, 164]
MRI	18-59	Lens = 4.00 mm	Lens = 0.018	[121]
Visante OCT	35.9-49.8	Lens = 4.05 mm	Lens = 0.021	[165]
Extended depth OCT	21-71	Lens = 4.09 mm	Lens = 0.029	[166]

**Table 2.** Age-related changes in lens transparency.

<b>Imaging modality</b>	<b>Age range (years)</b>	<b>Optical density vs age curve</b>	<b>Comment</b>	<b>Ref.</b>
Slit-lamp Scheimpflug photography	20-80	Linear fit	Optical densities were computed for lens layers (capsule, cortex, and nucleus) based on the densitograms.	[127]
Slit-lamp Scheimpflug photography	18-70	Exponential fit and bilinear fit	Optical densities were normalized based on the lens densitograms. The paper includes plots for only the C3 layer and the whole lens.	[124]
Scheimpflug camera	25-80	Linear fit	Both peak and average optical densities showed a high correlation and increased with age. Plots showed only the lens and nucleus. Stray light passed through the eye was evaluated. Scattering increased with age exponentially. Plots showed only lens	[5]
C-Quant	20-85	Exponential fit	Optical densities computed were normalized to generate an optical density index that increased exponentially with age.	[167]
Purkinje image-based system	22-67	Exponential fit	8 regression models were used, but plots show two types of fits. Optical density was normalized and all regression models agreed with optical density increases with age	[129]
SS-OCT	3-69	Linear and bilinear fit		[168]

In this chapter, we investigated the age-related changes in the morphometry and transparency (optical density) of the crystalline lens *in-vivo* using volumetric SS-OCT. We also associated the parameters describing the shape and optical density of the lenses with the optical quality of the eye and with visual function.

## 3.2 Data acquisition

This cross-sectional study was accomplished by recruiting 50 participants (with ages ranging from 9 years to 78 years) to the Laboratory of Optics at the University of Murcia. The study adhered to the tenets of the Declaration of Helsinki. The volunteers were informed about the nature of the study, and written consent was obtained from each participant and in the case of children parental consent was also obtained. The Institutional Review Boards at Nicolaus Copernicus University and the University of Murcia approved the study. Standard ophthalmic examination was conducted for all individuals, and participants with previous ocular surgery were excluded from the study. All eyes were imaged in an unaccommodated state and with no pupil dilation. 3-D volumetric data (300 A-scans  $\times$  300 B-scans) were acquired by raster scanning of the central area of  $8 \times 8 \text{ mm}^2$  of the eye. We rejected data from one volunteer in this study because of the low quality of the acquired OCT images (noise beyond correction and motion artefacts). One randomly selected eye from each volunteer was taken for statistical analysis (49 eyes in total) to avoid correlations between fellow eyes.

A double-pass technique-based optical quality analysis system (OQAS, HD Analyser II, Visiometrics SL, Terrassa, Spain) was used to evaluate the optical quality of the eye objectively and to determine OSI (compare section 2.3). The visual function was assessed with an adaptive optics visual simulator (VAO; Voptica SL, Murcia, Spain). In this study, VAO measured VA of the eye and performed a contrast sensitivity test so that the area under the log contrast sensitivity function (AULCSF) could be determined (compare section 2.4).

### **3.3 Data post-processing and statistical analysis**

#### **3.3.1 Motion artefacts correction**

Volumetric data sets from *in-vivo* imaging often suffer from motion artefacts, which is a consequence of involuntary eye mobility during the scanning procedure. In the post-processing, motion artefacts in 3-D data sets were corrected for motion in two directions, transverse and axial. First, the *en-face* projection image was generated from volumetric data and binarised to determine the transverse motion artefacts. Therefore, for each B-scan, the edges of the pupil mask could be easily obtained from a binarised *en-face* image and enabled to find a proper shift of each B-scan with respect to the centre of the volume. The procedure of motion artefact correction allowed us to obtain a circular pupil shape. Later, using two central cross-sectional images taken along slow and fast scan directions from the volume and blurred with a Gaussian window. The anterior interface of the lens was segmented in those images using a Sobel filter, and the ellipsoid surface was fitted. The difference between the fit and segmented anterior lens interface was used to correct B-scans for the axial motion of the eye.

#### **3.3.2 Refraction correction method with ray tracing**

A sample having an optically non-homogeneous medium can also suffer from other distortions due to light propagation inside the sample. First, the OCT image maps optical distances. Accordingly, one has to take into account the refractive index of the sample to be able to measure geometrical distances. Secondly, the refraction of the beam can change the apparent dimensions of the sample and the apparent locations of scatterers in the image as the beam does not need to propagate along the z-direction in the object with curved refractive surfaces like the anterior segment of the eye. It is then desirable to find the true spatial locations of scatterers inside the medium with knowledge of the refractive indices of the layers that comprise the medium. The refraction correction method can correct the distortions caused by the refractive index and light refraction [16, 142].

Optically, the eye consists of layers of optical elements and media characterized by different refraction indices. A light refraction correction algorithm using a ray-

tracing approach was applied to dewarp the motion-free OCT images. It required segmentation of the corneal and lenticular interfaces. In particular, lens segmentation of OCT images was achieved by fitting the 2nd-order polynomial at the lens capsule (anterior and posterior) and both cortex-nucleus interfaces. Therefore, a double-shell model was assumed to simplify the GRIN lens in a ray-tracing refraction correction algorithm. Each segmented interface from the cornea to the vitreous had a refractive index estimated using the Cauchy equation:

$$n(\lambda) = n_0 + 0.0512 - 0.1455\lambda + 0.0961\lambda^2, \quad (3.1)$$

where  $n(\lambda)$  is the refractive index of the medium at a wavelength (in  $\mu\text{m}$ )  $\lambda$ ,  $n_0$  is the refractive index of the medium at 555 nm [16]. The following refractive indexes were taken to calculate light propagation through the air – cornea – aqueous humour – the anterior cortex – the nucleus – the posterior cortex – vitreous humour: 1, 1.3665, 1.3266, 1.3749, 1.3947, 1.3749, and 1.3270. Figure 21 demonstrates how the refraction correction modifies the raw OCT image of the crystalline lens.

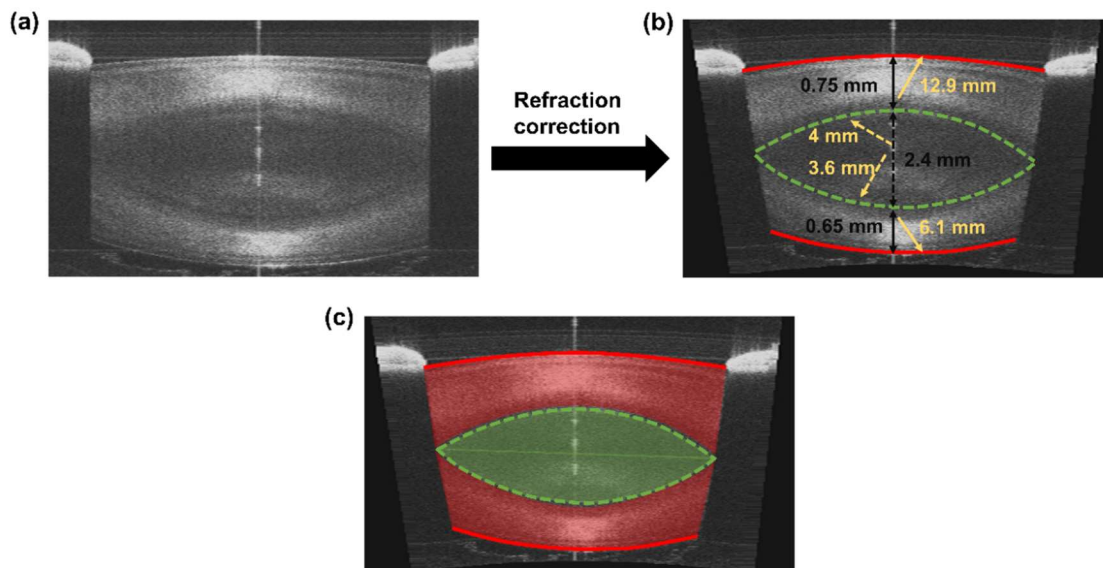


**Figure 21.** (a) Original OCT B-scan of the crystalline lens of a 49-yo subject. (b) Refraction correction of the central B-scan. The surfaces of the anterior and posterior of the lens (solid yellow) and the nucleus (dashed yellow) were used to measure the radii of curvature (yellow arrows), and the central thickness (black double-side arrows). (c) Region of interest to measure the optical density of the lens, cortex, and nucleus.

### 3.3.3 OCT-based morphometry and densitometry of the crystalline lens

The OCT images corrected for light refraction illustrated the true geometry of the measured lens and allowed us to determine the following morphological features of the crystalline lens:

- central lens thickness,
- central thickness of the nucleus and the cortex,
- anterior radius of curvature of the lens,
- posterior radius of curvature of the lens,
- anterior and posterior radii of curvature of the nucleus (Fig. 21b).

It has to be noted that the radii of curvature were determined within the 3.5 mm-diameter region, which is the smallest pupil diameter in our group.

Densitometry of the entire lens and its components was performed by calculating the optical density, which is defined here as the averaged back-scatter light intensity of the corresponding region (lens, nucleus or cortex, as shown in Fig. 21c). Accordingly, the signal in the OCT image was transformed from a logarithmic scale to a linear scale. Then, the signal was averaged within the region as stated by definition.

### 3.3.4 Statistical analysis. Simple linear regression model

In this part of the study, we used simple linear regression (SLR) model to perform a statistical analysis of the results. In the SLR model, two variables in a dataset are compared with each other, and a degree of correlation between them is measured against linear fit. The SLR models are commonly used to analyse and predict one variable's behaviour over another. For example, if we postulate a linear relationship between a variable  $Y$  as an outcome and let  $x$  be the explanatory variable, the SLR model would be [169]:

$$E(Y|x) = \alpha_0 + \alpha_1 x, \quad (3.2)$$

where,  $E(Y|x)$  the expected value of  $Y$  at a given  $x$ ,  $\alpha_0$  is the intercept at  $x = 0$ ,  $\alpha_1$  is the slope (often referred to as the rate  $Y$  values change per unit of  $x$  values). The structural model says that for each value of  $x$ , the population mean of  $Y$  (over all of the

subjects with that particular value “x” for their explanatory variable) can be calculated using the simple linear expression in Eq. 3.2.

Statistical analysis was done using Microsoft Office Professional plus Excel 2013 (Microsoft Corp., Redmont, WA, USA). Spearman’s rank correlation was performed to investigate age-related changes in the lenticular morphology (i.e. thickness and radius of curvature) and the lens transparency. The statistical significance of Spearman’s correlation coefficient  $R_s$  was tested at the significance level  $\alpha = 0.05$ . The simplified SLR model was used to show the linear relation of the measured features with ageing. Correlation coefficients were also generated to observe associations between parameters extracted from OCT, OQAS and VAO, and to investigate the impact of intraocular scattering on vision.

## **3.4 Results**

### **3.4.1 Average parameters in the study group**

Table 3 shows the mean values and standard deviations of the measured morphological features from the refraction-corrected OCT images as well as from VAO and OQAS devices. The average age of subjects was 40 years, with an average lens thickness of 4.54 mm. The averaged radii of curvature of the anterior and posterior lens capsule are 10.19 mm and 5.91 mm, respectively, for the unaccommodated non-dilated eyes.

**Table 3.** Mean and standard deviations of the measured parameters from the 49 eyes.

<b>Variables</b>	<b>Unit</b>	<b>N</b>	<b>Mean (SD)</b>
<b>Age</b>	<b>years</b>	<b>49</b>	39.24 ± 18.80
<b>Subjective refraction</b>	<b>D</b>	<b>49</b>	
Sphere			(-1.0) ± 2.2
Cylinder			(-0.6) ± 0.6
<b>Pupil diameter</b>	<b>mm</b>	<b>49</b>	5.8 ± 1.4
<b>Thickness</b>	<b>mm</b>	<b>49</b>	
Lens			4.54 ± 0.5
Cortex			1.99 ± 0.47
Nucleus			2.39 ± 0.27
<b>Radius of curvature</b>	<b>mm</b>	<b>49</b>	
Anterior lens capsule			10.19 ± 1.63
Anterior nucleus			4.06 ± 0.37
Posterior nucleus			3.67 ± 0.33
Posterior lens capsule			5.91 ± 0.40
<b>Optical density</b>	<b>a.u.</b>	<b>49</b>	
Lens			(25.8 ± 8.5) × 10 <sup>3</sup>
Cortex			(35.0 ± 6.5) × 10 <sup>3</sup>
Nucleus			(14.8 ± 2.9) × 10 <sup>3</sup>
<b>Objective Scatter Index</b>	<b>-</b>	<b>49</b>	0.75 ± 0.55
<b>Visual function</b>		<b>49</b>	
AULCSF	-		2.25 ± 0.20
VA	LogMAR		(-0.01) ± 0.06

### 3.4.2 Age-related changes in the morphometry and optical density of the lens and its components

Morphological and densitometric parameters of the crystalline lens derived from OCT data, OSI and parameters of visual function were also correlated with age. The results are summarised in Table 4, and selected plots are illustrated in Fig. 22. As age increased, the thickness of the lens and identified lens layers increased with high and moderate correlations ( $R_s = 0.34, 0.64,$  and  $0.86$  for the nucleus, cortex, and the whole lens, respectively; Fig. 22a). Whereas overall lens thickness grows at the rate of  $0.023$  mm/year, the cortex thickens at  $0.017$  mm/year and the nucleus only at  $0.006$  mm/year (Table 4).

**Table 4.** Correlation of measured parameters with age.

<b>Dependent Variables</b>	<b>R<sub>s</sub></b>	<b>P-value</b>	<b>Rate of change (per year)</b>
<b>Thickness (mm)</b>			
Lens	0.86*	<0.001	0.023
Cortex	0.64*	<0.001	0.017
Nucleus	0.34*	0.016	0.006
<b>Radius of curvature (mm)</b>			
Anterior lens capsule	-0.70*	<0.001	-0.053
Anterior nucleus	-0.67*	<0.01	-0.013
Posterior nucleus	-0.30*	0.025	-0.006
Posterior lens capsule	<b>0.17</b>	<b>0.304</b>	<b>0.003</b>
<b>Optical density (a.u.)</b>			
Lens	0.76*	<0.001	351
Cortex	0.42*	0.003	552
Nucleus	0.64*	<0.001	101
<b>Objective Scatter Index</b>	0.32*	0.025	0.014
<b>Visual function</b>			
AULCSF	-0.38*	0.007	0.0047
VA (LogMAR)	0.37*	0.008	0.0005

Asterisk indicates statistically significant correlation.

The radii of curvature of the anterior lens capsule and both nucleus interfaces declined with age (coefficients  $R_s = 0.70$ ,  $0.67$ , and  $0.30$ , respectively), and statistical significance of the correlation was obtained (Fig. 22b). In particular, a substantial decrease in radius of curvature of the anterior lens was observed with the rate of  $-53 \mu\text{m}/\text{year}$  (Table 4). Although the posterior lens capsule became slightly flatter, there was no statistical significance of the correlation between its radius of curvature and age ( $R_s = 0.17$ ,  $p = 0.304$ ).

The light scattering in the lens was expressed by the optical density defined as the average OCT back-scatter signal taken from a particular region (layer) of the crystalline lens. The optical density of the whole lens, the cortex and the nucleus increased significantly with age (with  $R_s = 0.76$ ,  $0.42$ , and  $0.64$ , respectively; Fig. 22c).

Vision quality degradation with age was characterised by the statistically significant decrease in AULCSF ( $R_s = -0.38$ ,  $p = 0.007$ ) and an increase in VA

expressed in LogMAR units ( $R_s = 0.37$ ,  $p = 0.008$ ) although correlations are relatively weak.

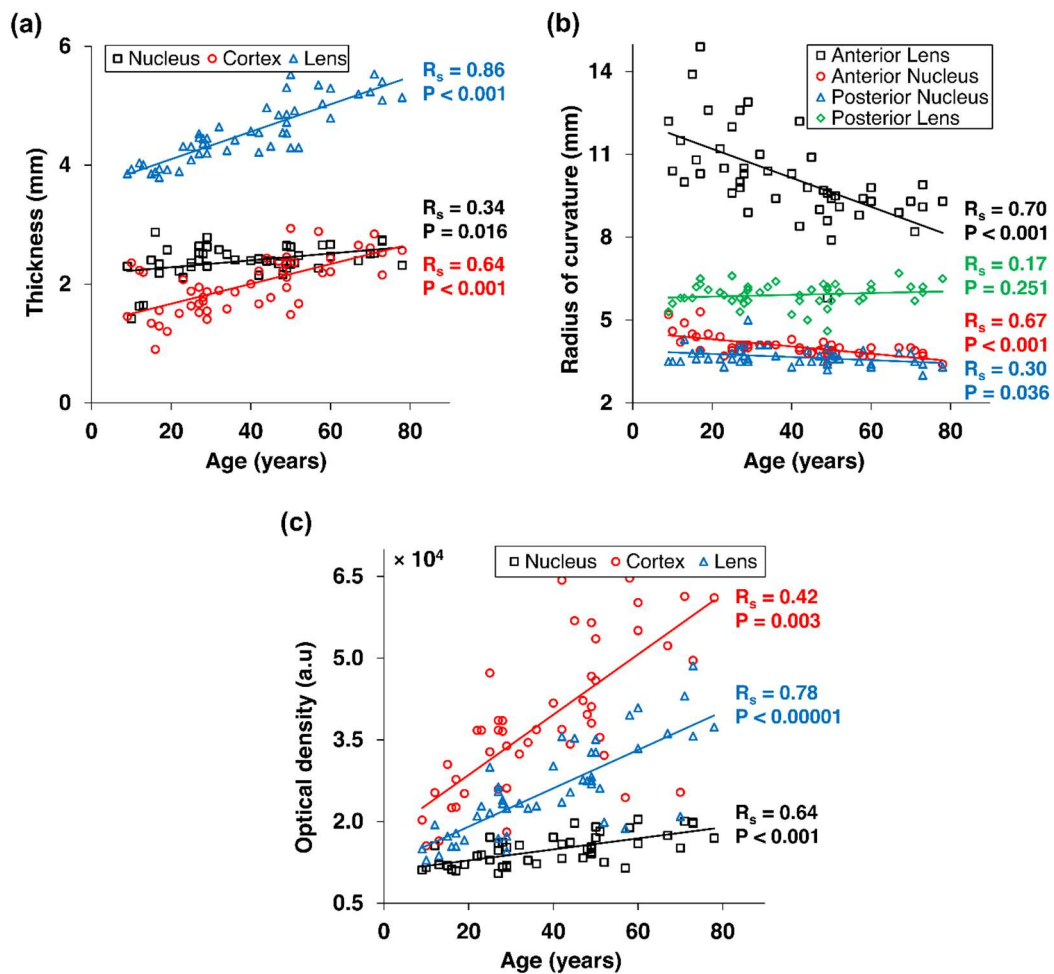


**Figure 22.** Age dependence of measured (a) thickness of nucleus, cortex, and whole lens, (b) radii of curvature of the anterior and posterior lens capsules and the lens nucleus, and (c) optical density of the nucleus, cortex, and lens.

### 3.4.3 Impact of age-related changes on the optical quality of the eye and visual function

I also investigated how the parameters extracted from OCT correlated with the optical quality of the eye (measured with OQAS) and vision (measured with VAO).

The results are presented in Table 5. The optical density of the lens was negatively correlated with AULCSF ( $R_s = -0.35$ ,  $p = 0.0126$ ) but no correlation was found with VA ( $R_s = 0.23$ ,  $p = 0.1080$ ). Moreover, OSI correlated stronger with parameters describing the degradation of vision ( $R_s = -0.42$ ,  $p = 0.0027$  for AULCSF and  $R_s = 0.40$ ,  $p = 0.0045$  for VA). In addition, the increase in light scattering in the lens resulted in an increase in OSI measured for the whole eye with OQAS ( $R_s = 0.41$ ,  $p = 0.0036$ ).

**Table 5.** Spearman’s correlation between the measurements from OCT, OQAS and VAO.

Parameter	Lens optical density (a.u.)	OSI	AULCSF	VA (LogMAR)
Lens optical density (a.u.)				
OSI	$R_s = 0.41^*$ ( $P = 0.0036$ )			
AULCSF	$R_s = -0.35^*$ ( $P = 0.0126$ )	$R_s = -0.42^*$ ( $P = 0.0027$ )		
VA (LogMAR)	$R_s = 0.23$ ( $P = 0.1080$ )	$R_s = 0.40^*$ ( $P = 0.0045$ )	$R_s = -0.60^*$ ( $P < 0.0001$ )	

Asterisk indicates statistically significant correlation.

### 3.5 Discussion

The clinical studies on the development and ageing of the human crystalline lens have contributed to elucidating the changes that lead to the progression of presbyopia and cataracts. Understanding those age-related diseases allow novel treatments to be developed to manage the ageing effects on the eye. In this study, **I demonstrated a detailed quantitative analysis of age-related alterations of morphology and transparency of the human lens, and I assessed the correlations of those changes with vision degradation.**

The current study showed that the central lens thickness increases with age, and the rate change in the lens thickness was estimated to be 0.023 mm/yr. Those observations confirmed previous reports based on Scheimpflug photography, magnetic

resonance imaging and OCT [6, 9, 57, 120, 124, 125, 165, 168, 170-175]. The calculated thickening rate is within the range of 0.019-0.029 mm/yr observed earlier with the standard methods. The increase in lens thickness with age is mainly governed by the thickening of the cortex, which grows at a rate almost three times faster than the nucleus (0.017 mm/yr vs. 0.006 mm/yr, Fig. 22a).

Other age-dependent parameters included lens and nucleus radii of curvature. The results showed a statistically significant decrease in the anterior lens radius, anterior nucleus radius and posterior nucleus radius (at the rates of -0.053 mm/yr, -0.013 mm/yr and -0.006 mm/yr, respectively) within our age range. However, no significant trend in changes in the posterior lens radius was observed (Fig. 22b). Our data suggest agreement with the conclusions from previous *in-vivo* studies where the anterior lens surface became significantly steeper (decrease rate between -0.076 and -0.044 mm/yr). The relation between the posterior lens radius of curvature and age was either not significant or marginally significant [46, 166, 171, 173, 174, 176]. However, age-related changes in the curvature of nucleus-cortex interfaces are not available in the literature, although lens modelling suggests that nuclear curvature becomes flatter [177]. One has to note that correlations of radii of curvature and age become weaker when deeper surfaces are considered. The reasons for that might be the refractive index distribution not exactly represented by a double-shell model in OCT image correction as well as the fact that the refractive indexes were assumed to be independent of age. Therefore, our calculations may introduce deviations from true values.

The cross-sectional OCT images of the lens indicate the non-homogenous character of the optical properties of the crystalline lens (Fig. 21c). OCT signal in the images directly represents light back-scattered and is associated with optical micro-heterogeneity of the lens (the differences in the local refractive index). Much more light is back-scattered from the cortex than that from the nucleus. One can also notice hypo-reflective nuclear sulcus. Quantitative analysis of the images showed that light scattering in the lens increases with ageing, and a high correlation was obtained. Earlier studies investigated that effect and detected non-linear dependence of the densitometric parameter with respect to age (e.g. exponential or bilinear) [129, 173, 178, 179]. In this study, the scatter plots of optical density are rather represented by linear relation, which

confirms other OCT studies (Fig. 22c) [168]. However, different definitions of optical density were used throughout the studies so that the arbitrary units do not allow for a direct comparison of the rates of change.

The densitometric effects similar to those in the crystalline lens were also observed in other ocular components. Age-related opacification was previously measured in the cornea [180-182] and the vitreous [133, 183, 184]. The changes in light scattering in the lens correlated significantly with the scattering in the vitreous [133].

Backward scattering is used to evaluate the condition of the eye in imaging modalities like OCT. However, forward scattering occurring during light propagation through the entire eye contributes to the degradation of the optical performance of the eye. OSI is a biomarker that gives objective information on the image formed on the retina. By definition, intraocular forward scatter degrades the retinal PSF, thus increasing the OSI. I found a significant increase in OSI with age in the group of normal subjects, although the correlation ( $R_s = 0.32$ ) was weaker than that reported in previous studies with the same OQAS instrument [118, 185]. OSI rise with age suggests that enhanced intraocular scattering in older subjects (where the dominating role has light scattering in the crystalline lens) is a factor responsible for the worsened optical quality of the eye. In addition, a moderate correlation between OSI (forward scatter) and optical density of the lens extracted from OCT data (backward scatter) given by  $R_s = 0.41$  comes from the fact that forward and back-scattering are governed by different physical processes [186]. This also explains why the age dependence of OSI is weaker than that for optical densities (Table 3).

The reduced optical quality of the eye compromises the visual performance of the eye studied using the VA test and contrast sensitivity test. We showed that ageing of the crystalline lens is associated with the degradation of VA (increase in VA in logMAR scale) and loss of contrast sensitivity (a drop of AULCSF), which confirms earlier reports [185, 187]. Also, OSI correlated stronger with visual performance metrics than the optical density of the lens did. The reason for that is that OSI measures forward scattering in the eye.

In conclusion, we studied the age-dependency of geometry and light back-scattering of the crystalline lens *in-vivo* and the impact of those changes on optical

quality and the visual performance of the eye. I found that the lens becomes thicker and more convex with ageing. The cortex is primarily responsible for the increase in lens thickness. Changes in the geometry and transparency of the crystalline lens have a significant impact on the optical quality of the eye and its visual performance. Those insights help us understand the ageing processes that often lead to presbyopia and cataract. The results can facilitate the development of emerging strategies for cataract surgery and accommodation restoration.



## Chapter 4

# Changes of optical non-homogeneity of the crystalline lens with age. Optical signal discontinuity zones

### 4.1 Motivation and aim of the study

Another important aspect of crystalline lens ageing that has been of increasing interest in recent years is the role of optical inhomogeneity in understanding those ageing processes. The studies based on cross-sectional images of the crystalline lens (initially using Scheimpflug imaging) have led to distinguishing alternating light and dark regions in the internal lens structure called the optical signal discontinuity (OSD) zones (Fig. 23a). Identification of the OSD zones is a direct consequence of the optical non-homogeneity of the lens since the OSD zones are associated with abrupt changes in refractive index that occur at the boundaries between different regions of the lens. OSD zones are present in all lenses but their thickness and number can vary between individuals and with age.

The use of *in-vivo* and *ex-vivo* imaging techniques has provided valuable insights into the ageing processes of the crystalline lens. The images of the OSD zones have been used for the Oxford clinical cataract classification and grading system [109]. Different imaging modalities have been used to characterise human lens ageing by measuring the shape and refractive status *in-vivo* and in donors' eyes [9, 10, 109, 166, 167, 169, 177, 189-192]. However, the features of internal lens structures, including OSD zones, have not been reported in OCT images. Accordingly, no detailed *in-vivo* OCT study on the contribution of different lens layers to lens transparency and geometry in ageing eyes has been performed. Micrometre-scale resolution and high sensitivity (ability to detect low signals) are the main advantages of OCT with respect to other clinically used imaging methods that facilitate the precise identification of OSD zones.

The aim of this study was to determine the age-related changes in the OSD zones of the crystalline lens. OCT images were used to identify the cortical zones of OSD according to the Oxford nomenclature, and age-related dependencies of the thickness and optical density of OSD zones were presented.

## **4.2 Data acquisition**

In this part of my research, I explored the possibilities of extracting more information from the OCT data that were acquired with a custom-built high-resolution and highly sensitive swept-source OCT system. Hence, I based on the data sets used in the previous study (Chapter 3). Therefore, this cross-sectional study included the scans of 49 eyes (age range: 9-78 years) that were acquired at the Laboratory of Optics at the University of Murcia. The study adhered to the tenets of the Declaration of Helsinki. The volunteers were informed about the nature of the study, and written consent was obtained from each participant in the case of children parental consent was also obtained. The Bioethics Committees at Nicolaus Copernicus University and the University of Murcia approved the study.

## **4.3 Data post-processing and statistical analysis**

### **4.3.1 Densitogram**

Raw OCT data underwent motion correction as well as refraction correction. Later on, the region of interest (ROI) was selected, spanning within a radius of  $66.5\ \mu\text{m}$  around the central axis connecting anterior and posterior lens apices. Hence, the ROI had the shape of a cylinder spreading from the anterior to the posterior lens (Fig. 23c). Data within the ROI were averaged laterally, and an intensity depth profile called a densitogram was generated. Each densitogram highlighted the locations of the OSD zones that can be classified using Oxford nomenclature:  $C1\alpha$ ,  $C1\beta$ , C2, C3, C4, and the nucleus (Fig. 23) [9, 192]. The bright (hyper-reflective) zones with higher optical density are the ones that back-scatter light more, and dark (hypo-reflective) zones are presumably more transparent (optically homogeneous). Once the nuclear and cortical

sub-layers (i.e., C1 $\alpha$ , C1 $\beta$ , C2, C3, and C4) were manually identified in the densitogram, the thickness and optical density within each layer were measured.

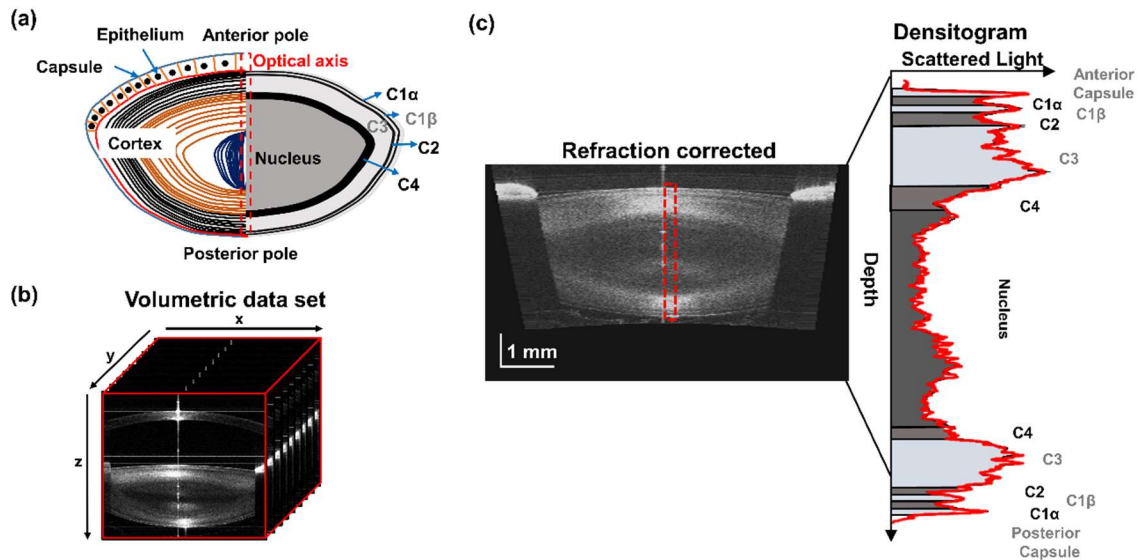


**Figure 23.** (a) Schematic diagram of the crystalline lens (left half: structure of the crystalline lens, and right half: OSD zones) and ROI (red) for generating densitogram for the zones. The epithelial layer is not given in scale. (b) Three-dimensional swept-source OCT volumetric ( $8 \times 8 \times 7 \text{ mm}^3$ ) dataset of a 49-year-old subject. (c) Refraction correction of the central B-scan. The surfaces of the anterior and posterior of the lens (solid yellow) and the nucleus (dashed yellow) were used to measure the radii of curvature. (d) Densitogram of the lens and identification of the OSD zones based on Oxford system nomenclature. The thickness and optical density were measured for each zone.

### 4.3.2 Multivariate linear regression (MLR) model

The SLR model can estimate the linear relationship between only two variables. However, if the dataset comprises multiple independent variables influencing the other variable's outcome, the SLR model can be extended to the multivariate linear regression (MLR) model to observe this influence. This can be expressed as [193, 194]:

$$E(Y_i|x_i) = \alpha_0 + \sum_{i=1}^n \alpha_i x_i, \quad (4.2)$$

where  $n$  is the total number of independent variables,  $E(Y_i|x_i)$  is the expected  $i^{\text{th}}$  value of  $Y$  at a given  $i^{\text{th}}$   $x$  variable,  $\alpha_0$  is the intercept at all  $x = 0$  (intercept is also a mean value of the known  $Y$  variable),  $\alpha_i$  is the coefficient of  $i^{\text{th}}$   $x$  variable (often referred to as the rate  $Y$  values change per unit of  $x$  values).

The main advantage of the MLR approach is that multiple regression analysis assesses the strength of the independent variables' influence over the outcome (the dependent variable). However, for multivariate linear regression analysis on the dataset following four assumptions are made [194]:

1. There is a linear relationship between the dependent variables and the independent variables.
2. The residuals of the data that don't fit the model are normally distributed and independent from each other.
3. The collinearity among the independent variables is minimal.
4. The variance around the regression line is equal or similar for all values of the dependent variable. This measure is called homoscedasticity.

The MLR model was applied (a) to test the significance of the role that the OSD zones play in the changes in the thickness of the crystalline lens, and (b) to investigate if the visual function (from VAO) and optical quality of the eye (from OQAS) change significantly with OCT-measured parameters. It was ensured that MLR is done correctly by checking the normality of the residuals, and if chosen independent variables have low multicollinearity and are homoscedastic.

I selected independent variables based on prior knowledge from the literature, some of the independent variables were removed because they had high multicollinearity. The multicollinearity was checked by computing the variance inflation factor (VIF). VIF describes how much variance is inflated if the independent variables are correlated. VIFs are calculated by taking one independent variable and regressing it against every other independent variable in the model. Therefore, VIF is computed using R-squared values:

$$VIF = \frac{1}{1 - R_i^2}, \quad (4.3)$$

where,  $i$  is an integer value (1,2,3....) for independent variables.

If VIF is

- equal to 1, then independent variables are not correlated.
- between 1 and 5, then independent variables are moderately correlated.
- higher than 5, then independent variables are highly correlated, so multicollinearity is high.

One of the key assumptions of linear regression is that the residuals are distributed with equal variance at each level of the independent variable. The homoscedasticity of the independent variables was analysed using Breusch–Pagan test. The Breusch-Pagan test is used to determine whether or not heteroscedasticity is present in a regression model [195]. The test uses the following null and alternative hypotheses:

- null hypothesis ( $H_0$ ): Homoscedasticity is present (the residuals are distributed with equal variance).
- alternative hypothesis ( $H_A$ ): Heteroscedasticity is present (the residuals are not distributed with equal variance).

If the p-value of the test is greater than the significance level (i.e.  $\alpha = 0.05$ ), then we accept the null hypothesis and conclude that homoscedasticity is present in the regression model.

### 4.3.3 Statistical analysis

Statistical analysis was completed using a statistical toolbox from Microsoft Office Professional plus Excel 2013 (Microsoft Corp., Redmont, WA, USA). Spearman's correlation was performed to investigate age-related changes in the thickness and optical density of OSD zones from the Oxford classification system. The statistical significance of Spearman's correlation coefficient  $R_s$  was tested at the significance level  $\alpha = 0.05$ .

## 4.4 Results

### 4.4.1 Average parameters in the study group

Table 6 illustrates the mean values and standard deviations of the thickness and optical density of OSD zones. The data are extracted from OCT-based densitograms.

**Table 6.** Mean and standard deviations of the thickness and optical density of lenticular OSD zones from the 49 eyes.

<b>Variables</b>	<b>Unit</b>	<b>N</b>	<b>Mean (SD)</b>
<b>Thickness</b>	<b>mm</b>	<b>49</b>	
Nucleus			$2.39 \pm 0.27$
C1 $\alpha$			$0.16 \pm 0.04$
C1 $\beta$			$0.20 \pm 0.07$
C2			$0.27 \pm 0.08$
C3			$1.07 \pm 0.38$
C4			$0.30 \pm 0.08$
<b>Optical density</b>	<b>a.u.</b>	<b>49</b>	
Nucleus			$(14.8 \pm 2.9) \times 10^3$
C1 $\alpha$			$(33.6 \pm 7.4) \times 10^3$
C1 $\beta$			$(39.8 \pm 7.4) \times 10^3$
C2			$(33.1 \pm 8.9) \times 10^3$
C3			$(4.3 \pm 1.1) \times 10^4$
C4			$(25.5 \pm 6.5) \times 10^3$

### 4.4.2 Age-related changes in the thickness and transparency of OSD zones

Table 7 presents the significance of the correlation of thickness and optical density of OSD zones with age. The calculated rate of change (with respect to time of life span) is also included. Among all cortical OSD zones (according to the nomenclature of the Oxford system), the highest correlation of thickness with age was found for the C3 layer ( $R_s = 0.70$ ,  $p < 0.001$ ), and the thickening rate of the C3 zone (0.0146 mm/year) was close to that of the entire cortex. The thickness of the C1 $\alpha$  zone also correlated significantly with age. On the other hand, the changes in the thickness

of C1 $\beta$ , C2 and C4 did not show a significant correlation with age. Unlike the C1 zone, all cortical OSD zones demonstrated increasing light scattering with age (positive rates of changes in Table 7).

**Table 7.** Correlation of measured parameters with age.

Dependent Variables	R <sub>s</sub>	P-value	Rate of change (per year)
<b>Thickness (mm)</b>			
Nucleus	0.34*	0.016	0.006
C1 $\alpha$	0.41*	0.003	0.001
C1 $\beta$	<b>0.25</b>	<b>0.083</b>	<b>0.0011</b>
C2	<b>-0.02</b>	<b>0.892</b>	<b>-0.0002</b>
C3	0.70*	<0.001	0.0146
C4	<b>0.1</b>	<b>0.494</b>	<b>0.0006</b>
<b>Optical density (a.u.)</b>			
Nucleus	0.64*	<0.001	101
C1 $\alpha$	-0.37*	0.009	-128
C1 $\beta$	<b>-0.05</b>	<b>0.733</b>	<b>-33</b>
C2	0.45*	0.001	234
C3	0.74*	<0.001	434
C4	0.56*	<0.001	200

Asterisk indicates statistically significant correlation.

A more detailed analysis was later completed for the thickness of the lens and each OSD zone. I tested the statistical significance of the difference between the growth rates of corresponding anterior and posterior OSD zones. Figure 24 presents the changes in the thickness of the anterior and posterior cortical OSD zones with age. No significant differences between the growth rates of anterior and posterior lenticular zones were found.

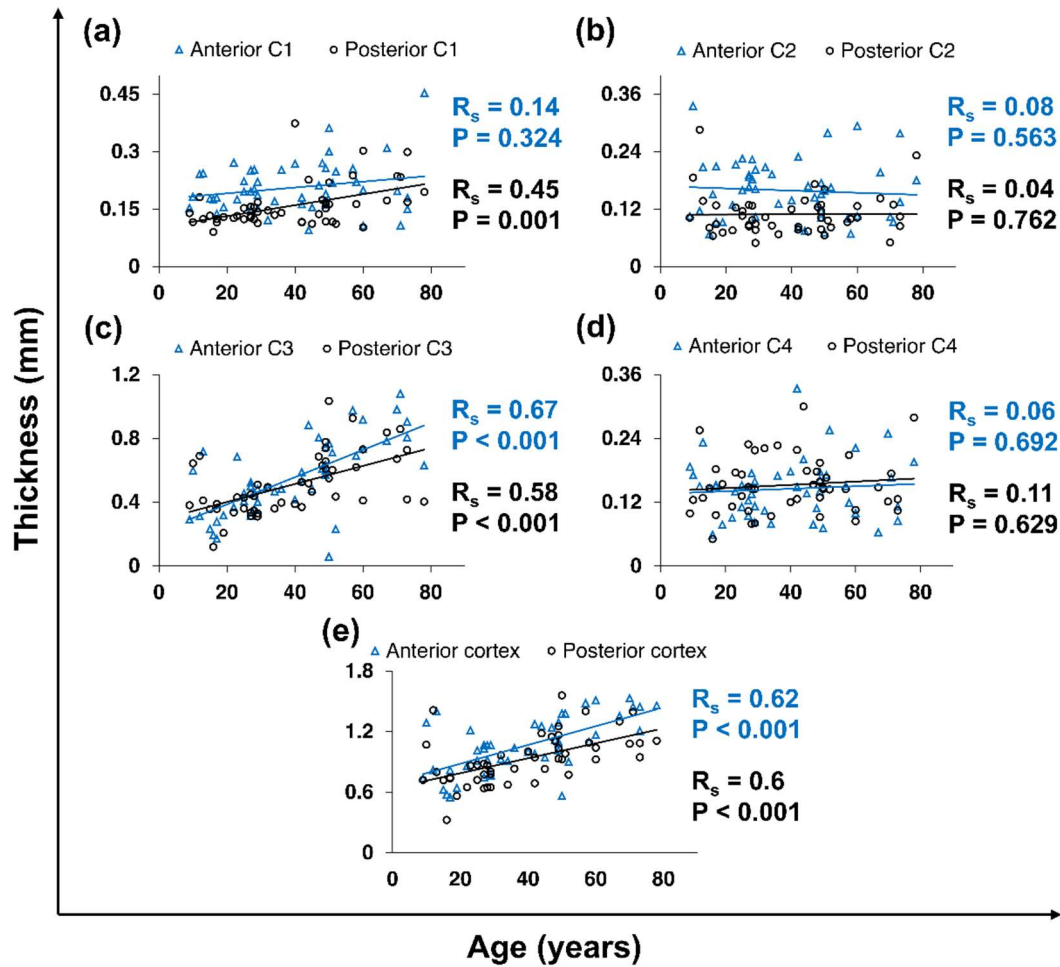


**Figure 24.** Relation of ageing with changes in the anterior and posterior thickness of the cortex and its sub-layers (C1, C2, C3, and C4).

The data were further investigated by categorisation based on age groups. The entire population was split into seven age groups, from 9 to 78 years old. The thickness of each cortical zone was expressed as the percentage of the entire central lens thickness. This allowed us to observe the contribution of the thickness of the OSD zones to the lens thickness growth.

In Fig. 25, pie charts depict how the relative thickness of each zone changes with age. Access to cortical sub-layers revealed that the bright C3 zone was mainly responsible for the growth of the overall cortex and thus contributed to the development of the crystalline lens (from 45% to 58% in Fig. 25). Furthermore, the relative thickness of dark zones, C2 and C4, decreased with age, whereas the contribution of C1 layer thickness is minimal and remained rather consistent with age.

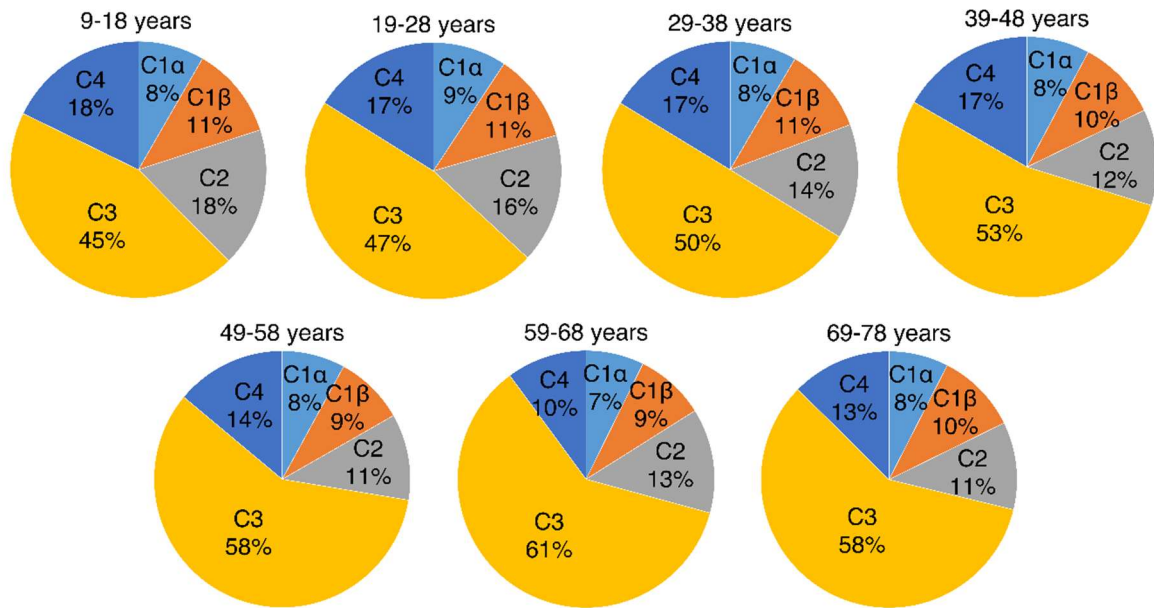


**Figure 25.** Percentage contribution of cortical layers to the total cortical thickness for different age groups.

#### 4.4.3 Factors influencing lens thickness and optical density

Influencing factors on crystalline lens thickness and lenticular optical density were also explored by MLR analysis. The independent variables for both dependent variables were homoscedastic, confirmed by Breusch–Pagan test.

The variables with high multicollinearity were avoided to have an unbiased analysis. MVLRL analysis showed that the thickness of the nucleus ( $\beta = 0.27$ ,  $p < 0.001$ ) and cortical layers (C1 $\alpha$   $\beta = 0.04$ ,  $p = 0.021$ ; C1 $\beta$   $\beta = 0.07$ ,  $p = 0.001$ ; C2  $\beta = 0.1$ ,  $p < 0.001$ ; C3  $\beta = 0.38$ ,  $p < 0.001$ ; C4  $\beta = 0.09$ ,  $p < 0.001$ ) had a strong influence on the crystalline lens thickness, with adjusted  $R^2 = 0.97$ .

Lens optical density was highly influenced, adjusted  $R^2 = 0.87$ , by optical densities of the nucleus ( $\beta = 4835$ ,  $p < 0.001$ ), and C3 (bright zone) ( $\beta = 2997$ ,  $p = 0.04$ ) as well as OSI ( $\beta = 2025$ ,  $p = 0.004$ ). However, there was no significant influence,  $p > 0.05$ , of optical densities from C1 $\alpha$  ( $\beta = -1029$ ), C1 $\beta$  ( $\beta = -466$ ), C2 ( $\beta = 1197$ ), and C4 ( $\beta = -236$ ) as well as AULCSF ( $\beta = 102$ ), and VA ( $\beta = 456$ ).

MVLR analysis also revealed that visual acuity (VA) is influenced by AULCSF ( $\beta = -0.001$ ,  $p = 0.007$ ), the radius of curvature of the anterior lens ( $\beta = 0.022$ ,  $p = 0.025$ ), anterior nucleus ( $\beta = -0.019$ ,  $p = 0.0098$ ), and posterior nucleus ( $\beta = 0.015$ ,  $p = 0.042$ ).

## 4.5 Discussion

Compared with Chapter 3, the study in this section is related to a more detailed OCT image analysis. Visual inspection of OCT images of the lens revealed that the crystalline lens is not an optically homogenous structure. Previous studies using Scheimpflug imaging identified the OSD zones that are a consequence of the optical inhomogeneity of the crystalline lens structure [11]. Dubbelman et al. demonstrated densitograms from low-resolution Scheimpflug images, which resulted in a C1 layer that could not be further divided into C1 $\alpha$  and C1 $\beta$ . Moreover, their results also lacked a clear boundary between the C4 zone and the nucleus, so C4 was excluded from the measurements [9]. OCT instrumentation was utilised to perform *in-vivo* imaging of the anterior segment of the eye and to investigate different aspects of ocular ageing [14, 165, 191, 196]. However, no study was reported in which OSD zones were visualised with OCT. **I took advantage of specific features offered by SS-OCT modality, such as high resolution and sensitivity that enabled the acquisition of high-quality images allowing us to identify OSD zones in densitograms.** These zones were extracted (C1 $\alpha$ , C1 $\beta$ , C2, C3, C4, and nucleus) following the Oxford nomenclature that was initially used to categorise cataract types based on their location in the crystalline lens [108]. **This is the first comprehensive study on OSD zones and new OCT application.** OCT outperforms Scheimpflug imaging in terms of resolution and ability to detect low back-scattered signals; thus more details could be extracted and quantified.

Although the increase in lens thickness with age is mainly governed by the thickening of the cortex, I found differences between the rates of thickness change within the cortical OSD zones. The thickness of zones C1 $\alpha$  and C3 increased significantly with age (0.0010 mm/yr and 0.0146 mm/yr, respectively). On the other hand, the changes in the thickness of C1 $\beta$ , C2 and C4 did not show a significant correlation with age (Table 6). This contradicts the report of Dubbelman et al. who

demonstrated that only the C2 zone had a dominant and statistically significant role in lens thickening with age, with a higher rate in the anterior cortex [9]. Unlike Dubbelman et al. and Cook et al., there was no significant differences in thickness change rates between the anterior and posterior cortex (Fig. 24) [9, 124]. However, the poor resolution of the Scheimpflug camera and the low accuracy of determination of all OSD zones from Scheimpflug images could explain the discrepancies.

Furthermore, the mutual contribution of each OSD zone to the overall thickness of the cortex was studied. The comparison within age groups revealed that since the bright and thickest C3 zone grows fast, its contribution increased from 45% to 58% of the total thickness at the expense of the C2 and C4 hyporeflective zones (Fig. 25). I also observed that C1 maintains percentage contribution during ageing. Therefore, it is confirmed that all bright OSD zones in the crystalline lens grow with age, adding more cellular fibres in each zone. In contrast, dark zones (C2 and C4) do not go through consistent thickness increase, and thus the process of compaction may occur in those zones.

I also showed that the highest increase in scattering occurs in the hyper-reflective zone C3, which was also demonstrated in the studies with Scheimpflug imaging [110, 127]. Interestingly, the optical density of the C1 zone declined with age, unlike in C2, C3, and C4 zones. A closer inspection shows that the correlation of the optical density with age is highly significant in the case of C1 $\alpha$ , whereas C1 $\beta$  has poor significance (Table 6).

The analysis using MVLR indicated that the thickness of OSD zones as measured by OCT has a significant impact on the total thickness of the crystalline lens, with the nucleus and C3 layer having the most statistical significance. Moreover, these layers affect not only the lens thickness but also its optical density. In addition, the MVLR results showed that the visual acuity of the eye is significantly influenced by the anterior and posterior radius of curvatures of the lens, as well as the AULSCSF. This suggests that the shape of the lens is one of the factors that affect visual acuity.

In conclusion, 3-D OCT enables high-resolution crystalline lens imaging with high sensitivity to distinguish the lenticular OSD zones. The most significant age-related changes occur in the C3 zone as it thickens faster and becomes more opaque

than other OSD zones. Evaluation of light scattering in the lens demonstrates that the nucleus and C2-C4 zones contribute to the general opacification of the crystalline lens.

## Chapter 5

### ***In-vivo* imaging of lenticular sutures and effect of ageing on suture architecture**

#### **5.1 Motivation and aim of the study**

Natural sutures present in the crystalline lens are a direct consequence of fibre cell organization in the lens (Fig. 26a). The sutures play a critical role in maintaining the structural integrity and optical properties of the lens. The crystalline lens has highly ordered layered fibres that meet at the lens optical axis (along the lenticular poles), forming micro-scale sutures. The sutures contribute to the metabolism processes in the crystalline lens by facilitating the nutrient flow from the cortex to the nucleus and supporting the maintenance of lens homeostasis and playing a role in optical quality (aberrations) [9, 64-67, 197, 198]. The interdigitating processes that make up the sutures provide a high degree of mechanical stability to the lens, allowing it to maintain its shape and focus light onto the retina. The distribution of forces within the lens is critical for maintaining the optical properties of the lens and ensuring that light is focused correctly onto the retina [7, 199, 200].

As we age, the sutures of the crystalline lens undergo many changes that can affect their structural and mechanical properties. One of the most significant changes is characterized by an increase in the branch number and complexity of the sutures, which may influence the transparency and mechanical properties of the lens [10, 41, 197]. This may lead to presbyopia and suture cataracts [42, 43]. In addition to that, alterations in the alignment and geometry of the sutures can also occur with age. What is more, the changes in the sutures can result in localized areas of stress, which can lead to the development of lens opacities or even lens dislocation. At suture sites, lens fibre ends are non-uniform, unlike their lengths, and thus are more scattering. Accordingly, the abnormal development of sutures is associated with specific types of cataracts (sutural cataracts) [202]. In addition, surgical interventions like trabeculectomy and vitrectomy

may result in post-surgical alterations in lens sutures that precede cataract formation [202, 203].

The complexity of the suture patterns increases with age with adding more fibre cell layers at the periphery of the lens. Understanding the changes that occur in the sutures of the crystalline lens with age is critical for developing interventions to slow or prevent the progression of lens-related conditions. As such, a significant amount of research is currently focused on investigating the structure and function of the sutures and their role in maintaining the optical properties of the lens.

The presence of sutures is a consequence of the lens microstructural organization. From the optical point of view, 3-D shape of sutures in the lens leads to optical inhomogeneity of the lens. Previous studies suggest that sutures induce optical aberrations like spherical aberrations [12, 43, 161, 163, 197]. The light passing through the crystalline lens is highly scattered compared to neighbouring sites. Fundamental studies on lenticular suture visualisation were performed using the techniques like point diffraction interferometry, and light and electron microscopy [40, 41, 204-209]. Laser ray tracing was used to evaluate the effect of sutures on retinal image quality and aberration [197, 210]. *In-vivo* imaging of sutural cataracts was performed using biomicroscopy [27, 211, 212]. Although those reports gave important insights into the relationship between the suture pattern of the lens and optical quality, the studies were mostly limited to *ex-vivo* animal studies, *in-vitro* specimens or only two-dimensional *en-face* imaging.

By visualizing the sutures *in-vivo*, the researchers can gain a better understanding of their structure and function and how they change with age. OCT can surpass the *in-vivo* imaging limitations of other modalities by providing a highly sensitive high-resolution 3-D *in-vivo* imaging of lens suture architecture in a non-contact and non-invasive way [132]. This study aimed to demonstrate *in-vivo* imaging of the human crystalline lens sutures from the 3-D OCT data and to describe sutural structure quantitatively.

## 5.2 Data acquisition

This was an observational cross-sectional study that was conducted at the University of Murcia and adhered to the tenets of the Declaration of Helsinki. The acquisition of volumetric data sets was completed at the Laboratory of Optics at the University of Murcia. The Institutional Review Boards approved the study at Nicolaus Copernicus University and the University of Murcia. The study enrolled 100 eyes of 50 individuals (mean age: 40 years, age range: 9-78 years). The participants underwent a standard ophthalmic examination. Participants with previous ocular surgery were excluded from the study. The volunteers were informed about the nature of the study, and a written consent was obtained from each participant. No pupil dilation was used in this study. The scanning procedures were completed under constant conditions of dim illumination.

## 5.3 Data post-processing and statistical analysis

### 5.3.1 Imaging of lenticular sutures

A 3-D volumetric OCT data set consisting of  $300 \times 300$  A-scans and covering an  $8 \times 8 \text{ mm}^2$  area was obtained from each subject (Fig. 26b). The motion-corrected volumes of data revealed high-resolution OCT images of the crystalline lens. The cross-sectional B-scans were used to identify the anterior and posterior cortex as well as the fetal nucleus from the literature. The volumetric OCT images allowed us to generate *en-face* images of the lens segmented areas and extract suture patterns.

### 5.3.2 Methods of extraction of suture features

An OCT volumetric data comprises multiple B-scans acquired based on raster scanning over the region of interest (Fig. 26a-b). The data were corrected for motion artefacts (as described in Section 3.3.1). The advantage of operating with 3-D data is that it is possible to generate virtually any possible cross-section and projection. In particular, both anterior and posterior intensity *en-face* projection images were generated from axially averaged slabs (ca.  $320 \text{ }\mu\text{m}$  thick) below the anterior interface

and above the posterior interface of the lens, respectively (Fig. 26c). Therefore, the entire depth of the cortex was not included in the slabs. Axial averaging of the OCT signal from OCT images was implemented to form an average intensity projection (AIP) image (Fig. 26c).

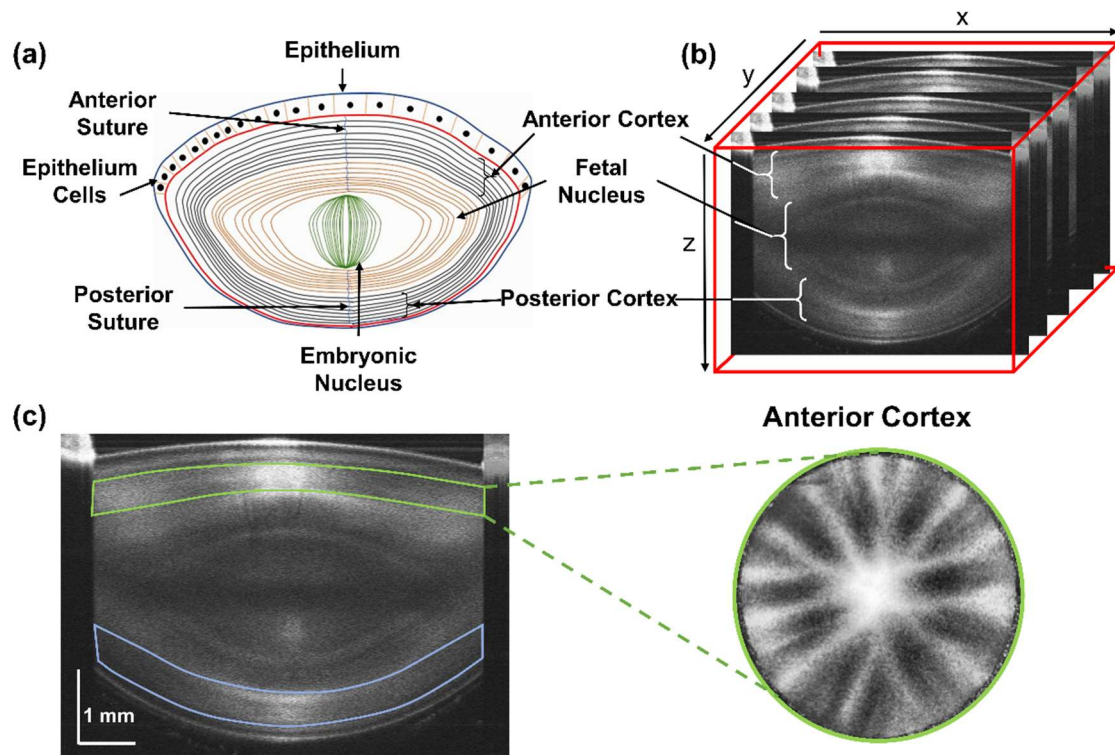


**Figure 26.** (a) Anatomy structure of the human crystalline lens. (b) OCT volumetric data of the crystalline lens of  $8 \times 8 \times 4 \text{ mm}^3$ . (c) Illustration of the segmented cortex and generation of average intensity projection (AIP) image of the anterior cortex. Star-shaped sutures are visible in AIP image.

The exact position and thickness of the slab within the lens cortex layer were set individually to obtain the optimum AIP image contrast by visual inspection of the projection images. The anterior and posterior cortex projection images demonstrate complex star suture patterns in the anterior and posterior lens. The sutures appear as hyper-intensive lines that radiate from the pole toward the equator. A similar manual approach was applied to the lens nucleus (the slabs were ca.  $80 \mu\text{m}$  thick in this case). In this case, we could also identify Y-shaped sutures (and inverted Y-sutures) that are

characteristic of the early development of the lens. Y-sutures were visible in 56 volumetric images (61% of all data sets).

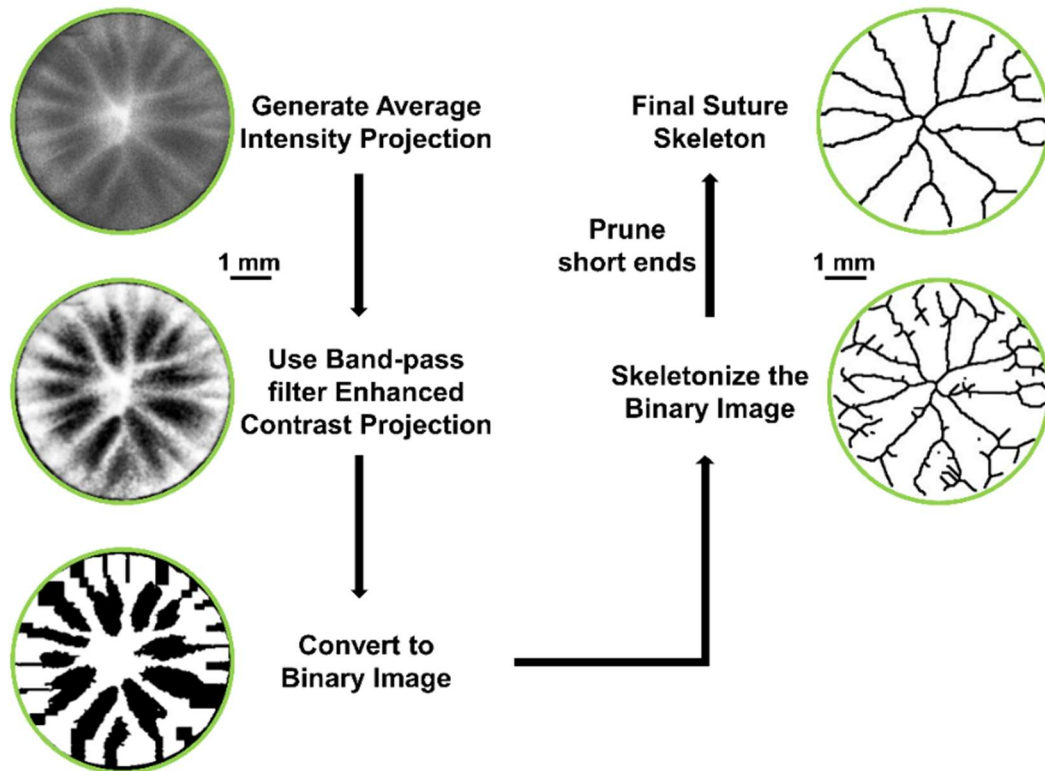


**Figure 27.** Flow chart of the image processing and extraction of suture pattern algorithm; averaged intensity *en-face* projection of anterior lens suture, image contrast enhancement with bandpass filtering and CLAHE (contrast limited adaptive histogram equalisation) contrast enhancement, image binarisation, image skeletonisation, pruning ends and false branches.

I developed a semi-automatic image processing algorithm in ImageJ to obtain a suture pattern from the selected (anterior or posterior) AIP image of the cortical layer of the crystalline lens. The protocol comprises several steps, as shown in Fig. 27. First, a band-pass filter was applied to enhance the contrast between suture branches and the background signal in the AIP image. The band-pass filter was set to have large structures filtered down and small structures filtered up to 40 pixels and 3 pixels, respectively. The direction tolerance of the filter was set to 5%. Image intensity was

rescaled after filtering to match the range of display values. Further enhancement of images was done with contrast limited adaptive histogram equalisation (CLAHE) algorithm (no mask, block size 127, histogram bins 256, normal speed for high accuracy) [43]. Then, the enhanced AIP image was binarised by thresholding the signal. A robust automatic threshold selection (RATS) algorithm was applied to set the threshold level (estimate of the noise 5, scaling factor 3, and min leaf size 60) [44]. Later, binary projection underwent automatic skeletonisation based on thinning algorithm, which enabled obtaining suture patterns with false, short ends or small branches [45]. At final step to get a suture pattern included pruning those false ends/branches using the ‘shortest branch’ prune cycle method. Some remaining false short branches were also removed manually.

The procedure described here was applied to both anterior and posterior projection images so that I obtained two skeletonised suture images (anterior and posterior) from each measured eye. The sutures formed the planes, in projection, appeared as branches.

### **5.3.3 Comparison of manual and semi-automatic methods for suture segmentation. Bland-Altman analysis**

The semi-automatic algorithm to extract the shape of the sutures can be validated with respect to the manual method. Thus, it was observed that two methods could extract the results for the same query during data analysis. In statistics, Bland-Altman analysis is used to compare both methods ( $M_1$  and  $M_2$ ) and deduce whether the difference between their results is acceptable [213]. The measurement methods, called  $M_1$  and  $M_2$ , are compared by plotting the mean results of both methods against the difference between the results. In Cartesian form, the Bland-Altman plot can be represented as [214]:

$$M(x, y) = \left\{ \frac{M_1 + M_2}{2}, M_1 - M_2 \right\}. \quad (5.1)$$

The condition for acceptable difference limits if data points of  $M(x,y)$  lie within 95% of the confidence level. The data points should not lie above the mean +  $(1.96 \times SD)$  and below the mean -  $(1.96 \times SD)$ , where  $SD$  is the standard deviation.

Validation of the proposed algorithm was performed by the assessment of the ability of the algorithm to detect the sutures. The suture branches were counted using the obtained skeleton patterns and compared with the number of sutures detected manually by a trained grader in corresponding AIP images. The grader did not know the age or the output of the semi-automatic algorithm.

### **5.3.4 Quantitative description of lenticular suture pattern**

Different parameters were extracted to describe the architecture of the crystalline lens sutures quantitatively:

*a) anterior cortex mean signal:* The inverse mask of the anterior sutures masked the AIP image from the anterior lens. The average signal was calculated. This quantity shows the average signal in the anterior AIP image in the regions outside sutures.

*b) anterior suture mean signal:* The suture pattern mask masked the AIP image from the anterior lens. The average signal was calculated. This quantity shows the average signal from sutures in the AIP image.

*c) posterior cortex mean signal:* The inverse mask of the posterior sutures masked the AIP image from the posterior lens. The average signal was calculated. This quantity shows the average signal in the posterior AIP image in the regions outside sutures.

*d) posterior suture mean signal:* The suture pattern mask masked the AIP image from the posterior lens. The average signal was calculated. This quantity shows the average signal from sutures in the AIP image.

*e) suture density index:* The number of pixels indicating sutures in the skeletonised image was divided by the number of pixels covering the pupil area.

The parameters mentioned above were calculated in the circular region of interest with a diameter of 3.5 mm, corresponding to the group's smallest pupil.

### **5.3.5 Statistical analysis**

Statistical analysis was completed using a statistical toolbox from Microsoft Office Professional plus Excel 2013 (Microsoft Corp., Redmont, WA, USA). The

statistical significance of Pearson correlation coefficient  $R$  was tested at the level  $\alpha = 0.05$ .

The SLR model is used to observe statistical linear relationships between two variables in the data set and to measure the linearity with the help of Pearson's correlation coefficient.

## **5.4 Results**

### **5.4.1 Suture visualization strategies from volumetric OCT data**

The suture architecture can be shown using different strategies. 3-D data allow the generation of projection images, where the sutures appear as hyper-reflective lines that radiate from the pole toward the equator (Fig. 28b). Additionally, access to volumetric data enables the generation of 3-D rendering of the sutures that are represented by the surfaces where the fibre cells meet each other (Fig. 28c). A characteristic Y-suture pattern is illustrated in the fetal nucleus (yellow and blue), and complex star sutures in the anterior (red) and posterior lens (green) are shown.

The sutures from the lens anterior and posterior hemispheres can be superimposed (Fig. 29a). I also observe that the suture pattern from the posterior lens is rotated about 20 degrees clockwise with respect to the suture pattern from the anterior lens. Moreover, it is possible to represent the suture complex organisation in the polar coordinate system (Fig. 29b). The dendritic pattern of sutures as well as correspondence between anterior and posterior suture branches can be explored with this transformation. However, one has to remember that OCT does not enable the exploration of sutures up to the lens equator since the lens sampling area is limited by pupil size and no peripheral regions are imaged. Additionally, no refraction correction was applied to the data. Consequently, the polar representation does not cover the entire lens interface, and the information on how the anterior and posterior sutures are connected cannot be retrieved.

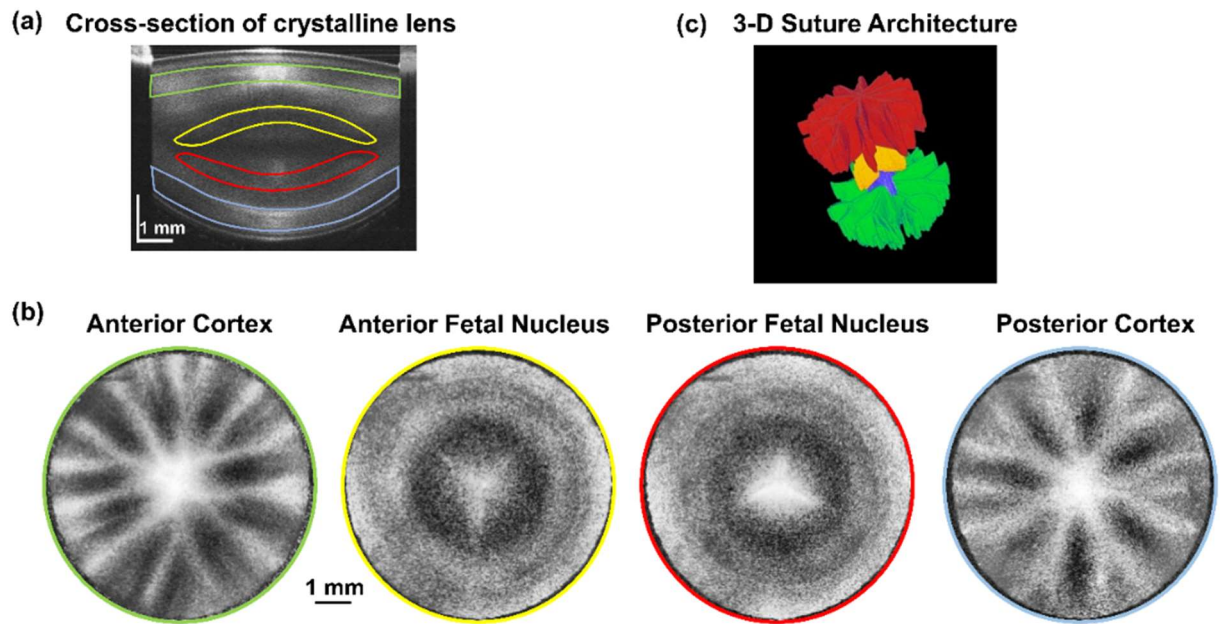


**Figure 28.** (a) Cross-sectional segmentation of cortex and nucleus, (b) AIP projections of segmentations reveal sutures at: anterior cortex – star-shaped sutures (green), anterior fetal nucleus – Y sutures (yellow), posterior fetal nucleus – Y sutures (red), and posterior cortex – star-shaped sutures (blue). (c) 3-D suture architecture in the whole crystalline lens. Data presented here is the anterior crystalline lens from the right eye of a 40-yr subject.

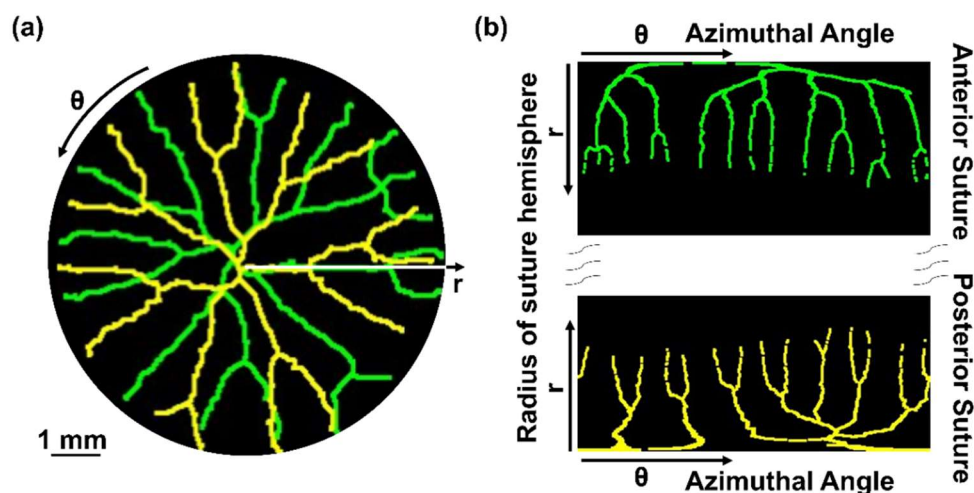


**Figure 29.** Anterior (green) and posterior (yellow) suture pattern in the crystalline lens of the right eye of a 40-yr subject. (a) Representation in the Cartesian coordinate system. (b) Representation in the polar coordinate system.

Detailed examination of obtained projections made it also possible to notice hypo-reflective zones surrounded by regular hyper-reflective lines within the sutures (red arrow in Fig. 30). This effect was observed in 22 eyes (24% of all data sets used for analysis).

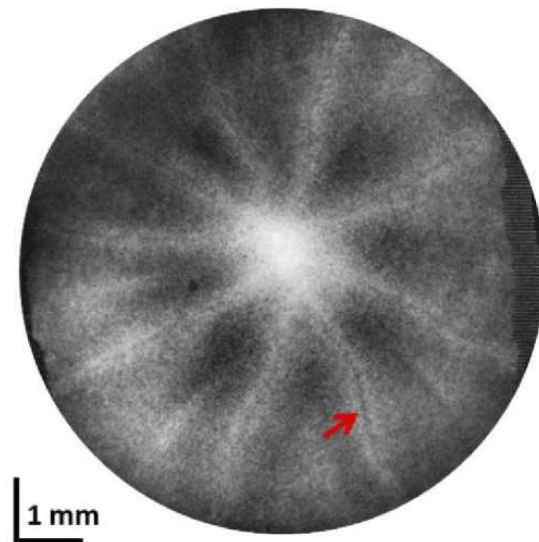


**Figure 30.** Enhanced-contrast AIP of the right eye of the 28-yo subject. Red arrow clearly shows non-homogenous nature of light scattering in suture region.

#### **5.4.2 Agreement between semi-automatic and manual method of suture extraction**

Agreement between both methods of suture segmentation was assessed using Bland-Altman analysis. The validation procedure was based on counting the number of detected suture branches (in skeleton patterns) in both the lens anterior and posterior poles. On the other hand, the suture branches were counted manually using generated AIP suture images. Fig. 31 demonstrates the correlation between applied approaches (left column) as well as the Bland-Altman plots (right column).

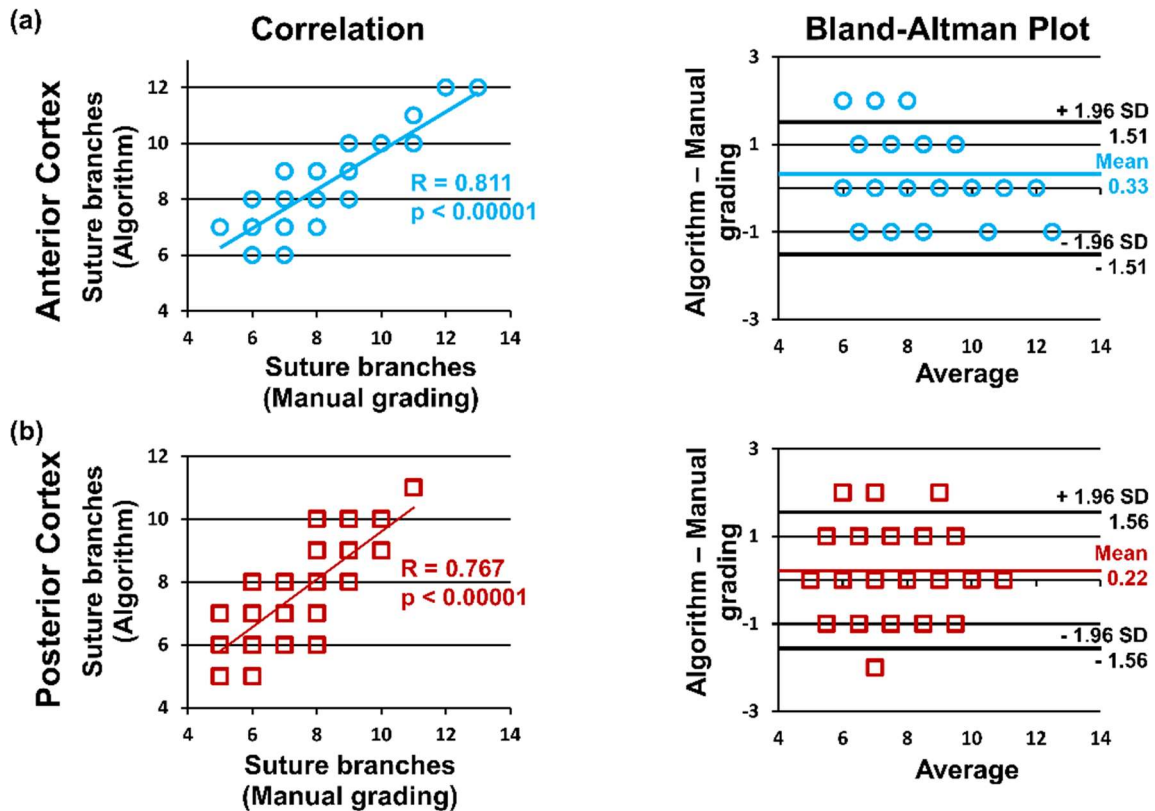


**Figure 31.** Validation of the algorithm for suture pattern extraction. Comparison and agreement between semi-automatic algorithm and manual grading of the AIP images: (a) anterior lens sutures and (b) posterior lens sutures. The plots demonstrate the correlation between the detected number of suture branches (left column) and Bland-Altman plots (right column).

A high and statistically significant correlation was found between semi-automatic and manual counting of suture branches in both the anterior and posterior cortex ( $R = 0.811$ ;  $p < 0.00001$  and  $R = 0.767$ ;  $p < 0.00001$ , respectively). The semiautomatic algorithm also demonstrates a very good agreement with the manual grading of the suture pattern. The maximum difference between both methods does not exceed 2.

### 5.4.3 Suture patterns in ageing lenses

The examples of images and corresponding anterior suture patterns of human lenses of different ages are presented in Fig. 32. Visual inspection and comparison of

OCT B-scans and projection images demonstrate progressively stronger lens signals with age as the intraocular scattering increases. In particular, the cortex and the nucleus become more reflective, which can be easily noticed by comparing the images of young and old subjects (Fig. 32, middle row).

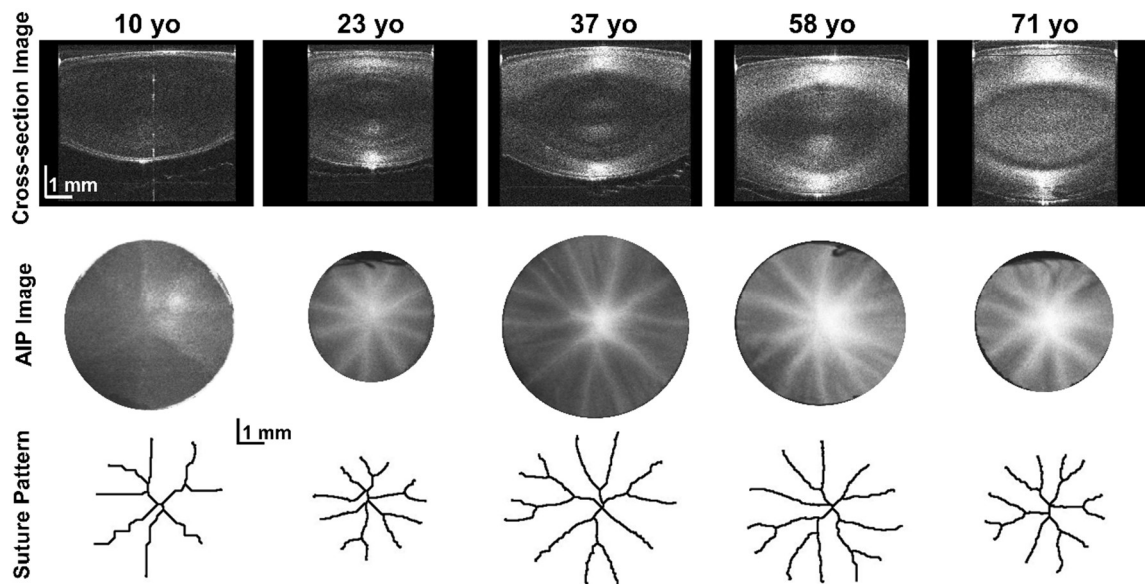


**Figure 32.** The crystalline lens and suture pattern in the ageing eye. OCT cross-sectional image (upper row), AIP images (middle row) and extracted anterior suture patterns (bottom row) of human lenses in different decades of human life.

The analysis of the suture patterns indicates the age-dependent development of sutures in the crystalline lens. The lens of a 10-yo person in Fig. 32 features a simple six (or seven-) branch suture pattern, which is the simplest form of star sutures [41]. The suture architecture becomes even more complex in adolescence. The number of branches of the complex star pattern increases reaching 9, 12 or sometimes even more branches.

#### 5.4.4 Age-related changes in the crystalline lens suture patterns

The number of branches extracted in the anterior cortexes was, statistically, pseudo-equal to the number of branches extracted in the posterior cortexes from our

data with  $R = 0.991$  and  $p < 0.00001$  (Fig. 33a). As the line fit on the data was below line  $y = x$ , it was observed that fewer suture branches were visualised in the posterior lens cortexes compared to the number of visualised sutures in the anterior lens cortexes. The number of detected branches increases slightly with age but with no statistical significance ( $p > 0.2$ ) (Fig. 33b).

I also introduced the parameter, suture density index, which describes the total length of sutures related to the number of pixels covering the circular region of interest. The results present a statistically significant (but weak) correlation of suture density index with age for anterior suture patterns,  $R = 0.213$ ,  $p = 0.043$ . However, no correlation is observed between age and the suture density index for the posterior cortex of the crystalline lens ( $p = 0.12$ ) (Fig. 33c).

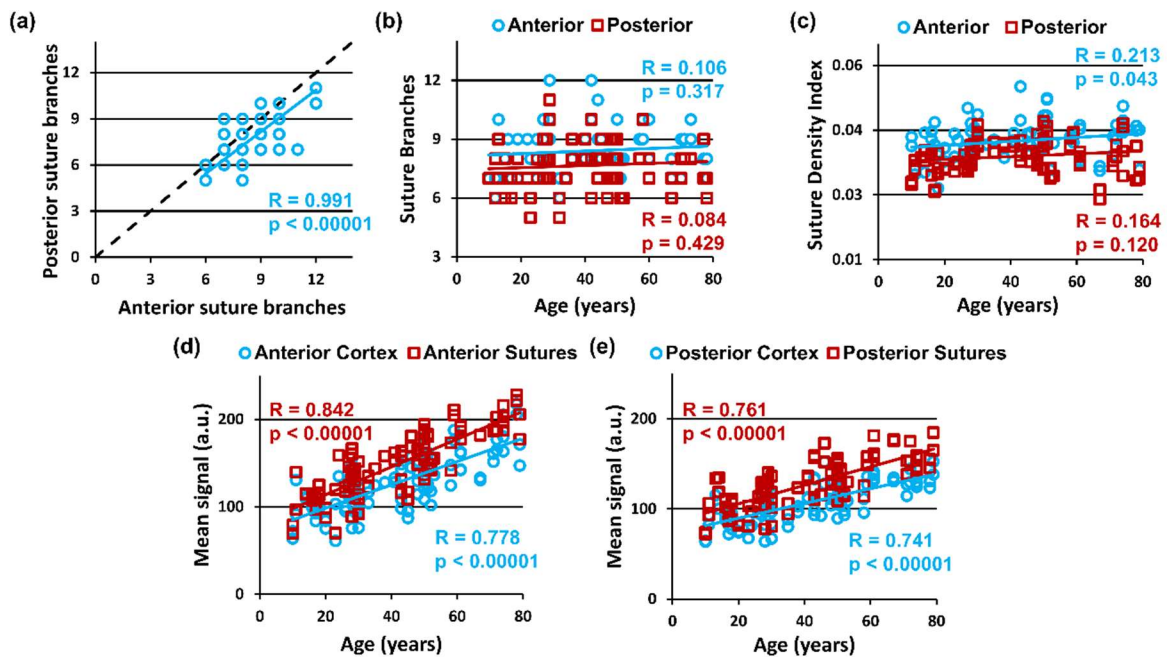


**Figure 33.** Quantitative analysis of the human lens suture pattern *in-vivo*. (a) Relation between the number of branches in the posterior lens and the number of branches in the anterior lens. The dashed line represents the equality of the numbers. (b) Age-related changes in the number of branches. (c) Age-related changes of the suture density index. (d) Age-related changes in the mean signal of the anterior cortex and the anterior suture pattern derived from AIP images. (e) Age-related changes in the mean signal of the posterior cortex and posterior suture pattern derived from AIP images.

Furthermore, I analysed the signal in the AIP images of the anterior and posterior cortexes (Fig. 33d-e, respectively). The plots show that the averaged signal from the cortex and the averaged signal taken along the corresponding sutures are highly correlated with age, with  $p < 0.00001$ . In addition, the increase rate of the suture signal is higher than that of the cortex signal. The anterior suture signal increase rate per year is 119% more than the anterior cortex signal, whereas the posterior suture signal increase rate is 125% more than the posterior cortex signal.

## 5.5 Discussion

In this chapter, I demonstrated the 3-D visualisation of sutures in human crystalline lenses *in-vivo* using OCT. **A comprehensive *in-vivo* analysis of human lens suture organisation in the ageing eye has not been reported before although anterior segment swept-source OCT was widely used for crystalline lens imaging** [20, 114, 131, 140, 149, 215, 216]. The OCT images of the lenticular sutures were shown before in rodent and human eyes [131, 132, 149]. Previous reports on human lenticular sutures were mostly limited to *ex-vivo* or *in-vitro* conditions. Moreover, microscopic modalities used in earlier studies did not enable volumetric imaging and a large field of view, although they provided extremely high-resolution images [28, 162, 197, 205, 207, 217, 218].

SS-OCT features several advantages that address the challenges of suture visualisation and facilitate new imaging applications even in subjects with no diagnosed cataract. Firstly, OCT imaging is well-suited for lenticular suture imaging. Lenticular sutures appear in projection images as regions with higher reflectivity as the result of optical inhomogeneity inside the lens. Elevated light scattering in the suture branches, which were observed in OCT AIP images, was consistent with the fact that lenticular sutures are formed by the abutting ends of cell fibres, which was confirmed in several microscopic studies [40]. This natural microstructural discontinuity can be directly related to optical heterogeneity, which results in higher scattering as light passes through these regions. Hence, the obtained results (images) are consistent with cellular (microstructural) details of fibre arrangement in the crystalline lens and its impact on the lens optical quality.

Secondly, SS-OCT is a modality characterised by a higher sensitivity than earlier OCT generations, so it is possible to efficiently image pseudo-transparent objects like crystalline lenses in their natural state. Lens sutures are practically invisible in healthy conditions using regular lens imaging with a slit lamp. However, clinical cases with sutural cataracts can demonstrate opaque sutures clearly distinguishable in biomicroscopic examination [27]. Therefore, OCT extends this ability into the less scattering cases, enhancing diagnostic utility. With the high scan density, 3-D OCT data also enables the implementation of different strategies to select subsets of voxels that can contrast desired structures effectively. In this study, I used voxel axial averaging to increase the signal-to-noise ratio resulting in a higher projection image quality with no significant loss of resolution.

Thirdly, the sutures are three-dimensional anatomical structures, thus requiring volumetric imaging for visualisation. Accordingly, with its low sensitivity drop with depth, SS-OCT shows the potential for effective reconstruction of the sutures' architecture. Finally, OCT can probe optical properties in a non-contact and non-invasive way. Consequently, unlike other optical methods, studies on lens sutures can be done *in-vivo*.

Clinical research on ageing lenses involving imaging modalities included the topics such as lens biometric alterations, increased scattering or loss of accommodation [9, 111, 178, 215]. I studied another aspect of the processes of eye ageing that considers the formation of sutures. I showed the types of sutures at different stages of human lens development and ageing: Y-shaped sutures in the fetal nucleus, and simple and complex star-shaped sutures as the effect of continuous division and differentiation of epithelium cells. The formation of more complex suture patterns in the crystalline lenses complies with the age-dependent structural organisation of sutures, as revealed by earlier microstructural studies [41, 217]. The discrepancy between the number of sutures detected in the anterior and posterior lens cortex could be partially attributed to the lower signal in OCT images in the posterior part of the crystalline lenses. When the numbers of sutures in the anterior and posterior parts of the crystalline lens matched, it was possible to find offset (rotation angle) between patterns [204].

A single cross-section of the crystalline lens does not allow us to reveal the architecture of sutures. It is a volumetric image that enables the generation of virtually any projection, thus providing insight into sutures. It has been shown experimentally that sutures play a role in lens aberrations [43]. However, recent studies demonstrated the possible involvement of the sutures in the circulation of nutrients and waste removal, which is crucial for lens physiology [27, 68, 128, 219]. This hypothesis might be confirmed by observing hypo-reflective zones surrounded by regular hyper-reflective lines. This unexpected optical effect could be associated with light absorption, light polarization, and extracellular spaces within fibre cells interconnection along the suture that acts as a nutrient flow channel (microcirculation). Consequently, a more detailed investigation is required for that effect.

Furthermore, the developed algorithm included the steps of skeletonisation and pruning, which were the sources of some erroneous detection of sutures (cf. Fig. 27), although the number of detected sutures correlated very well with manual detection. The shape of some sutures did not fully correspond to that observed in the periphery of the AIP image, especially in the eyes of young subjects where the OCT signal of the crystalline lens was relatively low. Suture branches were more clearly visible in older subjects due to higher scatter and better AIP image contrast.

The pupil diameter introduced a bias in the quantitative analysis of the crystalline lens sutures with respect to age. Therefore, the same diameter of the region of interest was used in this study to calculate the biomarkers. The results showed that the suture density index correlates very weakly with age only for anterior sutures and confirmed that the number of suture branches in older subjects were not significantly higher. The effect of age on suture development might be more pronounced if more young participants are included. The age-related changes in the cortical and sutural OCT signal confirm opacification processes in the crystalline lenses, which reduce their transparency [131, 149].

It is important to mention that the volumetric data were not corrected for light refraction in this part of the study. The OCT images shown in this study represent optical distances. Consequently, the effective imaging range of the posterior lens is lower than that of the anterior lens. Based on ray tracing applied to the model eye, one

can estimate that the observed transverse range of the posterior lens is ca. 12% smaller than the pupil diameter (in the anterior lens). Since the circular pupil is the physical barrier to the evaluation of the crystalline lens, the imaged area in the posterior surface of the lens is ca. 22% smaller than the pupil area. Moreover, the biomarkers introduced in this study to describe the sutures are not based on geometrical dimensions, which are affected by light refraction in the lens.

The lenticular suture development is proportional to the growth of the crystalline lens with age and highly contributes to the rising back reflected OCT signal with age. The orientation of the suture pattern and suture-associated extracellular spaces in the anterior and posterior lens is responsible for the nutrient circulation cycle. It supports homeostasis processes to maintain the transparency and flexibility of the lens (discussed in section 1.4.2).

In conclusion, optical inhomogeneities of the lens manifest in increased light scattering at the lenticular sutures. SS-OCT can detect differences in light scattering across the lens enabling visualization of suture branches. The sutures increase their complexity with age, and show elevated light scattering.



# Chapter 6

## Summary, limitations, and future scope. Conclusions

### 6.1 Summary

The research presented in this thesis concerned ageing processes in the eye. I hypothesized that optical imaging technologies enable visualization of the structural and optical changes in the crystalline lens. The main aim of the study was to demonstrate and quantify age-related alterations in the crystalline lens in cross-sectional studies in a group of healthy subjects. To verify the hypothesis and achieve the scientific goals of my PhD project, I used two modern imaging systems: anterior segment SS-OCT and retinal PSF imaging (OQAS) to assess both the lens morphology and intraocular scattering. Additionally, I employed an adaptive optics visual simulator to perform visual tests.

I concentrated on the following specific research problems that are associated with age-related effects on the crystalline lens:

- lens shape remodelling with age,
- gradual loss of lens transparency and reduction of visual performance,
- optical inhomogeneities within the lens associated with the micro-structural organization.

With respect to specific aim 1, I found that the lens becomes thicker and more convex with ageing. The cortex is primarily responsible for the increase in lens thickness. In addition, the changes in the geometry and transparency of the crystalline lens have a significant impact on the optical quality of the eye and its visual performance.

Specific aim 2 was devoted to the exploration of a characteristic three-dimensional optical non-homogenous nature of the crystalline lens. In particular, axial (depth-resolved) optical inhomogeneities detected by OCT are related to OSD zones whereas lateral optical inhomogeneities are visualized in the form of lenticular sutures. Accordingly, high-resolution cross-sectional images of the crystalline lens enable us to distinguish the lenticular OSD zones. Evaluation of light scattering in the lens demonstrates that the nucleus and C2-C4 zones contribute to the general opacification of the crystalline lens. The most significant age-related changes occur in the C3 zone as it thickens faster and becomes more opaque than other OSD zones. Additionally, contrast-enhanced averaged intensity projections reveal characteristic suture patterns that become more complex and more scattering with age. Observations of OSD zones and sutures reflect the specific organization of the fibre cells in the crystalline lens.

My research tasks included mostly the development of advanced image processing techniques for the objective and quantitative determination of the features of the ageing lens. **Those tools allowed us to add novel and innovative findings to the ophthalmic *in-vivo* studies and broadened our understanding of crystalline lens development and ageing.** In particular, I performed the first comprehensive study on the changes in the OSD zones with age using OCT, which is a more sensitive modality than standard Scheimpflug imaging. Secondly, to the best of my knowledge, I managed to report *in-vivo* observations of lenticular sutures for the first time.

The comprehensive approach to the problem of ocular ageing has important implications from the point of fundamental biology and clinical science. The results help us understand the ageing processes that often lead to presbyopia and cataract. The results can also facilitate the development of emerging strategies for cataract surgery and accommodation restoration.

## 6.2 Limitations

Although the studies presented in this dissertation address many software and hardware challenges, there are still methodological limitations regarding the application of OCT in studying age-related changes in the crystalline lens. The following factors have been identified:

1. *Spectral range of illumination in SS-OCT*: We have performed imaging at the central wavelength of 1050 nm to visualize the structure of the crystalline lens. Ideally, imaging should be performed in the visible range of electromagnetic radiation rather than in the near-infrared if one wants to quantitatively describe light scattering in the eye with realistic associations with impact on vision. However, the near-infrared spectral range used in this study can be considered as a trade-off between desired light penetration and the availability of tunable light sources on the market. Light scattering decreases with the illuminating wavelength, which allows for larger penetration depths at longer wavelengths. However, tissue imaging at 1  $\mu\text{m}$  or 1.3  $\mu\text{m}$  is limited by water absorption, and axial resolution is poorer compared with 0.84  $\mu\text{m}$  bandwidth. Although visible-light OCT was reported in the literature, the imaging depth ranges of those systems are usually limited [220]. Consequently, it is necessary to keep this in mind while comparing the optical density measured by OCT with the results from OQAS.
2. *Limited field of view. Shadowing artefact*: The crystalline lens is located behind the iris, which is a high-scattering and absorbing tissue. Therefore, the light cannot be effectively delivered to the regions of the lens which are behind the iris (outside the pupil area), and the whole lens cannot be imaged since the shadowing effect appears in OCT images. Although initial attempts have been demonstrated to increase the sampling volume of the lens they are difficult to be applied in a clinical environment [221]. This challenge of *in-vivo* imaging is usually overcome in a clinical setting by using mydriatic agents, which dilate the pupil. However, no mydriasis was applied before scanning in this study for the sake of patient comfort, and it restricted the field of view in the OCT images. In addition, the natural size of the pupil decreases with age [35, 222]. Therefore, a limited field of view could have an impact, particularly on the measurements of the radii of curvature of lenticular interfaces.
3. *Motion artefacts*: OCT images are susceptible to motion artefacts, which can occur if the patient moves during the imaging process. The eye's involuntary movements can also cause motion artefacts, which can reduce the quality of the images. This is particularly problematic when imaging the crystalline lens, as the eye's movements can cause distortions in the image and affect the accuracy of the measurements. This

limitation can be addressed by using OCT systems with faster acquisition times, which can reduce the effects of motion artefacts. Eye tracking systems can also be used to monitor the eye's movements and compensate for them during imaging. However, an increase in the scanning speed results in a drop in sensitivity, which can limit the application of the imaging system in the cases of young (relatively transparent) lenses.

4. *Refractive index distribution in the lens:* The refractive index of the lens exhibits age-related dependency [11, 12, 25]. However, no individual refractive indexes were taken into account during data post-processing since I used an equivalent refractive index for the cortex (1.3749) and nucleus (1.3947) for all processed data. This may have influenced the accuracy of morphometric measurements and influenced especially the significance of changes in the shape of the posterior lens curvature with age. This challenge could be addressed by implementing more sophisticated data processing tools [20, 166, 223].
5. *Limited resolution:* While OCT has excellent resolution, it may not be sufficient to image the fine structures within the crystalline lens, such as the lens fibres. The aspects of lens ageing associated with the development of lenticular suture architecture require much better resolution. Although I observed and mapped the sutures indirectly based on elevated light backscattering, a high-resolution microscopic technique that enables non-invasive *in-vivo* imaging of the crystalline lens would address the above-mentioned challenges.
6. *Small study sample size:* The main limitation of our study was the size of the study group. Consequently, we used non-parametric testing of the relations between the extracted parameters and age (Spearman's rank correlation test), which allowed us to infer on general tendency of changes (increase or decrease). In addition, we recruited 1 volunteer in the first decade of life and 8 teenagers. Accordingly, the limited sample size and age range did not permit to investigate interesting changes in lens thickness (e.g. remodelling and compaction), which were reported *in-vivo* and *ex-vivo* within the first 20 years after birth [3, 26, 27].

### 6.3 Future scope

The results obtained in this study open new perspectives for research actions. One area of research that is worth further exploration is the study of the relationship between age-related changes in the crystalline lens and other tissues, such as the retina and the vitreous. For example, studies have shown that age-related changes in the vitreous, such as liquefaction and posterior vitreous detachment, are associated with changes in the shape and position of the crystalline lens [133, 224]. Although it is extremely challenging to develop the imaging system for imaging through the entire eye length, such a study will offer a comprehensive and comparative approach to the problem of optical degeneration of ocular structures.

Another area of research that can benefit from the use of OCT is the study of the impact of environmental factors on the ageing processes in the crystalline lens. Environmental factors such as ultraviolet (UV) radiation, smoking, and diet have been implicated in the development of cataracts. OCT can be used to assess the degree of lens opacification and to quantify changes in lens thickness, density, and refractive index gradient in individuals with different levels of exposure to these environmental factors.

Moreover, OCT can be used to study the impact of genetics on the ageing processes in the crystalline lens. Genetic factors have been shown to play a role in the development of age-related cataracts, and OCT can be used to identify genetic markers associated with changes in lens morphology and transparency. By studying the genetic basis of age-related changes in the crystalline lens, researchers can develop new therapeutic approaches to prevent or delay the onset of cataracts.

The ability to identify and distinguish the OSD zones can be further extended for different accommodation statuses of the eye. It would be interesting to investigate the impact of accommodative demand on the geometry (e.g. thickness) of the nucleus and cortical OSD zones. That research would potentially contribute to the understanding of accommodation-related eye biomechanics and might explain fundamental issues of presbyopia development (like the age-related alterations of refractive index distribution in the lens).

Access to *in-vivo* modality that reveals suture morphology opens the gates to studying the role of nutrition cycles in maintaining the health and integrity of the lens. The nutrition cycles within the crystalline lens play an important role in maintaining the health and integrity of the lens. These cycles are responsible for delivering nutrients to the lens fibres and removing waste products, such as degraded proteins and lipids, which are facilitated by the sutures (that act as channels). Transportation processes of metabolic products are critical for maintaining the transparency and refractive index of the lens, which are essential for proper vision. Recent studies have shown that the nutrition cycles within the crystalline lens are closely related to the structure and function of the lens sutures [65-67].

Recent advances in OCT technology, such as SS-OCT and full-field OCT, hold promise for imaging the entire lens and its sutures *in-vivo*. The development of new algorithms for analysing the complex patterns of the lens sutures. The sutures form a unique and complex pattern that is specific to each individual, and analysing this pattern requires advanced image processing techniques and algorithms. Machine learning algorithms, such as deep learning, hold great potential for analysing sutural patterns and extracting meaningful information.

Furthermore, OCT can be used to monitor the efficacy of pharmacological treatments for age-related changes in the crystalline lens. Various drugs and compounds, such as aldose reductase inhibitors, have been shown to prevent or delay the onset of cataracts in animal models. OCT can be used to measure changes in lens thickness, density, and refractive index gradient in individuals undergoing treatment with these drugs, providing a non-invasive method for assessing treatment efficacy.

## **6.4 Conclusions**

In conclusion, the verification of the research hypothesis showed that SS-OCT enables volumetric visualization of the microstructure of the human crystalline lens. Double-pass imaging permits objective assessment of intraocular scattering. The progress of age-related effects on the lens shape and transparency leading to gradual visual quality reduction can be determined quantitatively from 3-D OCT data. Moreover, the unique features of OCT imaging such as volumetric scanning, high

sensitivity and high resolution facilitate the identification of optical signal discontinuity zones and lenticular sutures. The results provide an improved understanding of the development of cataracts and presbyopia.



## References

1. S. M. Salvi, S. Akhtar, and Z. Currie, "Ageing changes in the eye," *Postgrad. Med. J.* **82**, 581-587 (2006).
2. U. P. Andley, "Crystallins in the eye: Function and pathology," *Prog. Retin. Eye Res.* **26**, 78-98 (2007).
3. D. A. Atchison, E. L. Markwell, S. Kasthurirangan, J. M. Pope, G. Smith, and P. G. Swann, "Age-related changes in optical and biometric characteristics of emmetropic eyes," *J. Vis.* **8**, 1-20 (2008).
4. A. Berlin, M. E. Clark, T. A. Swain, N. A. Fischer, G. McGwin, K. R. Sloan, C. Owsley, and C. A. Curcio, "Impact of the aging lens and posterior capsular opacification on quantitative autofluorescence imaging in age-related macular degeneration," *Transl. Vis. Sci. Tech.* **11**, 23 (2022).
5. M. E. Bosem, P. A. Sample, G. A. Martinez, M. Lusky, and R. N. Weinreb, "Age-related changes in the human lens: a comparison of Scheimpflug photography and lens density index," *J. Cataract Refract. Surg.* **20**, 70-73 (1994).
6. C. Cheng, J. Parreno, R. B. Nowak, S. K. Biswas, K. Wang, M. Hoshino, K. Uesugi, N. Yagi, J. A. Moncaster, W.-K. Lo, B. Pierscionek, and V. M. Fowler, "Age-related changes in eye lens biomechanics, morphology, refractive index and transparency," *Aging* **11**, 12497-12531 (2019).
7. P. J. Donaldson, A. C. Grey, B. Maceo Heilman, J. C. Lim, and E. Vaghefi, "The physiological optics of the lens," *Prog. Retin. Eye Res.* **56**, e1-e24 (2017).
8. M. Dubbelman, and G. L. Van der Heijde, "The shape of the aging human lens: curvature, equivalent refractive index and the lens paradox," *Vis. Res.* **41**, 1867-1877 (2001).
9. M. Dubbelman, G. L. van der Heijde, H. A. Weeber, and G. F. J. M. Vrensen, "Changes in the internal structure of the human crystalline lens with age and accommodation," *Vis. Res.* **43**, 2363-2375 (2003).
10. R. C. Augusteyn, "On the growth and internal structure of the human lens," *Exp. Eye Res.* **90**, 643-654 (2010).
11. M. Bahrami, M. Hoshino, B. Pierscionek, N. Yagi, J. Regini, and K. Uesugi, "Optical properties of the lens: an explanation for the zones of discontinuity," *Exp. Eye Res.* **124**, 93-99 (2014).
12. J. F. Koretz, C. A. Cook, and J. R. Kuszak, "The zones of discontinuity in the human lens: development and distribution with age," *Vis. Res.* **34**, 2955-2962 (1994).
13. J. R. Kuszak, R. K. Zoltoski, and C. E. Tiedemann, "Development of lens sutures," *Int. J. Dev. Biol.* **48**, 889-902 (2004).

14. A. Gupta, D. Ruminski, A. Jimenez Villar, R. Duarte Toledo, S. Manzanera, S. Panezai, J. Mompean, P. Artal, and I. Grulkowski, "In vivo SS-OCT imaging of crystalline lens sutures," *Biomed. Opt. Express* **11**, 5388-5400 (2020).
15. P. Artal, ed. *Handbook of Visual Optics, Volume One : Fundamentals and Eye Optics*, (CRC Press, 2017).
16. D. A. Atchison, and G. Smith, "Chromatic dispersions of the ocular media of human eyes," *J. Opt. Soc. Am. A* **22**, 29-37 (2005).
17. S. Bassnett, Y. Shi, and G. F. J. M. Vrensen, "Biological glass: structural determinants of eye lens transparency," *Phil. Trans. Royal Soc. B: Bio. Sci.* **366**, 1250-1264 (2011).
18. S. P. Bhat, "Crystallins, genes and cataract," in *Progress in Drug Research*, E. Jucker, ed., Birkhäuser. **60**, 205-262, (2003).
19. R. C. Augusteyn, "Growth of the lens: *in vitro* observations," *Clin. Exp. Optom.* **91**, 226-239 (2008).
20. A. de Castro, S. Ortiz, E. Gamba, D. Siedlecki, and S. Marcos, "Three-dimensional reconstruction of the crystalline lens gradient index distribution from OCT imaging," *Opt. Express* **18**, 21905-21917 (2010).
21. B. K. Pierscionek, and J. W. Regini, "The gradient index lens of the eye: an opto-biological synchrony," *Prog. Retin. Eye Res.* **31**, 332-349 (2012).
22. R. C. Augusteyn, C. E. Jones, and J. M. Pope, "Age-related development of a refractive index plateau in the human lens: evidence for a distinct nucleus," *Clin. Exp. Optom.* **91**, 296-301 (2008).
23. A. P. Arrigo, and S. Simon, "Expression and functions of heat shock proteins in the normal and pathological mammalian eye," *Curr. Mol. Med.* **10**, 776-793 (2010).
24. H. Bloemendal, W. de Jong, R. Jaenicke, N. H. Lubsen, C. Slingsby, and A. Tardieu, "Ageing and vision: structure, stability and function of lens crystallins," *Prog. Biophys. Mol. Biol.* **86**, 407-485 (2004).
25. L. S. Kwok, and M. T. Coroneo, "Temporal and spatial growth patterns in the normal and cataractous human lens," *Exp. Eye Res.* **71**, 317-322 (2000).
26. J. G. Sivak, K. L. Herbert, K. L. Peterson, and J. R. Kuszak, "The interrelationship of lens anatomy and optical quality. I. Non-primate lenses," *Exp. Eye Res.* **59**, 505-520 (1994).
27. H. D. Wu, L. A. Howse, and E. Vaghefi, "Effect of Age-Related Human Lens Sutures Growth on Its Fluid Dynamics," *Invest. Ophthalmol. Vis. Sci.* **58**, 6351-6357 (2017).
28. N. A. Brown, A. J. Bron, and J. M. Sparrow, "An estimate of the size and shape of the human lens fibre *in vivo*," *Br. J. Ophthalmol.* **71**, 916-922 (1987).
29. V. I. Shestopalov, and S. Bassnett, "Three-dimensional organization of primary lens fiber cells," *Invest. Ophthalmol. Vis. Sci.* **41**, 859-863 (2000).
30. P. Artal, "Optics of the eye and its impact in vision: a tutorial," *Adv. Opt. Photon.* **6**, 340-367 (2014).
31. F. A. Bettelheim, and L. T. Chylack, "Light scattering of whole excised human cataractous lenses. Relationships between different light scattering parameters," *Exp. Eye Res.* **41**, 19-30 (1985).

32. C. Beckman, O. Nilsson, and L.-E. Paulsson, "Intraocular light scattering in vision, artistic painting, and photography," *App. Opt.* **33**, 4749-4753 (1994).
33. F. A. Bettelheim, and S. Ali, "Light scattering of normal human lens. III. Relationship between forward and back scatter of whole excised lenses," *Exp. Eye Res.* **41**, 1-9 (1985).
34. R. S. Anderson, T. Redmond, D. R. McDowell, K. M. Breslin, and M. B. Zlatkova, "The robustness of various forms of perimetry to different levels of induced intraocular stray light," *Invest. Ophthalmol. Vis. Sci.* **50**, 4022-4028 (2009).
35. M. L. Hennelly, J. L. Barbur, D. F. Edgar, and E. G. Woodward, "The effect of age on the light scattering characteristics of the eye," *Ophthalmic Physiol. Opt* **18**, 197-203 (1998).
36. M. J. Costello, S. Johnsen, K. O. Gilliland, C. D. Freeland, and W. C. Fowler, "Predicted light scattering from particles observed in human age-related nuclear cataracts using mie scattering theory," *Invest Ophthalmol Vis Sci* **48**, 303-312 (2007).
37. T. J. van den Berg, "Light scattering by donor lenses as a function of depth and wavelength," *Invest. Ophthalmol. Vis. Sci.* **38**, 1321-1332 (1997).
38. S. Lerman, "An experimental and clinical evaluation of lens transparency and aging," *J. Gerontol.* **38**, 293-301 (1983).
39. T. J. van den Berg, "Analysis of intraocular straylight, especially in relation to age," *Optom. Vis. Sci.* **72**, 52-59 (1995).
40. J. R. Kuszak, B. A. Bertram, M. S. Macsai, and J. L. Rae, "Sutures of the Crystalline Lens: A Review," *Scan. Electron Microsc.* **III**, 1369-1378 (1984).
41. J. R. Kuszak, R. K. Zoltoski, and C. E. Tiedemann, "Development of lens sutures," *Int. J. Dev. Biol.* **48**, 889-902 (2004).
42. J. R. Kuszak, K. L. Peterson, J. G. Sivak, and K. L. Herbert, "The interrelationship of lens anatomy and optical quality. II. Primate lenses," *Exp. Eye Res.* **59**, 521-535 (1994).
43. A. Gargallo, J. Arines, and E. Acosta, "Lens aberrations and their relationship with lens sutures for species with Y-suture branches," *J. Biomed. Opt.* **18**, 025003 (2013).
44. B. A. Moffat, D. A. Atchison, and J. M. Pope, "Explanation of the lens paradox," *Optom. Vis. Sci.* **79**, 148-150 (2002).
45. B. A. Moffat, D. A. Atchison, and J. M. Pope, "Age-related changes in refractive index distribution and power of the human lens as measured by magnetic resonance micro-imaging *in vitro*," *Vis. Res.* **42**, 1683-1693 (2002).
46. M. Dubbelman, and G. L. Van der Heijde, "The shape of the aging human lens: curvature, equivalent refractive index and the lens paradox," *Vis. Res.* **41**, 1867-1877 (2001).
47. "Wiring Diagram Eye Pattern Drawing - Part Of The Eye Clip Art, [https://www.nicepng.com/ourpic/u2w7q8t4u2y3u2\\_wiring-diagram-eye-pattern-drawing-part-of-the/](https://www.nicepng.com/ourpic/u2w7q8t4u2y3u2_wiring-diagram-eye-pattern-drawing-part-of-the/)."
48. M. Dubbelman, G. L. van der Heijde, and H. A. Weeber, "Change in shape of the aging human crystalline lens with accommodation," *Vis. Res.* **45**, 117-132 (2005).
49. B. A. Lege, W. Haigis, T. F. Neuhann, and M. H. Bauer, "Age-related behavior of posterior chamber lenses in myopic phakic eyes during accommodation measured by anterior segment partial coherence interferometry," *J. Cataract Refract. Surg.* **32**, 999-1006 (2006).

50. A. Khurana, *Comprehensive Ophthalmology* (New Age International Publishers, 2018).
51. N. Azzam, and A. Dovrat, "Long-term lens organ culture system to determine age-related effects of UV irradiation on the eye lens," *Exp. Eye Res.* **79**, 903-911 (2004).
52. J. Dillon, L. Zheng, J. C. Merriam, and E. R. Gaillard, "The optical properties of the anterior segment of the eye: implications for cortical cataract," *Exp. Eye Res.* **68**, 785-795 (1999).
53. C. A. McCarty, and H. R. Taylor, "A review of the epidemiologic evidence linking ultraviolet radiation and cataracts," *Dev. Ophthalmol.* **35**, 21-31.
54. H. R. Taylor, S. K. West, F. S. Rosenthal, B. Muñoz, H. S. Newland, H. Abbey, and E. A. Emmett, "Effect of ultraviolet radiation on cataract formation," *N. Engl. J. Med.* **319**, 1429-1433.
55. B. A. Moffat, K. A. Landman, R. J. Truscott, M. H. Sweeney, and J. M. Pope, "Age-related changes in the kinetics of water transport in normal human lenses," *Exp. Eye Res.* **69**, 663-669 (1999).
56. Z. Micun, M. Falkowska, M. Młynarczyk, J. Kochanowicz, K. Socha, and J. Konopińska, "Levels of trace elements in the lens, aqueous humour, and plasma of cataractous patients-A narrative review," *Int. J. Environ. Res. Public Health.* **19** (2022).
57. J. F. Koretz, P. L. Kaufman, M. W. Neider, and P. A. Goeckner, "Accommodation and presbyopia in the human eye--aging of the anterior segment," *Vis. Res.* **29**, 1685-1692 (1989).
58. M. Yanoff, and J. S. Duker, eds., *Ophthalmology*, (Elsevier, 2004).
59. D. C. Beebe, "Maintaining transparency: a review of the developmental physiology and pathophysiology of two avascular tissues," *Semin. Cell Dev. Biol.* **19**, 125-133 (2008).
60. N. J. Zar, and E. A. Davis, "Embryology in the eye," in *Ophthalmology*, M. Yanoff, and J. S. Duker, eds., (Elsevier, 2004).
61. "Embryology / pathology, <https://clinicalgate.com/embryology-pathology/>,".
62. M. A. Babizhayev, "New concept in nutrition for the maintenance of the aging eye redox regulation and therapeutic treatment of cataract disease; synergism of natural antioxidant imidazole-containing amino acid-based compounds, chaperone, and glutathione boosting agents: a systemic perspective on aging and longevity emerged from studies in humans," *Am. J. Ther.* **17**, 373-389 (2010).
63. D. C. Beebe, "Nuclear cataracts and nutrition: hope for intervention early and late in life," *Invest. Ophthalmol. Vis. Sci.* **39**, 1531-1534 (1998).
64. N. A. Delamere, M. Shahidullah, R. T. Mathias, J. Gao, X. Sun, C. Sellitto, and T. W. White, "Signaling between TRPV1/TRPV4 and intracellular hydrostatic pressure in the mouse lens," *Invest. Ophthalmol. Vis. Sci.* **61**, 58 (2020).
65. P. Donaldson, J. Kistler, and R. T. Mathias, "Molecular solutions to mammalian lens transparency," *Physiology* **16**, 118-123 (2001).
66. J. Gao, P. J. Minogue, E. C. Beyer, R. T. Mathias, and V. M. Berthoud, "Disruption of the lens circulation causes calcium accumulation and precipitates in connexin mutant mice," *Am. J. Physiol. Cell Physiol.* **314**, C492-C503 (2018).
67. K. L. Schey, R. S. Petrova, R. B. Gletten, and P. J. Donaldson, "The role of aquaporins in ocular lens homeostasis," *Int. J. Mol. Sci.* **18** (2017).

68. S. Amano, Y. Amano, S. Yamagami, T. Miyai, K. Miyata, T. Samejima, and T. Oshika, "Age-related changes in corneal and ocular higher-order wavefront aberrations," *Am. J. Ophthalmol.* **137**, 988-992 (2004).
69. H. V. Athaide, M. Campos, and C. Costa, "Study of ocular aberrations with age," *Arq. Bras. Oftalmol.* **72**, 617-621 (2009).
70. J. Dillon, L. Zheng, J. C. Merriam, and E. R. Gaillard, "Transmission of light to the aging human retina: possible implications for age related macular degeneration," *Exp. Eye Res.* **79**, 753-759 (2004).
71. W. Hodos, R. F. Miller, and K. V. Fite, "Age-dependent changes in visual acuity and retinal morphology in pigeons," *Vision Res.* **31**, 669-677 (1991).
72. K. Barton, and R. A. Hitchings, *Medical management of glaucoma* (Springer, 2013).
73. P. L. Kaufman, and L. Z. Bito, "The occurrence of senile cataracts, ocular hypertension and glaucoma in rhesus monkeys," *Exp. Eye Res.* **34**, 287-291 (1982).
74. S. N. Markowitz, and J. D. Morin, "Angle-closure glaucoma: relation between lens thickness, anterior chamber depth and age," *Can. J. Ophthalmol.* **19**, 300-302 (1984).
75. D. Papaconstantinou, I. Georgalas, N. Kourtis, A. Krassas, A. Diagourtas, C. Koutsandrea, and G. Georgopoulos, "Lens-induced glaucoma in the elderly," *Clin. Interv. Aging* **4**, 331-336 (2009).
76. H. Yang, and N. A. Afshari, "The yellow intraocular lens and the natural ageing lens," *Curr. Opin. Ophthalmol.* **25**, 40-43 (2014).
77. R. Navarro, F. Palos, and L. M. González, "Adaptive model of the gradient index of the human lens. II. Optics of the accommodating aging lens," *J. Opt. Soc. Am. A. Opt. Image Sci. Vis* **24**, 2911-2920 (2007).
78. N. J. Ray, "Biophysical chemistry of the ageing eye lens," *Biophys Rev* **7**, 353-368 (2015).
79. M. V. Cicinelli, J. C. Buchan, M. Nicholson, V. Varadaraj, and R. C. Khanna, "Cataracts," *Lancet* **401**, 377-389 (2023).
80. A. J. Bron, G. F. Vrensen, J. Koretz, G. Maraini, and J. J. Harding, "The ageing lens," *Ophthalmologica* **214**, 86-104 (2000).
81. A. Shiels, and J. F. Hejtmancik, "Genetic origins of cataract," *Arch. Ophthalmol.* **125**, 165-173.
82. J. Graw, "Genetics of crystallins: cataract and beyond," *Exp. Eye Res.* **88**, 173-189.
83. A. Shiels, and J. F. Hejtmancik, "Mutations and mechanisms in congenital and age-related cataracts," *Exp. Eye Res.* **156**, 95-102 (2017).
84. G. Aragonès, K. Dasuri, O. Olukorede, S. G. Francisco, C. Renneburg, C. Kumsta, M. Hansen, S. Kageyama, M. Komatsu, S. Rowan, J. Volkin, M. Workman, W. Yang, P. Daza, D. Ruano, H. Dominguez-Martín, J. A. Rodríguez-Navarro, X. L. Du, M. A. Brownlee, E. Bejarano, and A. Taylor, "Autophagic receptor p62 protects against glycation-derived toxicity and enhances viability," *Aging Cell* **19**, e13257 (2020).
85. A. J. Bron, N. A. Brown, J. J. Harding, and E. Ganea, "The lens and cataract in diabetes," *Int. Ophthalmol. Clin.* **38**, 37-67 (1998).

86. L. Kessel, T. Jørgensen, C. Glümer, and M. Larsen, "Early lens aging is accelerated in subjects with a high risk of ischemic heart disease: an epidemiologic study," *BMC Ophthalmol.* **6**, 16 (2006).
87. W. G. Christen, J. E. Manson, J. M. Seddon, R. J. Glynn, J. E. Buring, B. Rosner, and C. H. Hennekens, "A prospective study of cigarette smoking and risk of cataract in men," *JAMA* **268**, 989-993.
88. B. R. Hammond, B. R. Wooten, J. E. Náñez, and A. J. Wenzel, "Smoking and lens optical density," *Ophthalmic. Physiol. Opt.* **19**, 300-305 (1999).
89. A. Langford-Smith, V. Tilakaratna, P. R. Lythgoe, S. J. Clark, P. N. Bishop, and A. J. Day, "Age and smoking related changes in metal ion levels in human lens: Implications for cataract formation," *PLOS ONE* **11**, e0147576 (2016).
90. I. D. Nicholl, and R. Bucala, "Advanced glycation endproducts and cigarette smoking," *Cell Mol. Biol.* **44**, 1025-1033 (1998).
91. J. Zhang, H. Yan, S. Löfgren, X. Tian, and M. F. Lou, "Ultraviolet radiation-induced cataract in mice: the effect of age and the potential biochemical mechanism," *Invest. Ophthalmol. Vis. Sci.* **53**, 7276-7285 (2012).
92. F. Kamari, S. Hallaj, F. Dorosti, F. Alinezhad, N. Taleschian-Tabrizi, F. Farhadi, and H. Aslani, "Phototoxicity of environmental radiations in human lens: revisiting the pathogenesis of UV-induced cataract," *Graefes Arch. Clin. Exp. Ophthalmol.* **257**, 2065-2077 (2019).
93. F. J. Giblin, L. R. Lin, M. F. Simpanya, V. R. Leverenz, and C. E. Fick, "A Class I UV-blocking (senofilcon A) soft contact lens prevents UVA-induced yellow fluorescence and NADH loss in the rabbit lens nucleus in vivo," *Exp. Eye Res.* **102**, 17-27 (2012).
94. F. Behar-Cohen, G. Baillet, T. de Aiguavives, P. O. Garcia, J. Krutmann, P. Peña-García, C. Reme, and J. S. Wolffsohn, "Ultraviolet damage to the eye revisited: eye-sun protection factor (E-SPF®), a new ultraviolet protection label for eyewear," *Clin. Ophthalmol.* **8**, 87-104 (2014).
95. P. F. Jacques, A. Taylor, S. Moeller, S. E. Hankinson, G. Rogers, W. Tung, J. Ludovico, W. C. Willett, and L. T. Chylack, "Long-term nutrient intake and 5-year change in nuclear lens opacities," *Arch. Ophthalmol.* **123**, 517-526 (2005).
96. A. Astorino, and Jr, "Cataracts, <https://www.astorinoeyecare.com/blog/ataracts.>"
97. "Cataract surgery, <https://pgheyemds.com/our-services/ataract-surgery/>,".
98. P. Artal, ed., *Handbook of Visual Optics, Volume Two : Instrumentation and Vision Correction*, (CRC Press, 2017).
99. T. Kohnen, M. Baumeister, D. Kook, O. K. Klaproth, and C. Ohrloff, "Cataract surgery with implantation of an artificial lens," *Dtsch Arztebl Int* **106**, 695-702 (2009).
100. R. N. Mercer, C. M. Milliken, G. O. Waring, and K. M. Rocha, "Future trends in presbyopia correction," *J. Refract. Surg.* **37**, S28-S34 (2021).
101. E. Berrio, J. Tabernero, and P. Artal, "Optical aberrations and alignment of the eye with age," *J. Vis.* **10** (2010).
102. "Presbyopia, <https://www.mayoclinic.org/diseases-conditions/presbyopia/multimedia/inside-your-eye/img-20008042>," .

103. K. R. Heys, M. G. Friedrich, and R. J. Truscott, "Presbyopia and heat: changes associated with aging of the human lens suggest a functional role for the small heat shock protein, alpha-crystallin, in maintaining lens flexibility," *Aging Cell* **6**, 807-815 (2007).
104. E. Lafosse, J. S. Wolffsohn, C. Talens-Estarellles, and S. García-Lázaro, "Presbyopia and the aging eye: Existing refractive approaches and their potential impact on dry eye signs and symptoms," *Cont. Lens Anterior, Eye* **43**, 103-114 (2020).
105. J. S. Wolffsohn, and L. N. Davies, "Presbyopia: Effectiveness of correction strategies," *Prog. Retin. Eye Res.* **68**, 124-143 (2019).
106. A. Vogt, *Das Farbenschildern des hinteren Linsenbildes* (Klin. Monbl. Augenheilkd, 1919).
107. A. Vogt, *Lehrbuch und Atlas der Spaltlampenmikroskopie des Lebenden Auges* (Springer, 1931).
108. J. M. Sparrow, A. J. Bron, N. A. P. Brown, W. Ayliffe, and A. R. Hill, "The Oxford clinical cataract classification and grading system," *Inter. Ophthalmol.* **9**, 207-225 (1986).
109. B. Thylefors, L. T. Chylack Jr, K. Konyama, K. Sasaki, R. Sperduto, H. R. Taylor, and S. West, "A simplified cataract grading system The WHO Cataract Grading Group," *Ophth. Epidemiol.* **9**, 83-95 (2002).
110. A. J. Bron, G. F. J. M. Vrensen, J. Koretz, G. Maraini, and J. J. Harding, "The Ageing Lens," *Ophthalmologica* **214**, 86-104 (2000).
111. C. Cheng, J. Parreno, R. B. Nowak, S. K. Biswas, K. Wang, M. Hoshino, K. Uesugi, N. Yagi, J. A. Moncaster, W. K. Lo, B. Pierscionek, and V. M. Fowler, "Age-related changes in eye lens biomechanics, morphology, refractive index and transparency," *Aging* **11**, 12497-12531 (2019).
112. V. L. Taylor, K. J. al-Ghoul, C. W. Lane, V. A. Davis, J. R. Kuszak, and M. J. Costello, "Morphology of the normal human lens," *Invest. Ophthalmol. Vis. Sci.* **37**, 1396-1410 (1996).
113. R. C. Augusteyn, B. Maceo Heilman, A. Ho, and J. M. Parel, "Nonhuman primate ocular biometry," *Invest. Ophthalmol. Vis. Sci.* **57**, 105-114 (2016).
114. I. Grulkowski, S. Manzanera, L. Cwiklinski, F. Sobczuk, K. Karnowski, and P. Artal, "Swept source optical coherence tomography and tunable lens technology for comprehensive imaging and biometry of the whole eye," *Optica* **5**, 52-59 (2018).
115. E. J. Fernández, S. Manzanera, P. Piers, and P. Artal, "Adaptive Optics Visual Simulator," *J. Refract. Surg.* **18**, S634-S638 (2002).
116. P. Artal, A. Benito, G. M. Pérez, E. Alcón, Á. De Casas, J. Pujol, and J. M. Marín, "An objective scatter index based on double-pass retinal images of a point source to classify cataracts," *PLOS ONE* **6**, e16823 (2011).
117. J. L. Güell, J. Pujol, M. Arjona, F. Diaz-Douton, and P. Artal, "Optical Quality Analysis System: Instrument for objective clinical evaluation of ocular optical quality," *J. Cataract Refract. Surg.* **30**, 1598-1599 (2004).
118. K. Kamiya, K. Umeda, H. Kobashi, K. Shimizu, T. Kawamorita, and H. Uozato, "Effect of aging on optical quality and intraocular scattering using the double-pass instrument," *Curr. Eye Res.* **37**, 884-888 (2012).

119. R. R. Krueger, R. A. Applegate, and S. MacRae, *Wavefront customized visual corrections : the quest for super vision II* (SLACK, 2004).
120. S. A. Strenk, J. L. Semmlow, L. M. Strenk, P. Munoz, J. Gronlund-Jacob, and J. K. DeMarco, "Age-related changes in human ciliary muscle and lens: a magnetic resonance imaging study," *Invest Ophthalmol. Vis. Sci.* **40**, 1162-1169 (1999).
121. C. E. Jones, D. A. Atchison, and J. M. Pope, "Changes in lens dimensions and refractive index with age and accommodation," *Optom. Vis. Sci.* **84**, 990-995 (2007).
122. M. R. Praveen, A. R. Vasavada, S. K. Shah, C. B. Shah, U. P. Patel, N. V. Dixit, and S. Rawal, "Lens thickness of Indian eyes: impact of isolated lens opacity, age, axial length, and influence on anterior chamber depth," *Eye* **23**, 1542-1548 (2009).
123. H. Zhou, H. Yan, W. Yan, X. Wang, and Q. Li, "In vivo ultrasound elastographic evaluation of the age-related change of human lens nuclear stiffness," *BMC Ophthalmol.* **20**, 135 (2020).
124. C. A. Cook, J. F. Koretz, A. Pfahnl, J. Hyun, and P. L. Kaufman, "Aging of the human crystalline lens and anterior segment," *Vis. Res.* **34**, 2945-2954 (1994).
125. M. Dubbelman, G. L. Van Der Heijde, Weeber, and H. A., "The thickness of the aging human lens obtained from corrected Scheimpflug images," *Optomet. and Vis. Sci.* **78**, 411-416 (2001).
126. N. Brown, "The change in lens curvature with age," *Exp. Eye Res.* **19**, 175-183 (1974).
127. U. Eckerskorn, K. Kokkas, O. Hockwin, H. Laser, and M. Janke, "Physiologic changes of lens transparency during ageing: a Scheimpflug photography study," *Dev. Ophthalmol.* **17**, 72-74 (1989).
128. E. Vaghefi, K. Walker, B. P. Pontre, M. D. Jacobs, and P. J. Donaldson, "Magnetic resonance and confocal imaging of solute penetration into the lens reveals a zone of restricted extracellular space diffusion," *Am. J. Physiol. Regul. Integr. Comp. Physiol.* **302**, R1250-R1259 (2012).
129. T. Eto, P. Teikari, R. P. Najjar, Y. Nishimura, Y. Motomura, M. Kuze, and S. Higuchi, "A Purkinje image-based system for an assessment of the density and transmittance spectra of the human crystalline lens in vivo," *Sci. Rep.* **10**, 16445 (2020).
130. I. Grulkowski, J. J. Liu, B. Potsaid, V. Jayaraman, J. Jiang, J. G. Fujimoto, and A. E. Cable, "High-precision, high-accuracy ultralong-range swept-source optical coherence tomography using vertical cavity surface emitting laser light source," *Opt. Lett.* **38**, 673-675 (2013).
131. I. Grulkowski, S. Manzanera, L. Cwiklinski, J. Mompeán, A. de Castro, J. M. Marin, and P. Artal, "Volumetric macro- and micro-scale assessment of crystalline lens opacities in cataract patients using long-depth-range swept source optical coherence tomography," *Biomed. Opt. Express* **9**, 3821-3833 (2018).
132. J. J. Liu, I. Grulkowski, M. F. Kraus, B. Potsaid, C. D. Lu, B. Baumann, J. S. Duker, J. Hornegger, and J. G. Fujimoto, "In vivo imaging of the rodent eye with swept source/Fourier domain OCT," *Biomed. Opt. Express* **4**, 351-363 (2013).
133. D. Ruminski, J. Sebag, R. D. Toledo, A. Jiménez-Villar, J. K. Nowak, S. Manzanera, P. Artal, and I. Grulkowski, "Volumetric optical imaging and quantitative analysis of age-related changes in anterior human vitreous," *Invest. Ophthalmol. Vis. Sci.* **62**, 31 (2021).

134. J. Taberero, C. Otero, and S. Pardhan, "A comparison between refraction from an adaptive optics visual simulator and clinical refractions," *Translat. Vis. Sci. & Tech.* **9**, 23 (2020).
135. W. Drexler, and J. G. Fujimoto, eds., *Optical coherence tomography: Technology and applications* (Springer, 2015).
136. J. A. Izatt, M. R. Hee, G. M. Owen, E. A. Swanson, and J. G. Fujimoto, "Optical coherence microscopy in scattering media," *Opt. Lett.* **19**, 590-592.
137. A. F. Fercher, W. Drexler, C. K. Hitzenberger, and T. Lasser, "Optical coherence tomography - principles and applications," *Rep. Prog. Phys.* **66**, 239-303.
138. D. Huang, E. A. Swanson, C. P. Lin, J. S. Schuman, W. G. Stinson, W. Chang, M. R. Hee, T. Flotte, K. Gregory, and C. A. Puliafito, "Optical coherence tomography," *Science* **254**, 1178-1181.
139. R. Leitgeb, C. Hitzenberger, and A. Fercher, "Performance of fourier domain vs. time domain optical coherence tomography," *Opt. Express* **11**, 889-894 (2003).
140. I. Grulkowski, J. J. Liu, B. Potsaid, V. Jayaraman, C. D. Lu, J. Jiang, A. E. Cable, J. S. Duker, and J. G. Fujimoto, "Retinal, anterior segment and full eye imaging using ultrahigh speed swept source OCT with vertical-cavity surface emitting lasers," *Biomed. Opt. Express* **3**, 2733-2751 (2012).
141. I. Grulkowski, J. J. Liu, B. Potsaid, V. Jayaraman, A. E. Cable, and J. G. Fujimoto, "Ultrahigh Speed OCT," in *Optical Coherence Tomography: Technology and Applications*, W. Drexler, and J. G. Fujimoto, eds. (Springer, 2015), 319-356.
142. M. Wojtkowski, V. Srinivasan, T. Ko, J. Fujimoto, A. Kowalczyk, and J. Duker, "Ultrahigh-resolution, high-speed, Fourier domain optical coherence tomography and methods for dispersion compensation," *Opt. Express* **12**, 2404-2422 (2004).
143. J. M. Schmitt, "Optical coherence tomography (OCT): a review," *IEEE J. Sel. Top. Quant. Elect.* **5**, 1205-1215.
144. R. Huber, M. Wojtkowski, K. Taira, J. G. Fujimoto, and K. Hsu, "Amplified, frequency swept lasers for frequency domain reflectometry and OCT imaging: design and scaling principles," *Opt. Express* **13**, 3513-3528 (2005).
145. D. C. Flanders, "Short cavity tunable laser with mode position compensation," in *US Patent WO/2002/035667* (2002).
146. A. Agrawal, T. J. Pfefer, P. D. Woolliams, P. H. Tomlins, and G. Nehmetallah, "Methods to assess sensitivity of optical coherence tomography systems," *Biomed. Opt. Express* **8**, 902-917 (2017).
147. B. Potsaid, B. Baumann, D. Huang, S. Barry, A. E. Cable, J. S. Schuman, J. S. Duker, and J. G. Fujimoto, "Ultrahigh speed 1050nm swept source / Fourier domain OCT retinal and anterior segment imaging at 100,000 to 400,000 axial scans per second," *Opt. Express* **18**, 20029-20048 (2010).
148. M. Ruggeri, Y.-C. Chang, G. M. Mesquita, G. Belloni, S. Williams, A. Ho, J.-M. A. Parel, and F. Manns, "High-speed imaging and biometry of human accommodation dynamics with SS-OCT," *Invest. Ophthalmol. Vis. Sci.* **61**, 5136-5136 (2020).

149. A. de Castro, A. Benito, S. Manzanera, J. Mompeán, B. Cañizares, D. Martínez, J. M. Marín, I. Grulkowski, and P. Artal, "Three-Dimensional Cataract Crystalline Lens Imaging With Swept-Source Optical Coherence Tomography," *Invest. Ophthalmol. Vis. Sci.* **59**, 897-903 (2018).
150. I. Grulkowski, J. J. Liu, B. Potsaid, V. Jayaraman, J. Jiang, J. G. Fujimoto, and A. E. Cable, "High-precision, high-accuracy ultralong-range swept-source optical coherence tomography using vertical cavity surface emitting laser light source," *Opt. Lett.* **38**, 673-675.
151. A. F. Fercher, C. K. Hitzenberger, M. Sticker, R. Zawadzki, B. Karamata, and T. Lasser, "Numerical dispersion compensation for Partial Coherence Interferometry and Optical Coherence Tomography," *Opt. Express* **9**, 610-615 (2001).
152. A. F. Fercher, C. K. Hitzenberger, M. Sticker, R. Zawadzki, B. Karamata, and T. Lasser, "Dispersion compensation for optical coherence tomography depth-scan signals by a numerical technique," *Opt. Commun.* **204**, 67-74 (2002).
153. Y. Wang, X. Chen, X. Chen, and D. Yu, "Dispersion compensation for FD-OCT using spectrum reconstruction," *J. Xray Sci. Technol.* **23**, 639-646 (2015).
154. B. Liu, E. A. Macdonald, D. L. Stamper, and M. E. Brezinski, "Group velocity dispersion effects with water and lipid in 1.3  $\mu\text{m}$  optical coherence tomography system," *Phys. Med. Biol.* **49**, 923-930 (2004).
155. G. Ni, J. Zhang, L. Liu, X. Wang, X. Du, J. Liu, and Y. Liu, "Detection and compensation of dispersion mismatch for frequency-domain optical coherence tomography based on A-scan's spectrogram," *Opt. Express* **28**, 19229-19241 (2020).
156. D. L. Marks, A. L. Oldenburg, J. J. Reynolds, and S. A. Boppart, "Autofocus algorithm for dispersion correction in optical coherence tomography," *Appl. Opt.* **42**, 3038-3046 (2003).
157. D. L. Marks, A. L. Oldenburg, J. J. Reynolds, and S. A. Boppart, "Digital algorithm for dispersion correction in optical coherence tomography for homogeneous and stratified media," *Appl. Opt.* **42**, 204-217 (2003).
158. M. J. Simpson, "Optical quality of intraocular lenses," *J. Cataract Refract. Surg.* **18**, 86-94.
159. S. Marcos, P. Artal, D. A. Atchison, K. Hampson, R. Legras, L. Lundström, and G. Yoon, "Adaptive optics visual simulators: a review of recent optical designs and applications [Invited]," *Biomed. Opt. Express* **13**, 6508-6532 (2022).
160. S. Marcos, "Aberrometry: basic science and clinical applications," *Bull. Soc. Belge. Ophthalmol.* **302**, 197-213 (2006).
161. J. R. Kuszak, K. L. Peterson, J. G. Sivak, and K. L. Herbert, "The interrelationship of lens anatomy and optical quality II. Primate Lenses," *Exp. Eye Res.* **59**, 521-535 (1994).
162. J. R. Kuszak, "The ultrastructure of epithelial and fiber cells in the crystalline lens," *Int. Rev. Cytol.* **163**, 305-350 (1995).
163. J. G. Sivak, K. L. Herbert, K. L. Peterson, and J. R. Kuszak, "The interrelationship of lens anatomy and optical quality I. Non-primate Lenses," *Exp. Eye Res.* **59**, 505-520 (1994).
164. M. Dubbelman, G. L. Van der Heijde, H. A. Weeber, and G. F. Vrensen, "Changes in the internal structure of the human crystalline lens with age and accommodation," *Vis. Res.* **43**, 2363-2375 (2003).

165. K. Richdale, M. A. Bullimore, and K. Zadnik, "Lens thickness with age and accommodation by optical coherence tomography," *Ophthalmic Physiol. Opt.* **28**, 441-447 (2008).
166. Y.-C. Chang, G. M. Mesquita, S. Williams, G. Gregori, F. Cabot, A. Ho, M. Ruggeri, S. H. Yoo, J.-M. Parel, and F. Manns, "In vivo measurement of the human crystalline lens equivalent refractive index using extended-depth OCT," *Biomed. Opt. Express* **10**, 411-422 (2019).
167. T. J. Van Den Berg, L. J. Van Rijn, R. Michael, C. Heine, T. Coeckelbergh, C. Nischler, H. Wilhelm, G. Grabner, M. Emesz, R. I. Barraquer, J. E. Coppens, and L. Franssen, "Straylight effects with aging and lens extraction," *Am. J. Ophthalmol.* **144**, 358-363 (2007).
168. Y.-H. Wang, J. Zhong, and X.-M. Li, "Age-related changes of lens thickness and density in different age phases," *Int. J. Ophthalmol.* **15**, 1591-1597 (2022).
169. Y. Xin, and X. G. Su, *Linear regression analysis - theory and computing* (World Scientific Publishing, 2009).
170. J. L. Alió, P. Schimchak, H. P. Negri, and R. Montés-Micó, "Crystalline lens optical dysfunction through aging," *Ophthalmology* **112**, 2022-2029 (2005).
171. D. A. Atchison, E. L. Markwell, S. Kasthurirangan, J. M. Pope, G. Smith, and P. G. Swann, "Age-related changes in optical and biometric characteristics of emmetropic eyes," *J. Vis.* **8**, 29-29 (2008).
172. S. Kasthurirangan, E. L. Markwell, D. A. Atchison, and J. M. Pope, "In vivo study of changes in refractive index distribution in the human crystalline lens with age and accommodation," *Invest. Ophthalmol. Vis. Sci.* **49**, 2531-2540 (2008).
173. S. Kasthurirangan, E. L. Markwell, D. A. Atchison, and J. M. Pope, "MRI study of the changes in crystalline lens shape with accommodation and aging in humans," *J. Vis.* **11** (2011).
174. J. F. Koretz, S. A. Strenk, L. M. Strenk, and J. L. Semmlow, "Scheimpflug and high-resolution magnetic resonance imaging of the anterior segment: a comparative study," *J. Opt. Soc. Am. A* **21**, 346-354 (2004).
175. K. Kashima, B. L. Trus, M. Unser, P. A. Edwards, and M. B. Datiles, "Aging studies on normal lens using the Scheimpflug slit-lamp camera," *Invest. Ophthalmol. Vis. Sci.* **34**, 263-269 (1993).
176. Z. Li, W. Qu, J. Huang, Z. Meng, X. Li, R. Zou, and Y. Zhao, "Effect of age and cycloplegia on the morphology of the human crystalline lens: swept-source OCT study," *J. Cataract Refract. Surg.* **48**, 8-15 (2022).
177. S. Giovanzana, T. Evans, and B. Pierscionek, "Lens internal curvature effects on age-related eye model and lens paradox," *Biomed. Opt. Express* **8**, 4827-4837 (2017).
178. C. A. P. Cavallotti, and L. Cerulli, eds. *Age-Related Changes of the Human Eye* (Humana Press, 2008).
179. R. Michael, and A. J. Bron, "The ageing lens and cataract: a model of normal and pathological ageing," *Philos. Trans. R. Soc. Lond. B: Biol. Sci.* **366**, 1278-1292 (2011).
180. S. Ní Dhubhghaill, J. J. Rozema, S. Jongenelen, I. Ruiz Hidalgo, N. Zakaria, and M.-J. Tassignon, "Normative values for corneal densitometry analysis by scheimpflug optical assessment," *Invest. Ophthalmol. Vis. Sci.* **55**, 162-168 (2014).

181. R. Bocheux, P. Pernot, V. Borderie, K. Plamann, and K. Irsch, "Quantitative measures of corneal transparency, derived from objective analysis of depth-resolved corneal images, demonstrated with full-field optical coherence tomographic microscopy," *PLOS ONE* **14**, e0221707 (2019).
182. A. Consejo, M. Jiménez-García, and J. J. Rozema, "Age-related corneal transparency changes evaluated with an alternative method to corneal densitometry," *Cornea* **40**, 215-222 (2021).
183. J. Mamou, C. A. Wa, K. M. P. Yee, R. H. Silverman, J. A. Ketterling, A. A. Sadun, and J. Sebag, "Ultrasound-based quantification of vitreous floaters correlates with contrast sensitivity and quality of life," *Invest. Ophthalmol. Vis. Sci.* **56**, 1611-1617 (2015).
184. J. H. Nguyen, J. Nguyen-Cuu, J. Mamou, B. Routledge, K. M. P. Yee, and J. Sebag, "Vitreous structure and visual function in myopic vitreopathy causing vision-degrading myodesopsia," *Am. J. Ophthalmol.* **224**, 246-253 (2021).
185. J. A. Martínez-Roda, M. Vilaseca, J. C. Ondategui, M. Aguirre, and J. Pujol, "Effects of aging on optical quality and visual function," *Clin. Exp. Optomet.* **99**, 518-525 (2016).
186. T. J. T. P. van den Berg, L. Franssen, B. Kruijt, and J. E. Coppens, "History of ocular straylight measurement: A review," *Z. Med. Phys.* **23**, 6-20 (2013).
187. J. L. Alió, P. Schimchak, H. P. Negri, and R. Montés-Micó, "Crystalline lens optical dysfunction through aging," *Ophthalmology* **112**, 2022-2029 (2005).
188. S. R. Uhlhorn, D. Borja, F. Manns, and J. M. Parel, "Refractive index measurement of the isolated crystalline lens using optical coherence tomography," *Vis. Res.* **48**, 2732-2738 (2008).
189. A. de Castro, D. Siedlecki, D. Borja, S. Uhlhorn, J.-M. Parel, F. Manns, and S. Marcos, "Age-dependent variation of the gradient index profile in human crystalline lenses," *J. Mod. Opt.* **58**, 1781-1787 (2011).
190. A. Neri, M. Ruggeri, A. Protti, R. Leaci, S. A. Gandolfi, and C. Macaluso, "Dynamic imaging of accommodation by swept-source anterior segment optical coherence tomography," *J. Cataract Refract. Surg.* **41**, 501-510 (2015).
191. E. Martinez-Enriquez, A. de Castro, A. Mohamed, N. G. Sravani, M. Ruggeri, F. Manns, and S. Marcos, "Age-related changes to the three-dimensional full shape of the isolated human crystalline lens," *Invest. Ophthalmol. Vis. Sci.* **61**, 11 (2020).
192. J. M. Sparrow, A. J. Bron, N. A. P. Brown, W. Ayliffe, and A. R. Hill, "The Oxford clinical cataract classification and grading system," *Int. Ophthalmol.* **9**, 207-225 (1986).
193. A. C. Rencher, and W. F. Christensen, *Methods of multivariate analysis* (John Wiley & Sons, 2012).
194. N. E. Helwig, "Multivariate linear regression, <http://users.stat.umn.edu/~helwig/notes/mvblr-Notes.pdf>."
195. Zach, "The Breusch-Pagan test: Definition & example, <https://www.statology.org/breusch-pagan-test/>."
196. A. de Castro, D. Siedlecki, D. Borja, S. Uhlhorn, J.-M. Parel, F. Manns, and S. Marcos, "Age-dependent variation of the gradient index profile in human crystalline lenses," *J. Mod. Optics* **58**, 1781-1787 (2011).

197. J. R. Kuszak, J. G. Sivak, and J. A. Weerheim, "Lens optical quality is a direct function of lens sutural architecture," *Invest. Ophthalmol. Vis. Sci.* **32**, 2119-2129 (1991).
198. R. Navarro, and M. Angeles Losada, "Shape of stars and optical quality of the human eye," *J. Opt. Soc. Am. A* **14**, 353-359 (1997).
199. A. Glasser, and M. C. Campbell, "Biometric, optical and physical changes in the isolated human crystalline lens with age in relation to presbyopia," *Vis. Res.* **39**, 1991-2015 (1999).
200. G. Scarcelli, P. Kim, and S. H. Yun, "In vivo measurement of age-related stiffening in the crystalline lens by Brillouin optical microscopy," *Biophys. J.* **101**, 1539-1545 (2011).
201. J. R. Kuszak, and K. J. Al-Ghoul, "A quantitative analysis of sutural contributions to variability in back vertex distance and transmittance in rabbit lenses as a function of development, growth, and age," *Optom. Vis. Sci.* **79**, 193-204 (2002).
202. K. J. Al-Ghoul, R. K. Nordgren, A. J. Kuszak, C. D. Freil, M. J. Costello, and J. R. Kuszak, "Structural evidence of human nuclear fiber compaction as a function of ageing and cataractogenesis," *Exp. Eye Res.* **72**, 199-214 (2001).
203. J. R. Kuszak, J. G. Sivak, K. L. Herbert, S. Scheib, W. Garner, and G. Graff, "The relationship between rabbit lens optical quality and sutural anatomy after vitrectomy," *Exp. Eye Res.* **71**, 267-281 (2000).
204. J. R. Kuszak, M. Mazurkiewicz, L. Jison, A. Madurski, A. Ngando, and R. K. Zoltoski, "Quantitative analysis of animal model lens anatomy: accommodative range is related to fiber structure and organization," *Vet. Ophthalmol.* **9**, 266-280 (2006).
205. R. B. Nowak, R. S. Fischer, R. K. Zoltoski, J. R. Kuszak, and V. M. Fowler, "Tropomodulin1 is required for membrane skeleton organization and hexagonal geometry of fiber cells in the mouse lens," *J. Cell Biol.* **186**, 915-928 (2009).
206. J. Parreno, C. Cheng, R. B. Nowak, and V. M. Fowler, "The effects of mechanical strain on mouse eye lens capsule and cellular microstructure," *Mol. Biol. Cell* **29**, 1963-1974 (2018).
207. B. R. Masters, "Confocal microscopy of the *in-situ* crystalline lens," *J. Microsc.* **165**, 159-167 (1992).
208. E. Acosta, J. Bueno, C. Schwarz, and P. Artal, "Relationship between wave aberrations and histological features in *ex-vivo* porcine crystalline lenses," *J. Biomed. Opt.* **15**, 055001 (2010).
209. Y. Shi, A. De Maria, T. Bennett, A. Shiels, and S. Bassnett, "A Role for Epha2 in cell migration and refractive organization of the ocular lens," *Invest. Ophthalmol. Vis. Sci.* **53**, 551-559 (2012).
210. A. Roorda, and A. Glasser, "Wave aberrations of the isolated crystalline lens," *J. Vis.* **4**, 250-261 (2003).
211. J. Jinagal, G. Gupta, and F. Thattaruthody, "Sutural cataract," *Ind. J. Ophthalmol.* **66**, 853 (2018).
212. J. Sukhija, and S. Kaur, "Congenital sutural cataract," *N. Engl. J. Med.* **371**, e27 (2014).
213. J. Martin Bland, and D. Altman, "Statistical methods for assessing agreement between two methods of clinical measurement," *Lancet* **327**, 307-310 (1986).
214. D. Giavarina, "Understanding Bland Altman analysis," *Biochem. Med.* **25**, 141-151 (2015).

215. P. Pérez-Merino, M. Velasco-Ocana, E. Martínez-Enriquez, and S. Marcos, "OCT-based crystalline lens topography in accommodating eyes," *Biomed. Opt. Express* **6**, 5039-5054 (2015).
216. M. Sun, J. Birkenfeld, A. de Castro, S. Ortiz, and S. Marcos, "OCT 3-D surface topography of isolated human crystalline lenses," *Biomed. Opt. Express* **5**, 3547-3561 (2014).
217. J. R. Kuszak, R. K. Zoltoski, and C. Sivertson, "Fibre cell organization in crystalline lenses," *Exp. Eye Res.* **78**, 673-687 (2004).
218. D. G. Cogan, "Anatomy of lens and pathology of cataracts," *Exp. Eye Res.* **1**, 291-295 (1962).
219. E. Vaghefi, B. P. Pontre, M. D. Jacobs, and P. J. Donaldson, "Visualizing ocular lens fluid dynamics using MRI: manipulation of steady state water content and water fluxes," *Am. J. Physiol. Regul. Integr. Comp. Physiol.* **301**, R335-R342 (2011).
220. S. Xiao, B. Lisa Jane, and F. Z. Hao, "Visible-light optical coherence tomography: a review," *J. Biomed. Opt.* **22**, 121707 (2017).
221. Y. Chen, S. Manzanera, J. Mompeán, D. Ruminski, I. Grulkowski, and P. Artal, "Increased crystalline lens coverage in optical coherence tomography with oblique scanning and volume stitching," *Biomed. Opt. Express* **12**, 1529-1542 (2021).
222. M. Guillon, K. Dumbleton, P. Theodoratos, M. Gobbe, C. B. Wooley, and K. Moody, "The effects of age, refractive status, and luminance on pupil size," *Optom. Vis. Sci.* **93**, 1093-1100 (2016).
223. M. Bahrami, A. V. Goncharov, and B. K. Pierscionek, "Adjustable internal structure for reconstructing gradient index profile of crystalline lens," *Opt. Lett.* **39**, 1310-1313 (2014).
224. D. C. Beebe, N. M. Holekamp, C. Siegfried, and Y.-B. Shui, "Vitreoretinal influences on lens function and cataract," *Philos. Trans. R. Soc. B: Bio. Sci.* **366**, 1293-1300 (2011).

# Appendix A

## Research Activity

The titles of journals and conference presentations listed in “**bold**” are relevant to this scientific dissertation.

### A.1 Peer-Reviewed Journal and Conference Proceedings

1. “**Age-related changes in geometry and transparency of the human crystalline lens revealed by optical signal discontinuity zones in swept-source OCT images**”, **Ashish Gupta**, Daniel Ruminski, Alfonso Jimenez Villar, Raúl Duarte Toledo, Grzegorz Gondek, Spozmai Panezai, Barbara Pierscionek, Pablo Artal, Ireneusz Grulkowski, in review.
2. “***In-vivo* SS-OCT imaging of crystalline lens sutures**”, **Ashish Gupta**, Daniel Ruminski, Alfonso Jimenez Villar, Raúl Duarte Toledo, Silvestre Manzanera, Spozmai Panezai, Juan Mompean, Pablo Artal, and Ireneusz Grulkowski, *Biomed. Opt. Express* 11, 5388-5400 (2020).
3. “Comparative study on the detection of early dental caries using thermophotonic lock-in imaging and optical coherence tomography”, Elnaz B. Shokouhi, Marjan Razani, **Ashish Gupta**, and Nima Tabatabaei, *Biomed. Opt. Express* 9, 3983-3997 (2018).
4. “Optimal selection of laser modulation parameters in photothermal optical coherence tomography”, **Ashish Gupta**, Martin Villiger, Nima Tabatabaei, *Proc. SPIE 10067, Optical Elastography and Tissue Biomechanics IV*, 1006718 (2017).

5. “Analytical study of optical component for optogenetic application”, **Ashish Gupta**, Arun Kumar, Optik - International Journal for Light and Electron Optics, Volume 126, Issue 3, 309-312 (2015).
6. “Holography: A Cyber World”, **Ashish Gupta**, Aprajita Sharma, The Institution of Electronics and Telecommunication Engineer conference proceedings, 29-32 (2013).
7. “Optogenetics: Past, present and future”, **Ashish Gupta**, Arun Kumar American Institute of Physics (AIP) Conference Proceedings 1536(1): 1221-1222 (2013).

## A.2 Conference Presentations

1. Photonics West 2023, 28 January - 02 February 2023, oral presentation, “**SS-OCT images of the human crystalline lens reveal local changes in the morphology and transparency with ageing**”, **Ashish Gupta**, Daniel Ruminski, Alfonso Jiménez Villar, Raul Duarte Toledo, Grzegorz Gondek, Spozmai Panezai, Pablo Artal, Ireneusz Grulkowski.
2. Frontiers in Optics and Laser Science (FiO LS) 2022, 17 - 20 October 2022, Rochester, NY, USA, oral presentation, “**Age-related local changes in the morphology and transparency of the human crystalline lens using SS-OCT**”, **Ashish Gupta**, Daniel Ruminski, Alfonso Jimenez Villar, Raúl Duarte Toledo, Grzegorz Gondek, Spozmai Panezai, Pablo Artal, Ireneusz Grulkowski.
3. 4th Interdisciplinary FNP Conference, 6–7 October 2022, Warsaw, Poland, poster presentation, “**Lenticular morphology and transparency changes with age using swept-source OCT imaging system**”, **Ashish Gupta**, Daniel Ruminski, Alfonso Jimenez Villar, Raúl Duarte Toledo, Grzegorz Gondek, Spozmai Panezai, Barbara Pierscionek, Pablo Artal, Ireneusz Grulkowski.
4. 22nd Polish-Slovak-Czech Optical Conference on Wave and Quantum Aspects of Contemporary Optics, 5-9 September 2022, Wojanów, Poland, oral presentation, “**Age-related changes in the morphology and optical density of**

- the crystalline lens**", Ashish Gupta, Ebrahim Safarian Balaujeh, Daniel Ruminski, Alfonso Jimenez-Villar, Raul Duarte-Toledo, Grzegorz Gondek, Barbara Pierscionek, Pablo Artal, Ireneusz Grulkowski.
5. Siegman International School on Lasers 2022, 25 June – 2 July 2022, poster presentation, "**Swept-source OCT (SSOCT): a tool for in-vivo studies of optical density and morphological changes of the crystalline lens related to aging**", Ashish Gupta, Alfonso Jimenez-Villar, Ewa Mączyńska-Walkowiak, Spozmai Panezai, Grzegorz Gondek, Daniel Rumiński, Ireneusz Grulkowski.
  6. ARVO Annual Meeting 2022, 01-04 May 2022, poster presentation, "**Age-related changes in optical density and geometry of human crystalline lens measured with SS-OCT**", Ashish Gupta, Ebrahim Safarian Baloujeh, Daniel Ruminski, Alfonso Jimenez-Villar, Raul Duarte-Toledo, Grzegorz Gondek, Pablo Artal, Ireneusz Grulkowski.
  7. Photonics West 2022, 22-27 January 2022, oral presentation, "Phase analysis of the OCT signal from human crystalline lens during accommodation", Daniel Ruminski, Alfonso Jimenez-Villar, Ashish Gupta, Pablo Artal, Ireneusz Grulkowski.
  8. Photonics West 2022, 22-27 January 2022, oral presentation, "Impact of ultrafast motion on signal in SS-OCT and method for correction of motion-related image artifacts", Ashish Gupta, Daniel Ruminski, Grzegorz Gondek, Ireneusz Grulkowski.
  9. Frontiers in Optics and Laser Science 2021, 01-04 November 2021, oral presentation, "Correlation of image artifacts related to high speed motion in swept-source OCT", Ashish Gupta, Daniel Ruminski, Ireneusz Grulkowski.
  10. Optics and Photonics for Scientific Progress 2021, 13-14 April 2021, "**In-vivo imaging of crystalline lens sutures pattern with bench-top SS-OCT system**", Ashish Gupta, Alfonso Jimenez-Villar, Raul Duarte-Toledo, Daniel Ruminski, Silvestre Manzanera, Spozmai Panezai, Juan Mompean, Pablo Artal, Ireneusz Grulkowski.

11. Photonics West 2021, 06-11 March 2021, oral presentation; “***In-vivo* three-dimensional imaging of crystalline lens sutures**”, **Ashish Gupta**, Daniel Ruminski, Alfonso Jimenez Villar, Raúl Duarte Toledo, Silvestre Manzanera, Spozmai Panezai, Juan Mompean, Pablo Artal, and Ireneusz Grulkowski.
12. Photonics West 2020, 01-06, February 2020, Poster Presentation; “**SS-OCT reveals crystalline lens sutures**” **Ashish Gupta**, Daniel Rumiński, Silvestre Manzanera, Pablo Artal, and Ireneusz Grulkowski.
13. 4th Polish Scientific Networks, 19-21 September 2019, Poster Presentation, “High-resolution *in-vivo* visualization of opacifications of the human eye vitreous”, **A. Gupta**, D. Rumiński, S. Manzanera, E. Safarian Baloujeh, J. Sebag, P. Artal, I. Grulkowski.
14. 4th Polish Scientific Networks, 19-21 September 2019, Poster Presentation, “**Three-dimensional visualization of the crystalline lens sutures for the assessment of aging processes in the eye**”, D. Rumiński, **A. Gupta**, S. Manzaner, J. Sebag, P. Artal, I. Grulkowski.
15. 3rd Interdisciplinary FNP Conference, 11-12 April 2019, Poster Presentation, “High-resolution imaging platform for *in-vivo* visualization of opacifications of the human eye vitreous”, D. Ruminski, S. Manzanera, E. Safarian Baloujeh, **A. Gupta**, R. Pakulski, J. Sebag, P. Artal, and I. Grulkowski.
16. Photonics West 2017, 28 January - 02 February 2017, Poster presentation, “Optimal selection of laser modulation parameters in photothermal optical coherence tomography”, **Ashish Gupta**, Martin Villiger, Nima Tabatabaei.
17. International Conference of Telecommunication and Networks (TELNET’13), 27-28 February 2013, Poster presentation, “Holography: A Cyber World”, **Ashish Gupta**, Aprajita Sharma.
18. Recent Trends in Applied Physics & Material Science (RAM 2013), 01-02 February 2013, Poster presentation, “Optogenetics: Past, Present and Future”, Arun Kumar, **Ashish Gupta**.

### **A.3 Passive Conference Participation**

1. Presbiopia 2019, Łódź, Poland, in-person.
2. FiO LS Conference 2020, online.

### **A.4 Participation in organizing academic conferences**

1. The 25th International Workshop on Quantum Systems in Chemistry, Physics and Biology (QSCP), 19-24 June 2022, Torun, Poland.
2. Quantum Optics X, 5-11 September 2021, Torun, Poland.
3. The 14th School on Acousto-Optics and Applications, 24-27 June 2019, Torun, Poland.
4. International Conference of Telecommunication and Networks (TELNET), 27-28 February 2013, Noida, Uttar Pradesh, India.

### **A.5 Academic Awards**

1. PROM project II, 2019 – For attending and presenting my work at the international conference Photonics West 2020, San Francisco, USA.
2. IDUB OPTOFOTO 2020/2021 - For accomplishment made in my research project, presenting the results in reputed conferences, and publishing in a reputed journal.
3. IDUB OPTOFOTO 2021/2022 - For accomplishment made in my research project, presenting the new results in reputed conferences, and producing results for another manuscript.

## **A.6 Funding**

1. Foundation for Polish Science within the Smart Growth Operational Programme 2014–2020 of the European Union (TEAM Programme, # POIR.04.04.00-00-5C9B/17-00).
2. Polish National Science Centre (OPUS Programme, #2018/31/B/NZ5/02156).